



Praveen Sridhar

**Physical Modeling of Material Removal
in Grinding: Grit-Workpiece Approach
and Wheel-Workpiece Approach**

Herausgeber: Prof. Dr.-Ing. Kristin de Payrebrune
Computational Physics in Engineering - Berichte
Band 2 | 2024

Bibliografische Information Der Deutschen Bibliothek

Die Deutsche Bibliothek verzeichnet diese Publikation in der Deutschen Nationalbibliografie; detaillierte bibliografische Daten sind im Internet über <http://dnb.ddb.de> abrufbar.

Bibliographic information published by Die Deutsche Bibliothek

Die Deutsche Bibliothek lists this publication in the Deutsche Nationalbibliografie; detailed bibliographic data is available in the Internet at <http://dnb.ddb.de>.

Computational Physics in Engineering - Berichte CPE

Wissenschaftliche Schriftenreihe des
Lehrstuhl Computational Physics in Engineering CPE
der Rheinland-Pfälzischen Technischen Universität Kaiserslautern-Landau

Herausgeber: Lehrstuhl Computational Physics in Engineering CPE
Prof. Dr.-Ing. Kristin de Payrebrune
Postfach 3049
Rheinland-Pfälzische Technische Universität Kaiserslautern-Landau
67653 Kaiserslautern

Verlag: Rheinland-Pfälzische Technische Universität Kaiserslautern-Landau

Druck: Rheinland-Pfälzische Technische Universität Kaiserslautern-Landau
Dezernat 5 Technik
Abteilung 5.6 Foto-Repro-Druck

D-386

© Lehrstuhl Computational Physics in Engineering CPE, 2023
Rheinland-Pfälzische Technische Universität Kaiserslautern-Landau
Gottlieb-Daimler-Straße
67663 Kaiserslautern

Alle Rechte vorbehalten, auch das des auszugsweisen Nachdrucks, der auszugsweisen oder vollständigen Wiedergabe (Photographie, Mikroskopie), der Speicherung in Datenverarbeitungsanlagen und das der Übersetzung.

Als Manuskript gedruckt. Printed in Germany.

ISBN 978-3-95974-213-9
ISSN 2941-7066

Physical Modeling of Material Removal in Grinding: Grit-Workpiece Approach and Wheel-Workpiece Approach

Vom Fachbereich Maschinenbau und Verfahrenstechnik
der Rheinland-Pfälzischen Technischen Universität Kaiserslautern-Landau
zur Erlangung des akademischen Grades

Doktor-Ingenieur (Dr.-Ing.)

genehmigte

Dissertation

von

Herrn

Praveen Sridhar, M.Sc.

aus Bangalore, Indien

Tag der mündlichen Prüfung: 09.11.2023

Vorsitzender: Dr.-Ing. Lisa Scheunemann

Berichterstatterinnen: Prof. Dr.-Ing. Kristin de Payrebrune

Prof. Dr. Ing. Barbara S. Linke

Prof. Dr.-Ing. Jan Christian Aurich

Acknowledgements

I would like to extend my sincerest gratitude to the following people who made this doctoral thesis a worthwhile endeavour.

I extend my deepest gratitude to Dr. Kristin de Payrebrune, my supervisor from RPTU Kaiserslautern, for your unwavering patience and insightful feedback that proved invaluable throughout my doctoral studies. My thesis work would not have been joyous and satisfying had it not been for your supervision and expertise. You have always been an inspiration and apart from academic advice, two of the key takeaways from this experience would be your optimism and exuberance. For all the long consultation hours and personal mentoring, thank you very much.

To Prof. Dr. Ing. Barbara S. Linke, my co-supervisor from University of California, Davis, for the knowledge and expertise shared throughout the course of my thesis. A special thank you for your patience in answering my questions and lending your support whenever I needed one.

To Prof. Dr.-Ing. Jan Christian Aurich, spokesperson of IRTG 2057, RPTU Kaiserslautern. Thanks for sharing your expertise during the cohort general meetings and your personal experiences during the group celebrations. You have always been and will be an inspiration to many.

The journey I embarked upon would not have been possible without the support and expertise generously provided by my defense committee.

I express sincere appreciation to the Deutsche Forschungsgemeinschaft for their generous funding, which played a pivotal role in making my research endeavors a reality. I am grateful to International Research Training Group (IRTG) for its specialized training, facilitating international research stays at UC Berkeley and UC Davis, and providing essential soft skill seminars. These experiences have significantly shaped my expertise and enriched both my research and overall professional growth.

Special thanks are also due to my office mates and cohort members, particularly for their constructive feedback sessions and unwavering moral support. Acknowledgment is owed to the research assistants and study participants from the university, whose contributions and inspiration significantly influenced my work.

To my beloved parents, my sister, my wife, my family and dear friends, your love, encouragement and unwavering belief in me have been a constant source of motivation and encouragement throughout this journey.

Contents

Abstract	vii
Nomenclature	ix
Abbreviations	x
1 Introduction	1
1.1 Motivation	1
1.2 Aim and objectives	2
1.3 Outline of the thesis	3
2 Grinding Process Technology	5
2.1 Background of the grinding process	5
2.2 Grinding wheel fabrication procedure	5
2.2.1 Raw material weighting and mixing	6
2.2.2 Moulding process	7
2.2.3 Firing	7
2.2.4 Finishing	7
2.2.5 Summary	7
2.3 Material removal mechanism in grinding material	7
2.3.1 Material removal: grit-workpiece approach	8
2.3.2 Material removal: wheel-workpiece approach	8
2.4 Summary of grinding process technology	9
3 Finite Element Modelling and Simulation of Grinding Processes	11
3.1 Introduction and why FEM is suitable to model a grinding process	11
3.2 Finite element method approach for modelling material removal	12
3.2.1 Numerical formulation	12
3.2.2 Time integration schemes	13
3.2.3 Material model	13
3.2.4 Chip separation criteria	13
3.2.5 Friction scheme in FEM simulation	14
3.3 Finite element simulation-grinding process	14
3.3.1 Grit-workpiece approach	14
3.3.2 Wheel-workpiece approach	15
3.4 Summary of finite element modelling of grinding processes	16
4 Experimental Framework: Single and Multiple Grit Grinding	17
4.1 Single grit grinding approach	18
4.2 Establishment of single grit grinding test setup	19

4.2.1	Description of machining center used for scratch tests	19
4.2.2	Abrasive grit material and Indenters	20
4.2.3	Workpiece material and properties	22
4.2.4	Scratch test operation and data acquisition software	22
4.2.5	Experimental protocol	24
4.3	Scratch tests methods: Single Scratch Tests (SST) and Multiple Pass Scratch Tests (MPST)	25
4.4	Process Monitoring	26
4.4.1	Process Forces Measurement	26
4.4.2	Scratch profile topography measurement	28
4.5	Summary of single grit scratch experimental framework	32
5	Experimental Results: Single and Multiple Grit Grinding	33
5.1	Introduction	33
5.2	Material removal mechanisms in terms of pile-up ratio and chip removal strength	33
5.2.1	Pile-up ratio and chip removal strength for single scratches	34
5.2.2	Pile-up ratio and chip removal strength for multiple scratches	36
5.3	Effective grit engaging radius	38
5.3.1	Effective grit engaging radius for single scratches	39
5.3.2	Effective grit engaging radius for multiple scratches	41
5.4	Process forces during single grit grinding	43
5.4.1	Process forces vs linear speed	43
5.4.2	Process forces for single scratches	44
5.4.3	Process forces for multiple pass scratches	46
5.5	Specific energy in single grit grinding	47
5.5.1	Specific energy for single scratches	48
5.5.2	Specific energy for multiple pass scratches	49
5.5.3	Summary of single grit scratch experimental investigations	51
6	Simulations: Grit-Workpiece Approach	53
6.1	Introduction	53
6.2	Discretizational approaches	54
6.2.1	Mesh based discretizational approaches	54
6.2.2	Particle based method	55
6.3	Simulation Workflow	55
6.3.1	Simulation models	55
6.3.2	Material model	56
6.3.3	Contact model	58
6.4	2D Orthogonal Cutting Model	58
6.4.1	Simulation Framework	58
6.4.2	Benchmark simulation	60
6.4.3	Effect of negative tool rake angle	61
6.5	3D single grit scratch model	63
6.5.1	Simulation framework of 3D scratch model	63
6.5.2	Model adaptation based on experimental findings	65
6.5.3	Benchmark simulation	65
6.5.4	Sensitivity analysis of discretizational approaches	67

6.6	Parameter study of 3D single scratch ALE model based on process forces and scratch topography	68
6.6.1	Results: 3D conical single scratch model	70
6.6.2	Results: 3D pyramidal single scratch model	73
6.7	Parameter study of 3D multiple scratch ALE model based on process forces and scratch topography	76
6.7.1	Results: 3D conical multiple pass scratch model	77
6.7.2	Results: 3D pyramidal multiple pass scratch model	79
6.8	Analysis of the simulation models based on pile-up ratio and specific energy . . .	82
6.9	Summary of grit-workpiece approach simulations	84
7	Simulations: Wheel-Workpiece Approach	87
7.1	Introduction	87
7.2	Mathematical Description of Virtual Wheel Modeling and simulation framework .	87
	Particle mixing and packing	89
	Particle compression	90
	Firing	91
	Dressing	92
	Calculation of output variables	93
	Surface calculation and modelling	94
7.3	Results of the virtual grinding wheel model	95
7.3.1	Analysis of output parameters based on dressing 10%	96
	Alternative static grain count	96
	Alternative average grain protrusion height	97
7.3.2	Grinding Wheel Measurement and Model Verification	98
	Grinding wheel measurement platform	98
	Model Validation	100
7.3.3	Grinding wheel surface	102
	Alternative protrusion height	102
	Protrusion height vs. alternative protrusion height	103
7.3.4	Practical applications	103
7.4	Up-scaling from grit-workpiece to wheel-workpiece simulation	104
7.4.1	Simulation with sample wheel specimen (virtual grinding wheel model) . .	105
7.4.2	Simulation with complete grinding wheel	107
7.5	Summary of wheel-workpiece approach simulations	109
8	Conclusions and suggestions for future work	111
8.1	Conclusions	111
8.2	Possible future work	113
	Bibliography	115

Abstract (English)

In this thesis, material removal mechanisms in grinding are investigated considering a grit-workpiece interaction as well as a grinding-wheel workpiece interaction. In grit-workpiece interaction in a micrometer scale, single grit scratch experiments were performed to investigate material removal mechanism in grinding namely rubbing, plowing, and cutting. Experiments performed were analyzed based on material removal, process forces and specific energy. A finite element model is developed to simulate a single-grit scratch process. As part of the development of the finite element scratch model a 2D and 3D model is developed. A 2D model is utilized to test material parameters and test various mesh discretizational approaches. A 3D model undertaking the tested material parameters from the 2D model is developed and is tested against experimental results for various mesh discretization. The simulation model is validated based on process forces and ground topography from experiments. The model is also further scaled to simulate multiple grit-workpiece interaction validated against experimental results. As a final step, simulation models are developed to simulate material removal, due to the interaction of grinding wheel and workpiece. A developed virtual grinding wheel topographical model is employed to display an approach, to upscale a grinding process from grit-workpiece interaction to wheel-workpiece interaction. In conclusion, practical conclusions drawn and scope for future studies are derived based on the developed simulation models.

Abstract (German)

In dieser Arbeit werden die Mechanismen des Materialabtrags beim Schleifen untersucht, wobei sowohl die Wechselwirkung zwischen Korn und Werkstück als auch die Wechselwirkung zwischen Schleifscheibe und Werkstück berücksichtigt wird. Bei der Korn-Werkstück-Wechselwirkung im Mikrometermaßstab wurden Experimente mit einem einzelnen Korn durchgeführt, um die Mechanismen des Materialabtrags beim Schleifen zu untersuchen: Reiben, Pflügen und Schneiden. Die durchgeführten Experimente wurden anhand des Materialabtrags, der Prozesskräfte und der spezifischen Energie analysiert. Es wurde ein Finite-Elemente-Modell entwickelt, um einen Ein-Korn-Ritzprozess zu simulieren. Als Teil der Entwicklung des Finite-Elemente-Ritzmodells wird ein 2D- und 3D-Modell entwickelt. Ein 2D-Modell wird verwendet, um die Materialparameter zu testen und verschiedene Ansätze zur Netzdiskretisierung zu prüfen. Ein 3D-Modell, das die getesteten Materialparameter aus dem 2D-Modell übernimmt, wird entwickelt und mit experimentellen Ergebnissen für verschiedene Maschendiskretisierungen getestet. Das Simulationsmodell wird anhand der Prozesskräfte und der Werkstück topografie aus den Experimenten validiert. Das Modell wird auch weiter skaliert, um die Wechselwirkung zwischen mehreren Körnern und Werkstücken zu simulieren, die anhand der experimentellen Ergebnisse validiert werden. In einem letzten Schritt werden Simulationsmodelle entwickelt, um den Materialabtrag zu simulieren, der durch die Wechselwirkung von Schleifscheibe und Werkstück entsteht. Eine entwickelte virtuelle Schleifscheibentopographiemodell wird verwendet, um einen Ansatz zur Hochskalierung eines Schleifprozesses von der Korn-Werkstück-Interaktion zur Scheibe-Werkstück-Interaktion aufzuzeigen. Abschließend werden auf der Grundlage der entwickelten Simulationsmodelle praktische Schlussfolgerungen gezogen und Möglichkeiten für künftige Untersuchungen abgeleitet.

Nomenclature

Symbol	Unit	Description
V_c	mm/s	Cutting speed grinding
f	μm	Feed in orthogonal cutting
a_p	μm	Undeformed chip thickness in grinding
$a_{p,\text{exp}}$	μm	Pre-defined depth of cut in grinding experiments
γ	$^\circ$	Tool rake angle
α	$^\circ$	Tool clearance (or flank) angle
u	J/mm^3	Specific energy
F_c, F_n	N	Cutting forces and passive/normal forces
A	MPa	Initial yield strength
B	MPa	Strain hardening constant
C		Strengthening coefficient of strain rate
n		Strain hardening coefficient
m		Thermal softening coefficient
$H1$		Initial stress triaxiality dependent parameter
$H2$		Stress triaxiality dependent constant
$H3$		Stress triaxiality dependent coefficient
$H4$		Strain rate dependent parameter
$H5$		Temperature dependent parameter
\dot{D}		Overall damage variable (in damage evolution criterion)
K_{IC}	MPa	Fracture toughness mode I
K_{IIC}	MPa	Fracture toughness mode II
ν		Poisson ratio
E	GPa	Young's modulus
$\dot{\epsilon}$		Strain rate
$\dot{\epsilon}_0$		Reference strain rate
$\bar{\epsilon}^f$		Failure plastic strain
G_f		Fracture energy per unit area of a crack
L		Characteristic length of a finite element
σ_{y0}	MPa	Yield stress at onset of damage
τ_f	MPa	Frictional stress
σ_n	MPa	Passive stress
μ		Coefficient of friction
d_e	μm	Element discretization
d_p	μm	Particle discretization
GA		Groove cross-section area (in scratch test)
$P1, P2$		Side pile up areas (in scratch test)
R_{gi}	μm	Abrasive grit diameter
R_{pi}	μm	Total particle diameter
f_b		Bond fraction
f_g		Grain fraction
a_0	μm	Initial neck radius of bond material
a	μm	Final neck radius of bond material
τ_g	hrs	Grain-boundary diffusion's characteristic time
t	hrs	Firing time
a_{dp}	mm	Dressing depth
f_d	mm/min	Dresser travel speed
F_b	N/mm^2	Bonding force

Abbreviations

FEM	Finite Element Method
FEA	Finite Element Analysis
LAG	Lagrange
ALE	Arbitrary Lagrange Eulerian
SPH	Smoothed-particle hydrodynamics
PFEM	Particle Finite Element Method
SST	Single Scratch Tests
EXP	Experiment
MPST	Multiple Scratch Tests
EGER	Effective Grit Engaging Radius
MRR	Material Removal Rate
2D	Two Dimensional
3D	Three Dimensional

Chapter 1

Introduction

1.1 Motivation

Grinding is a material removal process that employs abrasive particles as the medium of cutting [51]. Grinding is applied to obtain highly smooth surfaces with a desired tolerance for metals and ceramics [18]. It is one of the most critical surface finishing processes that is commonly used in the industry and it accounts for almost 70% of the precision machining operations performed [119]. Grinding operation finds its application in a wide variety of industries such as consumer electronics, healthcare devices, supply chain, automotive and aerospace [95]. To meet the demand for parts with very high precision (in micrometer level), research on relatively small abrasive tools is crucial and promising. Grinding is a complex machining process where interaction of multitude of abrasive grit with the workpiece happens at high speed [118]. The prime reason for research in this area would be to focus on minimizing energy consumption and costs, including abrasive tool failure and reduction of labor costs.

Research on understanding the material removal process in grinding has been conducted for several decades [15]. There are many research articles that focus on the entire grinding wheel-workpiece interaction with validations from grinding experiments. The models were built using numerical, kinematic, and analytical approaches. These works are well summarized in [112] and [15]. It is highly challenging to make experimental observations and build tendencies only by performing wheel-workpiece grinding experiments, due to the highly complex nature of material removal that takes place during a grinding process [100, 32]. It is also difficult to observe and measure certain mechanical characteristics like temperature, stresses, and strains along the machined surfaces. The cost of experimentation and the validation of the experimental observation at certain machining conditions make it a undesirable approach to decode the grinding process [125, 67].

With the advancement and acceleration of computing and technology, it has become possible to model and perform simulation of the material removal process in grinding, in a digital environment [68, 121]. Empirical models, regression models and neural network models are being developed to predict the process responses in terms of known variables [66, 57]. However, these models are not valid under all machining circumstances. These approaches are unable to provide detailed process information as observed while performing experiments. Finite element methods are widely accepted modelling techniques, as they are highly scalable and can be validated based on multiple experimental observations. Even though there has been a huge improvement with respect to computational power, there lies a plethora of technical complexities in simulating the phenomena of material removal during a grinding process.

To overcome this problem, the grinding process using the single grit approach is applied by [37, 82]. This approach considers a single grit abrasive action on a workpiece to understand the material removal mechanism based on cutting forces, ground topography, stress and strain distribution [53]. Grinding is a very complex material removal process unlike other cutting processes such as drilling, milling, and cutting [60]. Material removal occurs in three dominant phases namely rubbing, plowing, and cutting [37]. Simulating a single grit process and validating the model with experiments would be the first step to understand the material removal mechanism that take place during a grinding process. Once the single grit scratch model is tested and validated for various machining conditions, the simulation is extended to a multiple scratch process, where there is interaction of multiple grits with the workpiece. Finally, the model is scaled from a grit-workpiece approach to a wheel-workpiece approach. This goal is achieved by digitally generating a grinding wheel topography first and use this grinding wheel to simulate the material removal in a complete grinding process. Hence a complete spectrum of simulation models is developed to understand the material removal mechanisms that occur in grinding and thereby reducing the experimental effort.

1.2 Aim and objectives

This work aims to develop a numerical grinding process model at micro scale in two phases. The first phase entails the development of numerical models that represent a grit-workpiece interaction followed by the development of numerical models that represent a wheel-workpiece interaction, in the second phase.

To achieve the aim of developing these models, the following objectives are set in place.

- Experimental analysis of single grit and multiple grit scratches by varying the input machining conditions like speed, depth of cut, tool geometry, tool apex angle to determine the influence of these parameters on the material removal mechanism.

To perform the first main objective, the following sub-objectives were accomplished.

- Conceptualization and construction of a linear single axis scratch machine center to perform single and multiple grit scratch tests.
 - Development of process monitoring tools to capture process forces during a scratch process.
 - Establishment of metrology techniques to measure the ground scratch surface.
- Validation and testing of a developed FEM grit scratch simulation models under different input conditions.

To perform the second main objective, the following sub-objectives were accomplished:

- Development of a FEM model to simulate an orthogonal cutting model to test and determine influential parameters such as meshing parameters and material model parameters.
- Development of a FEM model to simulate the material removal mechanism during the interaction between a single grit and workpiece

- Extension of the developed FEM model to simulate the material removal mechanism during the interaction between multiple grits and workpiece.
- Integration of a virtual grinding wheel model in a FEM material removal simulation to simulate the interaction between a grinding wheel and workpiece.

To perform the final main objective, the following sub-objectives were accomplished:

- Development of the virtual grinding wheel topography model considering the process steps involved in the fabrication of grinding wheels.
- Validation of the numerically generated virtual wheel topography with microscopic measurements of a grinding wheel.

1.3 Outline of the thesis

This thesis is composed of eight chapters with an introductory chapter at the beginning.

Chapter 2 presents the fundamentals of the grinding process. It contains a description of the manufacturing process in fabrication of a grinding wheel. Finally, material removal mechanisms taking place in a grinding process is introduced, based on two approaches namely wheel-workpiece approach and grit workpiece approach.

Chapter 3 presents modelling and simulation techniques used in the grinding process. A brief overview of the finite element method, constitutive material model, failure model, meshing techniques and contact models are presented. A literature review of finite element simulation of grinding wheels, in terms of the wheel-workpiece approach and grit-workpiece approach is provided.

Chapter 4 presents the methodology for the experiments performed based on the single grit approach. It includes establishment of a single grit grinding setup, definition of a workpiece and abrasive materials, establishment of process monitoring systems to perform experimental analysis.

Chapter 5 presents the experimental results of single/multiple grit grinding tests. The generated scratches are analyzed based on various output process parameters measured based on the process forces and ground surface topography.

Chapter 6 presents the finite element simulation results based on the grit-workpiece approach. It includes the results of an orthogonal cutting model and results from a 3D scratch simulation model simulating the material removal interaction between single/multiple grit on a workpiece.

Chapter 7 presents the numerical models based on the wheel-workpiece approach. It presents the description and results of a virtual grinding wheel topography model. Furthermore, FEM simulation results, simulating the interaction between a grinding wheel topography and a workpiece are presented. Finally, a general grinding process simulation is presented, simulating the interaction between a flat grinding wheel and a workpiece.

Chapter 8 contains the overall observations, discussion, and conclusions on the experimental and simulation results.

Chapter 2

Grinding Process Technology

In this chapter, the fundamentals of the grinding process, grinding wheel fabrication process and grinding process removal mechanisms are discussed.

2.1 Background of the grinding process

Grinding is a material removal process where there is interaction between a grinding wheel and a workpiece [118]. The grinding wheel is made up of many abrasive particles that are randomly oriented. In a surface grinding process, the operations can be classified into an up-cut grinding process and a down-cut grinding process [111]. An up-cut grinding process is where the grinding wheel rotates in the direction opposite to the movement of the workpiece, on the other hand, in a down-cut grinding process, the wheel rotation and the movement of the workpiece are in the same direction. A grinding process is performed at a relatively high speed and the chip thickness is relatively small [6]. This differentiates grinding from other metal cutting processes as the chip thickness is small especially in case of fine grinding. Grinding process can be classified based on the amount of material removed. Stock removal grinding is a process to remove unwanted material without regard to the surface finish achieved. Whereas finish grinding is a process where high surface finish tolerances are achieved [18]. To quantify grinding process performance, a grinding system behavior must be evaluated properly based on the correlation between the input and output parameters [62]. Grinding system behavior can be assessed based on kinematics, mechanics, abrasive geometry, energy and material properties according to [82]. Various factors that affect the grinding process performance include grinding force, machining vibration, temperature at cutting zone and surface roughness of workpiece material [82, 61, 19]. To enhance the grinding process performance, the grinding wheel must be periodically dressed to keep it in good condition. This could result in a good workpiece surface finish and integrity by generating lower forces and temperatures during the process [39].

2.2 Grinding wheel fabrication procedure

The performance and surface finish of a grinding process is directly related to the grinding wheel used during the grinding operation [60, 15]. It is hence important to understand each of the fabrication steps to manufacture a grinding wheel, to generate the desired 3D morphology and mechanical features [11]. A grinding wheel is a composite matrix consisting of abrasive particle and bond material. Figure 2.1 shows a typical structure of a grinding wheel, which consists of abrasive grits held on by a bond material and in addition void spaces or pores between the grit-bond matrix [27]. The void spaces or pores in a grinding wheel provides channels for lubrication and aids in the clearance of chips from the grit-bond matrix [18].

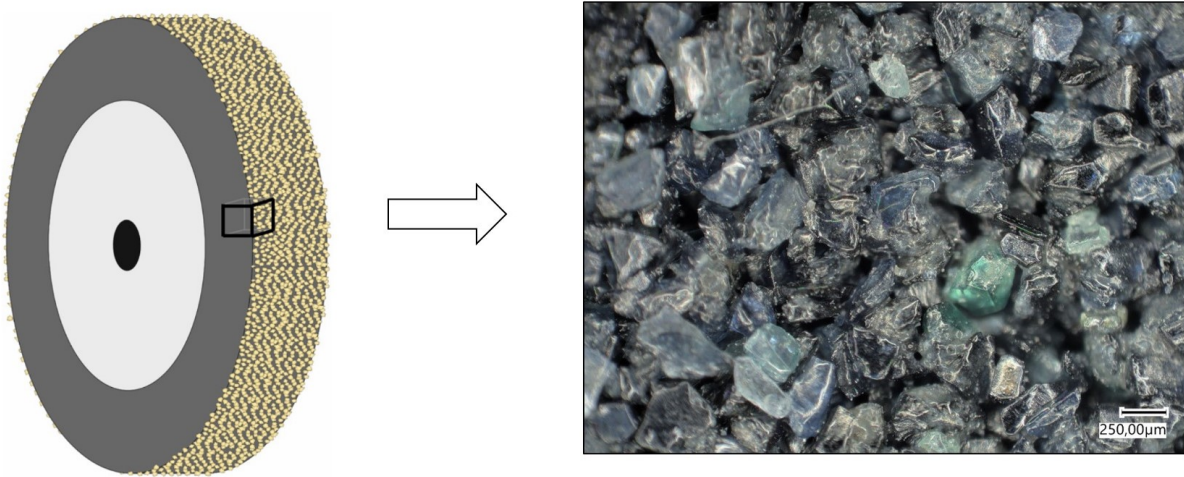


FIGURE 2.1: Structure of a silicone carbide grinding wheel with vitreous bond (60 grit size)

The Fig.2.2 show the general steps involved in the fabrication of a vitrified grinding wheel. The detailed description of each of these processes are described in the following sections.

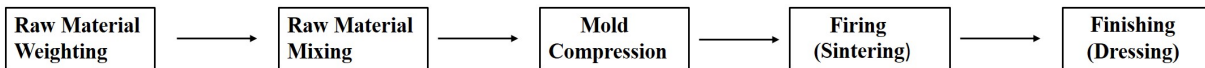


FIGURE 2.2: Steps in the fabrication of a grinding wheel

2.2.1 Raw material weighting and mixing

Abrasive grains and bonding materials are the two important ingredients that make up a grinding wheel [82, 59]. Although, additives are additionally blended along with the grit-bond mixture to shape the wheel in a desirable manner [60]. Abrasive grains are a central component that constitute a grinding wheel [60]. The abrasive grits are chosen carefully based on the application, and characteristics such as hardness, thermal conductivity and friability [82, 18]. The choice of bond material can vary from such as silicate, vitrified, resinoid, shellac, rubber, and metal [29]. Vitrified bonds are employed in case of fine grinding operations, while resin bonds are used in case of stock removal grinding operations. In addition, additives are used to vary the porosity of a grinding wheel which in turn contributes to the cutting characteristic of a grinding wheel [29]. Pores in a grinding wheel offer void spaces for chips from the material process to be removed from the grit-bond matrix [9]. The porosity also provides channels for the flow of the cutting liquid which enables control of heat at the cutting zone. A variety of materials are used as additives to create proper porosity [23]. For example, in a conventional vitrified wheel, organic glue is used as an additive material. The ratio of additives used vary based on the application [34]. 1% additives are used in case of vitrified wheel and 10% in case of organic bonded wheels [60].

Once the raw materials needed to fabricate a grinding wheel are chosen carefully based on the application, precise quantities of abrasive material, bond material and additives are weighed based on a special formula [12]. The three ingredients are mixed with the aid of water based binding agents. The binding agent aids the mixture to retain the shape until the bond solidifies.

It is important that the mixture blended is free flowing and uniformly distributes the abrasive grits [51].

2.2.2 Moulding process

The most common type of grinding wheel mould's shape is an annular disc shape [34]. A definite quantity of the blended mixture is poured into a mould. A typical mould consists of four parts: an outer shell with a thickness of about 1 inch (2.5 cm) and a height twice as high as the height of the desired wheel, a circular pic with diameter like the center hole of the desired wheel, two flat circular plates one with a diameter of the desired grinding wheel and another with a diameter of the center hole. Employing a hydraulic press, a pressure between the range of 100 to 500 psi is applied for 10 to 30 seconds onto the mould. After this, the pressed wheel is removed from the mould and is transferred to a heatproof carrier. Final shaping of the wheel is done at this stage. The wheel is now transported to a kiln for the firing (sintering) process. [60, 59]

2.2.3 Firing

The purpose of firing (sintering), a vitrified grinding wheel is to melt the binder material around the grit-bond matrix. The vitrified grinding wheel is sintered at different temperatures based on the application on a wide range of furnaces [60]. Vitrified bond wheels are fired at a temperature range of 927°C to 1260°C, while resin bond wheels are fired at a temperature range of 149°C to 204°C [61].

2.2.4 Finishing

As a final step, the grinding wheel is moved to the finishing area. The grinding wheels are dressed with typically a single point dressing tool [27, 82]. The wheel is checked if the center hole is concentric to the wheel circumference. Steps are taken to correct the thickness and parallelism of the wheel edges. Finally, the large grinding wheels are balanced to reduce vibration during operation [60].

2.2.5 Summary

A numerical model is proposed that recreates each of the above-mentioned fabrication steps as individual numerical algorithms. A virtual grinding wheel model is generated that resembles the topography of a real grinding wheel. The complete description of the modelling and results of the virtual grinding wheel model is provided in chapter 6. The generated virtual topography is used to perform material removal simulation to simulate the interaction between a grinding wheel and workpiece.

2.3 Material removal mechanism in grinding material

In grinding, the material removal mechanisms can be categorized into two groups:

- Material removal mechanism considering the interaction between single grit and workpiece. This investigation will be on a micro-scale.
- Material removal mechanism considering the interaction between a grinding wheel and workpiece. Here, the investigation will be on a macro scale.

2.3.1 Material removal: grit-workpiece approach

The major factor that dominates material removal and ground surface generation is the interaction between abrasive grit and workpiece [37]. Material removal takes place in three phases during single grit-workpiece interaction. The first phase, rubbing begins when the grit slides within the elastic limit of the material. Following the rubbing phase is the plowing phase where there is material swelling up across both sides and as well as to the front of the grit. However, there is no chip formation occurring during the plowing phase. Finally when the plastic deformation crosses the fracture limit, the ultimate material removal occurs in form of grinding chips, this phase is called cutting [51, 82]. Finite element simulation of a single grit process is a reliable method to derive various output process parameters such as specific energy, ground topography and process forces [15, 82]. Also a well validated FEM model with experiments can be employed to reveal optimal grain geometry and other process parameters for material removal in a grinding process [82].

One critical parameter used in this thesis to characterize the grinding process is the specific cutting energy or force [19]. It is defined as the energy required to remove unit volume of material. It is observed that specific energy is a function of the cutting conditions like depth of cut, tool geometry etc. Hence it is attempted in this thesis to study the effects on the specific energy by varying input process parameters [26].

Although there are many similarities of the single grit grinding process and a micro cutting process, especially cutting and chip-formation process [35, 44]. A critical phenomenon not considered in the micro-cutting process is the sideward flow of material during a single grit process [80]. This is analyzed using the pile-up ratio parameter as part of this thesis. The material in the pile-up regions is more hardened compared to the workpiece material. The pile-up generated not only affects the surface roughness, but also affects the force required to remove the hardened material in the next cut scratch [32]. Therefore, the pile-up ratios reveal critical information of the material removal and energy consumption [33]. A comprehensive investigation is done as part of this thesis to understand the effect on the pile-up ratio by varying input process parameters.

2.3.2 Material removal: wheel-workpiece approach

The majority of grinding wheel models consider average grit density or uniform distribution of grit without considering the random distribution of abrasive grits as observed in a grinding wheel topography [17, 56]. The random distribution of grits, varying protrusion heights and pore volume between grit-bond matrix makes the grinding process stochastic in nature. Fig.2.3 shows an illustration of the random nature of material removal during a grinding process [108]. The first abrasive grit in contact with the flat workpiece surface produces a ground topography like the cross section of the grain, however the further shapes of the grit in contact will have shapes that intersect with the ground surface topography. This makes the material removal very complex and unknown. Hence, representation of the material removal process would require a robust 3D grinding wheel model that is physics based and which includes both topographical and mechanical properties of a grinding wheel [125]. In this thesis, a virtual grinding wheel model is developed considering the fabrication steps of a grinding wheel. The virtual grinding wheel will bear resemblance of a real grinding wheel, and when integrated in a FEM material removal simulation environment, it can successfully represent a grinding process simulation.

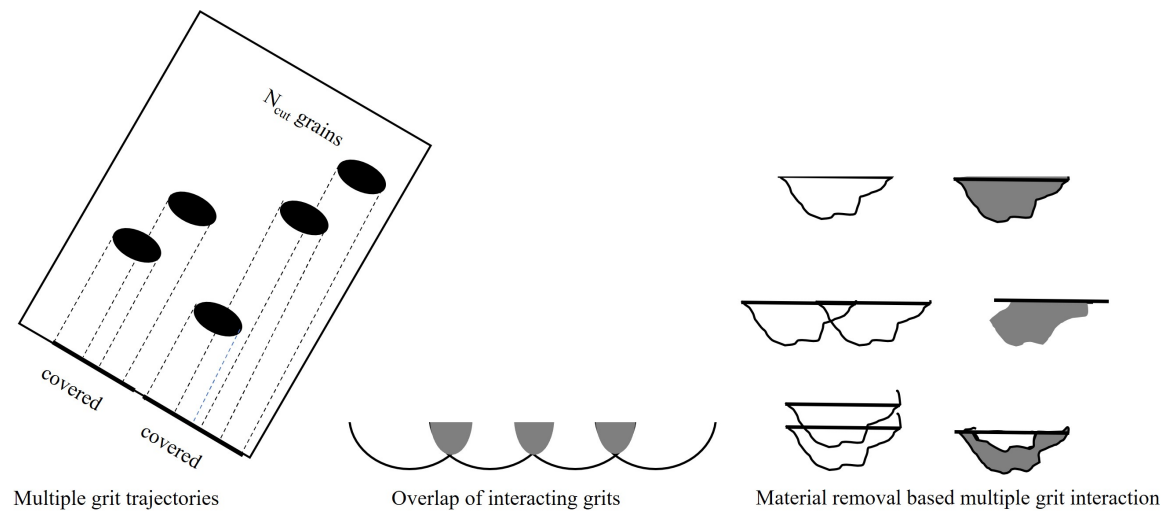


FIGURE 2.3: Interaction of multiple grit action on a workpiece during grinding and Change in workpiece topography due overlap of individual grit interactions, adapted based on [108]

2.4 Summary of grinding process technology

In this chapter, a brief introduction to the grinding process is provided. This is followed by a description of the fabrication process of a grinding wheel. Finally, the two approaches to describe the material removal process are described, namely the grit-workpiece approach and wheel-workpiece approach.

Chapter 3

Finite Element Modelling and Simulation of Grinding Processes

3.1 Introduction and why FEM is suitable to model a grinding process

To model dynamic machining processes and to predict various process parameters, a real system is simplified and simulated under certain machining conditions [67, 68]. With increase in computational power and ability to solve complex problems, simulation of the grinding process has become possible. A well-designed grinding process model can reduce the effort of experimental investigation, to determine various output process parameters [121]. Also, a well-developed physical model can determine many machining characteristics such as cutting mechanisms, strains, stresses, stress rates within material which are extremely difficult to determine through experiments [82, 126].

Based on literature, modelling approaches for a grinding process can be divided into physical models and empirical models [27, 15]. Empirical models are built based on experimental data. A fully developed model would require numerous grinding experiments performed, with recorded machining conditions to co-relate input and output parameters. The developed model is finally validated based on further experimental results and compared to check its accuracy [77, 66]. On the other hand, a physical model is developed considering physical laws, by using mathematical equations. The advantage of physical models over empirical models is that by adjustments made to a physical model, it can be applied to different machining processes. Physical models can be used to predict a wide variety of output process parameters such as stress-strain variation, deformation along cutting zones, temperature distribution along cutting zones, tool wear, chip formation etc., which are difficult to measure from experiments [1, 121]. This would provide key insight on various manufacturing processes.

It can be observed in Fig.3.1 below that the empirical models are mostly applied at a macroscopic scale, however physical models are applied both in the macroscopic and microscopic scale [15]. Finite Element Analysis (FEM) is modeled considering the physical laws to simulate the abrasive grit workpiece interaction. There are many powerful FEM software packages (such as Abaqus, Ansys, AdvantEdge etc.) that are easily available and applied to various machining processes [82, 68, 67]. These tools are preferred over other numerical methods. FEM is a very useful computational tool to predict various metal cutting output parameters like cutting forces, stresses, temperature, chip geometry taking into account abrasive fracture, abrasive wear, energy consumed, surface finish etc., Some of the output parameters predicted by FEM are difficult to

ascertain through experimental methods, making it a very valuable method [15, 27].

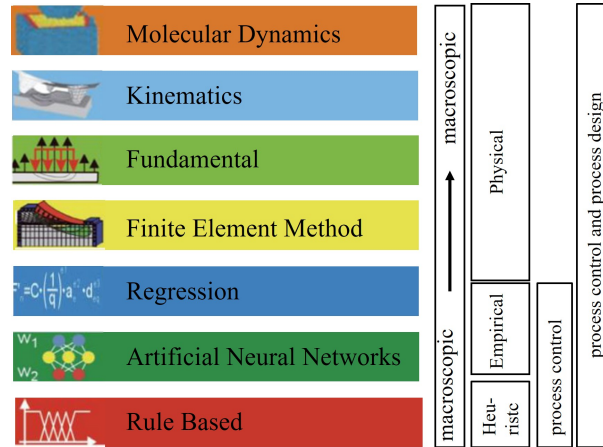


FIGURE 3.1: Simulations methods for abrasive processes [15]

3.2 Finite element method approach for modelling material removal

With the advent of high-power computers, FEM is a widely used method for solving complex problems like metal forming and cutting processes [123]. FEM is an assembly of finite elements where the solution variables are calculated at each node of an element. On each of the elements in the model, physical laws are applied [21]. The calculated nodal solutions are assembled to describe the process globally [21]. In the following section, various aspects in the development of a finite element simulation for abrasive grit-workpiece interaction process is described.

3.2.1 Numerical formulation

Metal cutting is a complex process with a multitude of simultaneously occurring mechanisms. As the experimental approach to study the machining process would be expensive, numerical simulations are performed to understand these effects by changing different process parameters and tool geometries [27]. Despite significant technological developments, it is challenging to model metal cutting processes to predict the optimal output process parameters. Hence it is very important to choose the right discretization approach to describe a complex material removal process like grinding [27, 22]. In continuum mechanics, the finite element motion can be described using three algorithms namely Eulerian, Lagrangian and Arbitrary Lagrangian Eulerian methods [22]. In addition, meshless methods like smooth particle hydrodynamics and particle finite element can be employed to describe the material motion [2, 28, 68].

A literature review of numerical simulations of metal cutting shows that most of the study was performed using mesh based approaches like Lagrange (LAG) or Arbitrary Lagrangian Eulerian (ALE) [73, 91, 98]. However, mesh distortion is a common reason for simulation crashes. Reviewing new modelling techniques [68, 89], meshless or particle based methods, are an alternative for machining simulations. However, even if the meshless methods show clear advantages for distortion problems, their accuracy in the calculation of the stresses, forces and temperature must be evaluated [106].

As a part of the comparative study, two mesh based methods Lagrangian (LAG) and Arbitrary Lagrangian Eulerian (ALE) approach, and a particle based methods Smooth Particle Hydrodynamics (SPH) are used to perform 2D orthogonal cutting and 3D scratch simulation on A2024 T351 aluminum are discussed in chapter 6. As an outcome of the study, the solution accuracy of the forces, stresses and temperatures inside the workpiece are compared between the mesh-based methods and particle-based methods for different cutting conditions thereby understanding which discretization approach is most suitable in modelling of abrasive grit-workpiece interaction process.

3.2.2 Time integration schemes

In FEM, nonlinear dynamic problems can be either solved using implicit or explicit time integration methods. Both these methods can be applied to many FEM problems. The iterative Newton's method is used to calculate an implicit solution [21]. In the usage of the implicit method, a set of equations at every time integration point are solved. For a solution to converge, it would require a large number of iterations, each with a prescribed increment [10, 70]. The implicit method helps maintain unconditionally stable linear system, which is its main advantage [21]. On the other hand, an explicit time integration scheme does not iteratively solve the equation making it more efficient.

In scope of metal cutting problems, explicit time integration schemes are mostly used [15]. The main advantage of the explicit method is that the solution is guaranteed to converge unlike the implicit method [103, 67, 4]. In this thesis, explicit integration method is used in FEM simulations.

3.2.3 Material model

To realistically represent the flow strength and subsequently the material removal mechanism, a robust constitutive material model is required. It is important to ascertain the flow stress properties of workpiece materials by performing experimental tests under varying stress, strain rate and temperatures [21]. In literature, various flow stress models are employed to model metal cutting at high strain rate and temperatures. The Johnson-Cook material model is the most frequently used material model to describe metal forming and cutting processes [68, 67, 121]. The Johnson-Cook model is a pure empirical model which calculates the flow stresses [46]. The parameters of the Johnson-Cook model can be estimated using tensile tests and Split-Hopkinson Pressure Bar (SHPB) tests [92]. In this work, Johnson-cook material model is primarily used to simulate low-speed single grit scratch processes as part of this thesis. However it is to be noted, while simulating high speed grinding processes, this model may often calculate lower strain rates and temperatures. A detailed description of the Johnson-Cook material model and the parameters used are described in chapter 6.

3.2.4 Chip separation criteria

Setting up a chip separation criteria in a machining simulation is important to cause chip formation [82]. Most of the chip separation is achieved by setting up a separation criterion, such as using damage evolution criteria and a damage model [13].

In literature, so far chip separation is achieved by applying the following methods.

- With the aid of material failure models based on fracture which simulates crack initiation to crack growth to final formation of chip [40].

- With the aid of Arbitrary-Lagrangian-Eulerian (ALE) adaptive meshing to simulate plastic flow of material [86].
- With the aid of particle based methods, which does not require chip separation criteria as the chip formation occurs due to the lack of cohesion between neighboring particles [68, 28, 1]

The use of a progressive damage model is a very important factor in modelling metal cutting simulations. Choosing the damage evolution criteria is a key factor that influences the results of the simulation. According to [71], the damage evolution criteria is provided by defining the equivalent plastic displacement or by defining fracture energy dissipation. The fracture energy dissipation according to Hillerborg [40] is evaluated as a function of material toughness. In this thesis, the damage evolution criteria in the LAG and ALE simulation are defined based on the fracture energy of dissipation.

3.2.5 Friction scheme in FEM simulation

The accuracy of the results predicted from the FEM simulations depends on two aspects. Firstly, a constitutive material model which describes the material deformation at high strain rates and temperatures [21] and secondly, a friction model that describes the friction characteristics between the tool-workpiece interface [85]. The friction condition at the tool-workpiece interface also strongly influences the heat generation at the cutting zones [42]. Hence, friction characterization is difficult and complex in machining. The Coulomb friction model is frequently used in the modelling of machining processes [42]. According to the model, the frictional forces are proportional to the normal forces with a coefficient of friction. The simulations in this thesis are performed by employing the Coulomb friction model [82].

3.3 Finite element simulation-grinding process

Grinding is a complex material removal process where the interaction on a workpiece takes place due to large number of unknown grit geometries that vary over time [15]. A physics based model that describes the complex relationships in terms of process, machine and workpiece parameters is invaluable [82, 60]. The developed model will predict various output parameters like workpiece surface topography, specific energy, grinding forces etc. In this thesis, the FEM modeling of the grinding process is classified into two approaches. The first approach is the material removal, considering the interaction between a single abrasive grit and workpiece. The second approach is the material removal, considering the interaction between a grinding wheel topography and workpiece.

3.3.1 Grit-workpiece approach

The single grit workpiece interaction approach occurs in three stages to achieve material removal in terms of grinding chips, according to [37] the three stages are rubbing, plowing, and cutting [27]. Simulation of a single grit action on a workpiece is complex, which is not the same as the conventional cutting processes. A single grit scratch process varies from conventional metal cutting based on the following aspects.

- Geometry of cutting tool: Cutting tools in processes like turning, milling, and drilling have properly defined tool shapes and chip formed are according to this shape and is continuous

[67]. However, in grinding the abrasive grits have complex unknown geometries, and the cutting conditions change instantaneously due to grit wear and breakage thus making the material removal process more complex [33, 100].

- Size effect: The undeformed chip thickness is relatively small compared to other conventional cutting processes. This led to generation of serrated chip formation that are much smaller in size [87].
- Material flow direction effect: In conventional cutting processes, the material flow is mostly in the direction of the shaped tool. However, in grinding this is sideward along with the material displacement along the tool direction [114].
- Rake angle of cutting tool: The rake angle of a tool is defined as the angle made between the tool face and material in front of it. In case of grinding, the abrasive grits mostly have a negative rake angle as opposed to conventional cutting processes which use shaped tools with a positive rake angle [76].

Material removal mechanisms vary based on the above mention point in a single grit scratch process, when compared to a conventional cutting process [27, 82]. There can be some similarities derived between single grit cutting and shaped tool cutting. Orthogonal cutting simulations can be performed with large negative tool rake angle as suggested by [80, 124]. In this thesis, the development of the FEM single grit scratch model is divided into two phases. In phase one, a 2D orthogonal cutting model is developed to test various mesh formulations, parameterize material model parameters and test change in tool geometry (high negative rake angles). The 2D orthogonal model is computationally less intensive to test various simulation ensembles. As part of phase two, a 3D scratch model is developed. Here the optimum simulation parameters from the 2D orthogonal model are transferred to the 3D model. Using this approach, modelling and simulation of a single grit process are performed in this thesis.

3.3.2 Wheel-workpiece approach

Wheel-workpiece approach in this work defines a finite element simulation of a grinding process considering a grinding wheel and workpiece interaction. In literature, most of the FEM models are used to perform thermal analysis, to calculate the influence of heat and surface pressure on the ground workpiece topography [16]. In these models, the grinding wheel is represented as a combined heat source and surface pressure. The grinding wheel is then moved over the workpiece surface [69]. Various profiles of heat flux distribution like rectangular or parabolic are tested as input parameters to understand their effects on the surface integrity of the workpiece [54]. Most of the available grinding wheel models do not consider the actual grinding wheel topography and are modelled as a flat surface. In this thesis, the actual grinding wheel topography is incorporated to simulate the material removal process due to interaction between wheel-workpiece [60, 125]. To perform this simulation, a pre-requisite is to develop a virtual grinding wheel topography model. There exists three different approaches to develop a grinding wheel model - empirical models, neural network models and physical models [77, 57]. The focus of this work is to develop a physical model to describe a grinding process, a physics based 'through-the-process' modelling approach is considered to describe a grinding wheel topography [59]. A 'through-the-process' approach means each manufacturing step in the fabrication of a grinding wheel is described as numerical algorithms [60]. The result of this physical simulation is a realistic topographical model of a grinding wheel, which can be integrated into a FEM simulation to

simulate the material removal process during a grinding process. With this implementation, the FEM model is up-scaled from a grit-workpiece approach to a wheel-workpiece approach.

3.4 Summary of finite element modelling of grinding processes

In this chapter, the simulation framework of a finite element model to simulate a grinding process is described. The chapter provides the motivation of why FEM is most suited to simulate material removal. The various elements that need to be considered while developing a material removal FEM model are summarized. Finally, the FEM models that are developed based the on the grit-workpiece approach and wheel-workpiece approach are described.

Chapter 4

Experimental Framework: Single and Multiple Grit Grinding

The multiple irregularly shaped and sized abrasive grits that are adhered to the grinding wheel create an extraordinarily complicated mechanism for material removal, as schematically shown in Fig.4.1. The single grit contact with the workpiece is crucial because grinding can be modeled as a cumulative process that results from multiple single grit actions over the workpiece. The material removal phenomenon could be extrapolated to the full grinding wheel-workpiece interaction with a thorough understanding of the various grit-workpiece interaction mechanisms.

In this chapter, a methodological approach is presented with respect to the single grit test. setup and workpiece sample preparation. In addition, methods of single grit grinding including single grit and multiple pass scratching are presented. Furthermore, force measurement technique and scratch surface measurement technique are described. Finally, the strategy to analyze scratches produced by single and multiple grit actions in terms of material removal mechanism is presented.

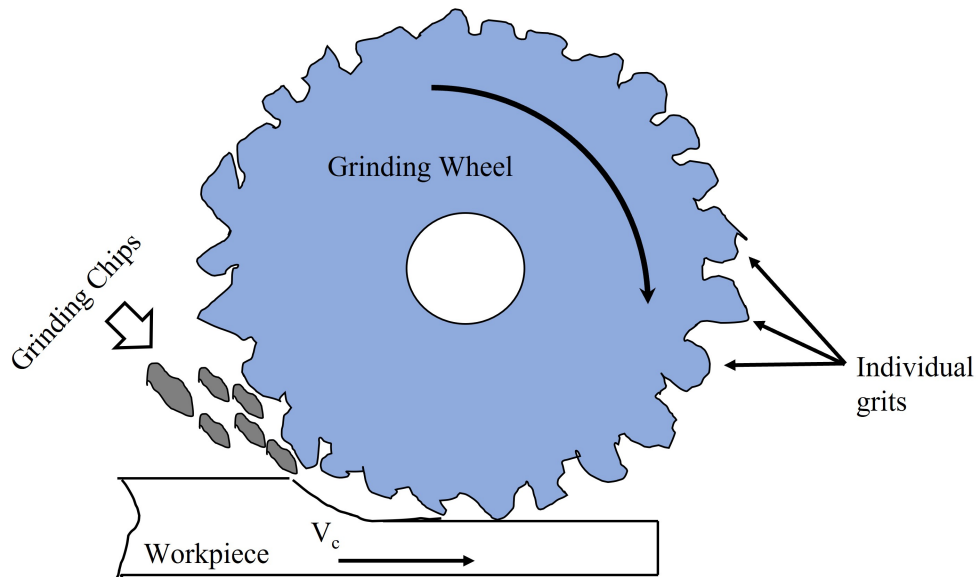


FIGURE 4.1: Schematic of grinding process (N : Wheel rotational speed, rpm; V_c : Work table speed (or feed) mm/min) [82]

4.1 Single grit grinding approach

To understand the complexity of the grinding material removal process, the single grit grinding process can be considered as an elementary part of the grinding process of the grinding wheel, and the grinding process as the integration of numerous actions performed by individual grits. Thus, understanding of single grit action performed on a workpiece is important to model the overall grinding phenomena. Single grit action on the workpiece comprises of rubbing, plowing, and cutting (chip formation) phases. The schematic representation of single grit action with the three material removal phases is given in Fig.4.2.

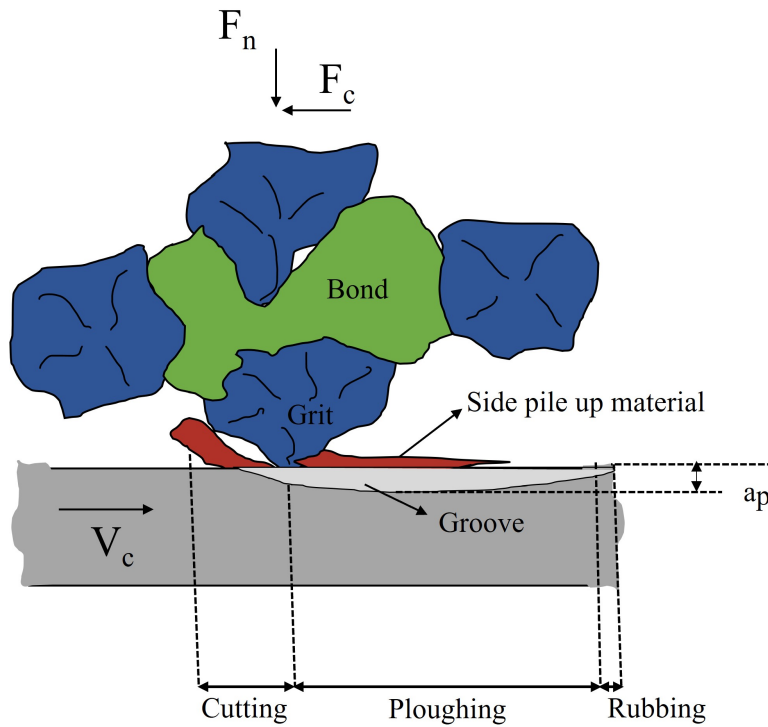


FIGURE 4.2: Schematic of single grit grinding action (F_n : passive force; F_t : cutting force; N : rotational cutting speed, rpm; V_c : work table speed or feed, mm/min; a_p : undeformed chip thickness) [82]

The contribution of each phase to material removal varies depending on the size, geometry and sharpness of the grit, the hardness of workpiece and grinding kinematic conditions, such as depth of cut and scratching speed, etc. For instance, with smaller depth of cut, rubbing and plowing processes are more prominent while with greater depth of cut, chip formation would be prominent. In this investigation, single grit grinding tests were performed on A2024 T351 aluminum workpiece. Scratch grooves were cut by single grit action performed at different speeds and with gradually increasing depth. A force sensor was used during the single grit grinding process to record the force exerted during scratching. Single grit grinding tests have been performed with different operational conditions and compared with numerical FEM simulation. A schematic of the investigation work flow is illustrated in Fig.4.3

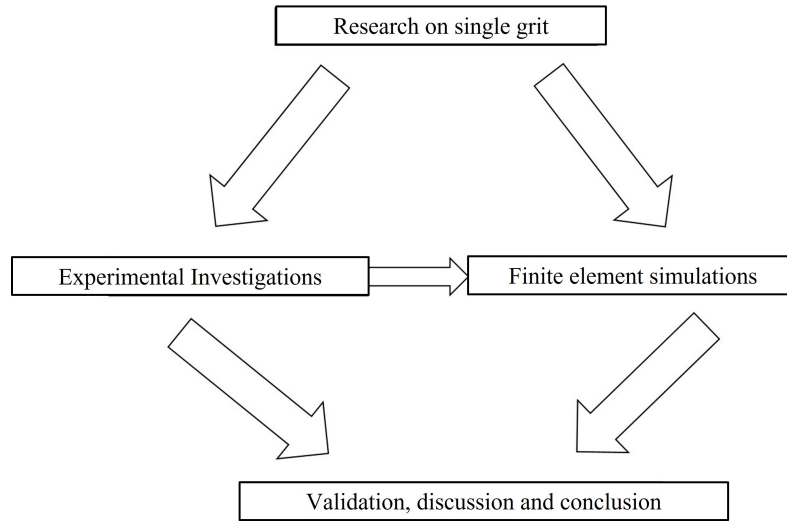


FIGURE 4.3: Simple schematic of research method

4.2 Establishment of single grit grinding test setup

In this section, the experimental platform, cutting indenters used and the workpiece material used to perform the scratch tests are explained in detail.

4.2.1 Description of machining center used for scratch tests

The scratch experiments are performed with a custom built 1-axis linear belt drive machine. Fig.4.4 A shows the schematic diagram and Fig.4.4B shows the actual platform of the single grit grinding test setup. The experimental setup for single grit scratching comprises of several components as listed below:

- A single axis linear belt drive motion device (stroke length=850 mm)
- A vertical z -axis height adjustable table to set the depth of cut (in order of 1 μm)
- An x -axis table, which can move horizontally demarcating the scratches from each other (in order of 0.1 mm)
- A Kistler 3-axis force sensor (Type: 9119AA1), placed under the workpiece for measuring the process forces
- A high pressure vacuum chuck to hold the workpiece in place while performing the scratch tests
- Aluminum alloy (A2024 T351) specimens with the dimensions 75 mm \times 20 mm \times 2 mm
- An indenter holder affixed along a vertical gantry to hold the diamond tip conical/pyramidal indenters (tool angle= 105°, 120° and 135°)

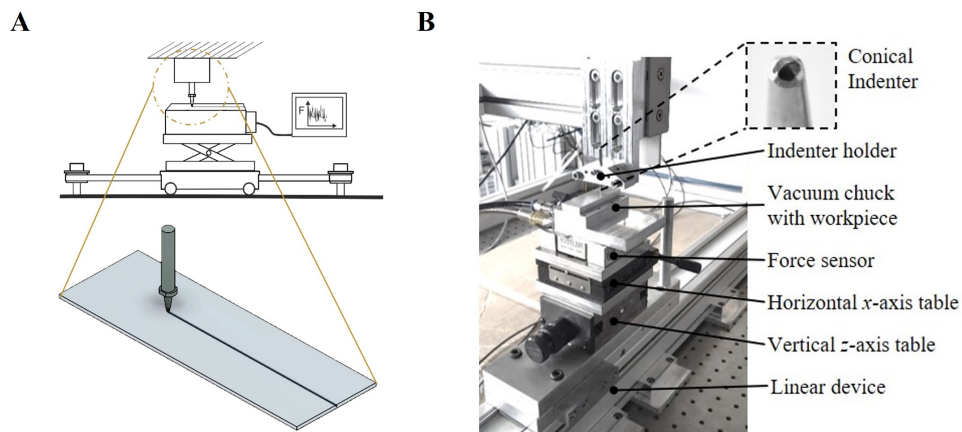


FIGURE 4.4: A: Schematic representation of the linear scratch setup, B: Machine center: single axis linear scratch setup

4.2.2 Abrasive grit material and Indenters

Synthetic diamonds having a mesh size of 40/50 as shown in Fig.4.5 were used to perform the single grit grinding experiments. Diamond abrasive was chosen as it has a significant higher toughness, endurance, abrasive ability, thermal conductivity and chemical stability compared to standard abrasive materials such as Al_2O_3 and SiC. Diamond has a significantly higher modulus of elasticity (700 - 1200 GPa) than conventional abrasives (296-365 GPa). The specific heat capacity of diamond (507.9 J/kg°C) is lower than Al_2O_3 . The important characteristics of commonly used abrasives are explained in detail in chapter 2.

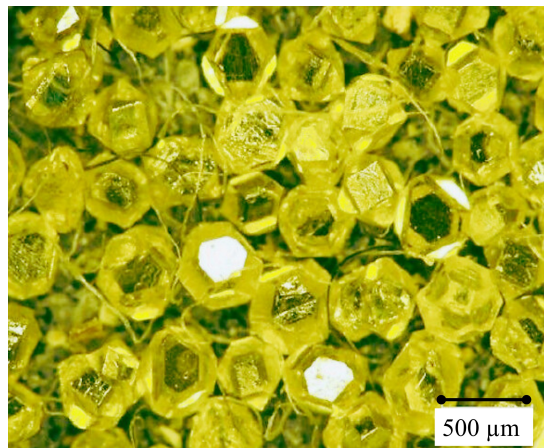


FIGURE 4.5: Diamond abrasive grits [82]

The diamond grits are soldered onto a steel holder as shown in Fig.4.6A. Initially, a hole is drilled on the steel holder to place the diamond grit, after which the soldering process is carried out to firmly fix diamond grits onto the steel holder. In Fig.4.6B three types of diamond tip indenters are shown, conical diamond tip geometries, pyramidal diamond tip geometries and unshaped diamond tip geometries. It can be observed in Fig.4.6B that the conical and pyramidal indenter geometries have a defined tool angle, the tool angle "X" in case of conical indenter and the tool angle "Y" in case of pyramidal indenter.

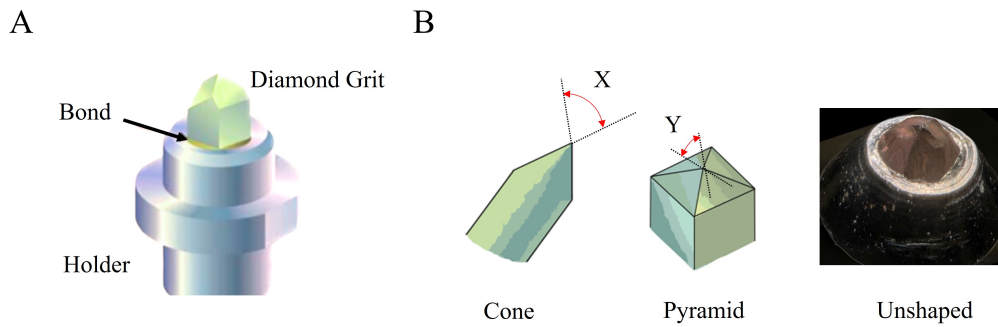


FIGURE 4.6: A: Schematic representation of single grit indenter, B: Types of single grit indenters based on tool tip geometry [117]

Fig.4.7 shows a closer view of the pyramidal and conical indenters. Three tool angles 105° , 120° and 135° are used to perform the scratch experiments for both the conical and pyramidal indent geometries as shown in Fig.4.8. Scratch experiments were performed to understand the effect of grit shape and tool angle on the process forces and scratched surface topography.

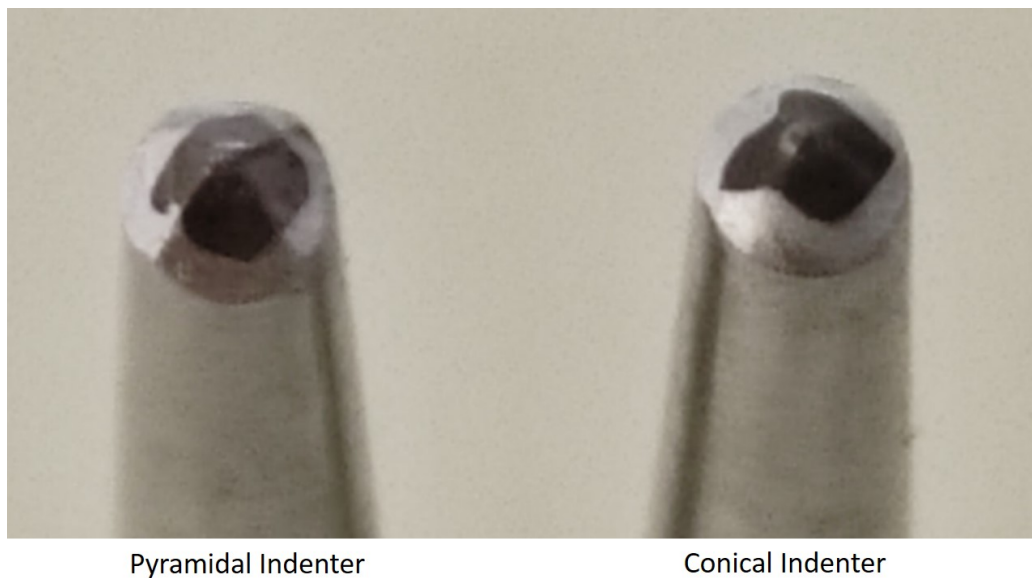


FIGURE 4.7: Pyramidal and conical indenter

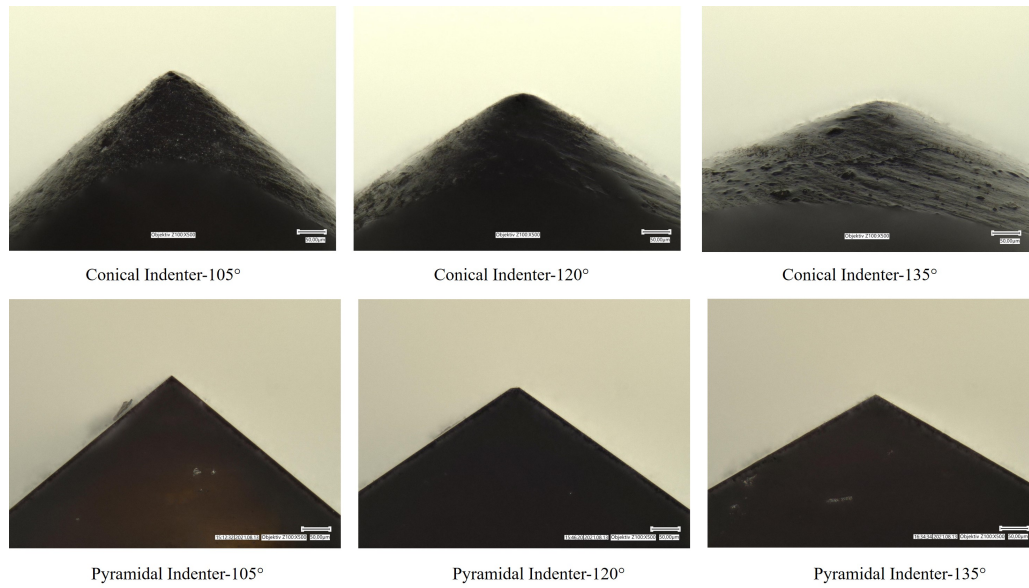


FIGURE 4.8: Microscopic images of conical and pyramidal indenters

4.2.3 Workpiece material and properties

Aluminum (A2024-T351) was used as the workpiece material to perform scratch experiments. The specimens are rectangular in size (75 mm × 20 mm × 2 mm) which are the length, breadth, and thickness respectively. To avoid the initial impact between the indenter and the specimen, both ends of the specimen are chamfered by 45°. Table 4.1 shows the typical properties of aluminum A2024-T351. Similar properties are used in the FEM simulations performed for validation of the simulation results. The Fig.4.9 shows the scratches performed on an aluminum A2024-T351 sample with the zoomed in microscopic scratch profile.

TABLE 4.1: Workpiece material properties of aluminum A2024-T351

Material properties	Aluminum A2024-T351
Density	2780 kg/m^3
Tensile strength	395 MPa
Yield strength	400 MPa
Elastic modulus	73.1 GPa
Poisson's ratio	0.33
Melting point	502 °C

4.2.4 Scratch test operation and data acquisition software

LabVIEW 2018 platform is used to program the servomotor that drives the single axis linear motion unit. Using Labview software, the rotational motion of the servo motor is converted into translatory motion. The user provides the stroke length, which is the length by which the linear slide moves along the linear motion unit. The linear slide is programmed to perform a trapezoidal motion, where the linear slide initially accelerates to reach the set linear speed, after which the speed remains constant for a period and finally the linear slide decelerates to come to a halt. Fig.4.10 shows the user interface of the scratch test operating software. The user can perform

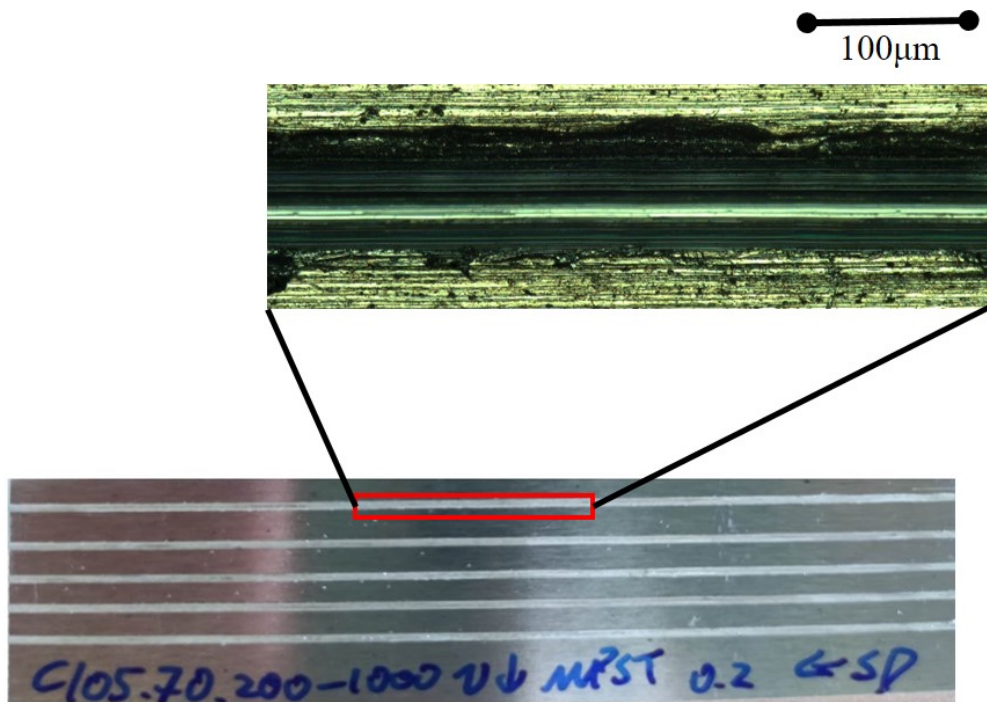


FIGURE 4.9: Macroscopic and microscopic image of scratched workpiece performed with 105° conical indenter

three basic motions using the linear motion unit, namely a forward move, a reverse move, or a home move. Forward motion, as the name suggests, is a forward motion of the linear slide and the reverse move moves the slide in the backward direction. For both these moves, the user can provide various inputs such as the target position (in mm), velocity (in mm/s), acceleration (in mm/s^2) and acceleration jerk (mm/s^2). Home move is used to re-position the linear slide at the preset zeroth position. The start and stop button are used to initiate or cancel a scratch test. On the left-hand side of the user interface real time data acquired during a scratch test are interactively plotted.

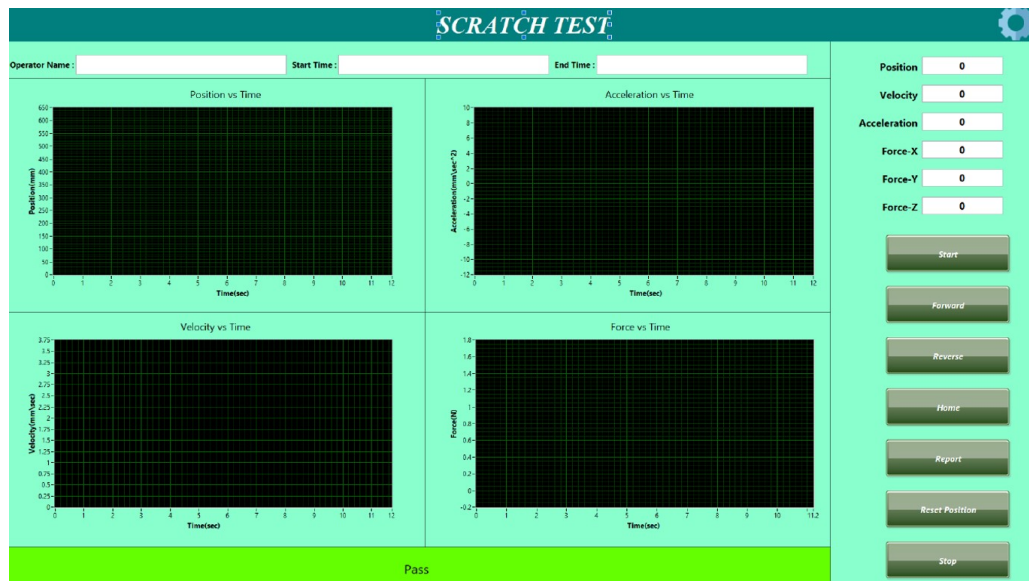


FIGURE 4.10: User interface of the scratch test operating software

4.2.5 Experimental protocol

To measure the experimental data more accurately, the force sensor is warmed up for one hour before the experiment. During this time, the samples are prepared for the experiment. The samples are immersed in acetone and the surface is cleaned in an ultrasonic bath unit. The air pressure of the vacuum pump is set to minus 0.8 bar. The sample is then held in the sample holder with the vacuum pump and the experiment platform is moved under the height measuring laser. The starting point of the scratch is determined by adjusting the threads in the y-direction of the x-stage. The indenter is lightly placed on the specimen and held, then the distance gauge is nullified. Then the whole specimen is checked to see if the flatness deviation of the specimen is less than $7 \mu\text{m}$ with a help of a height measuring laser as shown in Fig.4.11. The experimental platform is pulled away from the indenter and the infeed is determined by adjusting in the z direction with help of a z-axis table. Finally, the cutting speed is set, and the force gauge is switched on. The platform is moved to the initial position and the scratch test is performed. The test is repeated three times for each scratch test and the data from the three tests are averaged in the subsequent data analysis.

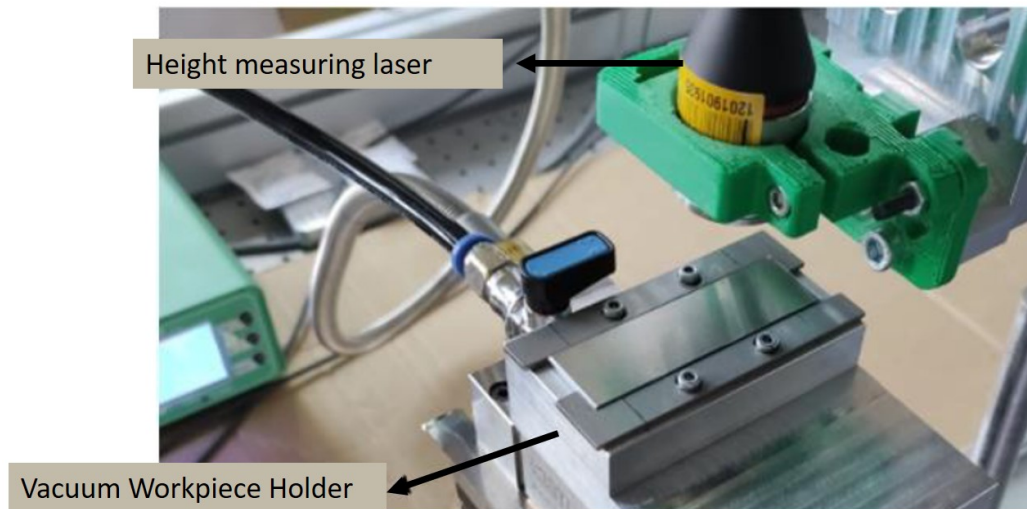


FIGURE 4.11: Zoomed in view: experimental platform

4.3 Scratch tests methods: Single Scratch Tests (SST) and Multiple Pass Scratch Tests (MPST)

To analyze the material removal mechanism in grinding using the single grit approach, two experimental schemes are used as part of this thesis, Single Scratch Test (SST) and Multiple Pass Scratch Tests (MPST).

Single Scratch Tests (SST) are performed to understand the material removal employing an individual grinding grit. To reduce measurement errors, the scratch test is repeated 3 times and the meaning of the data acquired is used for the analysis. All scratches performed on the same aluminum sample for various linear speeds for a particular indenter geometry (shape and tool angle) and depth of cut. The distance between the scratches is set to about 1.5 mm such that there is no interaction between individual scratches performed, which could influence the material removal. Fig.4.12 A shows a microscopic image of a SST.

MPST are performed to understand the influence of interaction between the individual scratches on the material removal. The SST experiment examined only the grinding condition of a single abrasive grain on the surface of the specimen. In practice, several abrasive grains act on the surface of the workpiece simultaneously during the grinding process. Therefore, MPST experiments are needed to study the scratching of multiple abrasive grains on the specimen surface. The mutual interaction and force between multiple scratches are observed in MPST experiment. The key difference between MPST and SST experiments is the distance between adjacent scratches. When the distance between the scratches is reduced to a certain level, interactions between scratches occur, making the MPST experiment different from the SST experiment. In the MPST experiment, a single abrasive grain will produce three abrasive cuts on the surface of the sample under the same experimental conditions, and these three cuts will produce a fixed spacing between the scratches. In the actual grinding process, the distances between scratches are random and not consistent. To evaluate the experiment and the study uniformly, the distance between the scratches is controlled and set to 0.2 mm. After the first and second scratch pass performed, 0.2 mm and 0.4 mm spacers are used to move the specimen in

the horizontal direction, hence maintaining a constant distance of 0.2 mm between the individual scratches. Fig.4.12 B shows a microscopic image of an MPST.

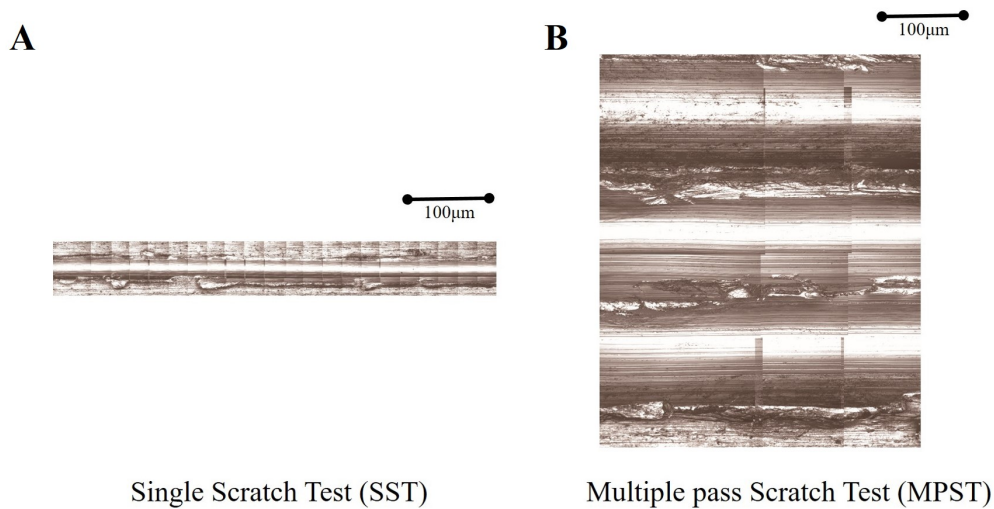


FIGURE 4.12: A: Microscopic image of single scratch test, B: Microscopic image of multiple scratch test

4.4 Process Monitoring

Process monitoring in machining processes is crucial to assess process performance [93]. During machining, real-time process monitoring systems can give relevant information, which is essential for the effectiveness of the process. Real-time and in-process monitoring systems can also be used to protect the machine from unexpected events such as high-speed grinding wheel failure that would cause significant damage to high-speed systems [43]. However, selection of sensors, where to place them, and how to process the data and extract information are issues that need to be evaluated by the researchers. In machining, power sensors, force sensors, accelerometers, and distance lasers are all used for process monitoring. In this section, the methodology of data acquisition and how the data is processed is explained in detail. This section is sub-categorized based on the two main measurements made, which are the process force measurements and the scratch profile topography measurement.

4.4.1 Process Forces Measurement

Force measurement is one of the most important process monitoring methods in machining applications because machining performance and machined surface quality are directly related to the forces exerted during machining. Machining forces play a key role in determining tool life, tool or workpiece damage, surface quality parameters, residual stresses, surface hardness and elastic-plastic deformation of the workpiece material [93]. Machining forces for grit grinding are of interest for this research. Single grit grinding is the elementary action of grinding process; the machining force measured during single grit action could provide a better understanding of grinding mechanics and can be compared to finite element simulation results. A Kistler 3-axis force sensor (Type: 9119AA1) in combination with a charge amplifier (Type: 5080A) is used in the experiments as shown in Fig.4.13. A force data acquisition system has three measurement

ranges, low, medium, and high.

High range with low sensitivity is between ± 4 kN for F_x , F_y and F_z components. Medium range with higher sensitivity is between ± 0.4 kN for F_x , F_y and F_z components. Low range with highest sensitivity is between ± 0.04 kN for F_x , F_y and F_z components. In this research, the sensor was set for the medium range, since forces exerted while performing scratch experiments lie in this range. For accurate measurement the sensor needed to be calibrated in situ after installation. Calibration was performed by applying masses (50 g, 100 g, 200 g, 500 g, 1000 g, 2000 g and 5000 g) to the X, Y and Z directions. LabVIEW software package is used to monitor and to record the force sensor measurement. Forces exerted due to the grinding process contain important information on surface integrity and overall grinding process performance. Normal and cutting forces were recorded during single grit scratching to obtain possible relations between the material removal mechanism and other parameters such as cutting speed and depth of cut. The sampling rate for the force measurement acquisition is set to 10,000 samples/s. An example of the forces measured with conical indenter (tool angle = 120°) for $a_{p,exp} = 50 \mu\text{m}$ and linear speed $v_c = 200 \text{ mm/s}$ is shown in Fig.4.13. It can be observed that the normal forces exerted are higher in comparison to the tangential forces exerted. Both the normal and tangential forces show a symmetric distribution at steady state condition, where the linear speed remains constant. As seen in Fig.4.14 statistical averages of the process forces are extracted at steady state condition, these are used for further data analysis.

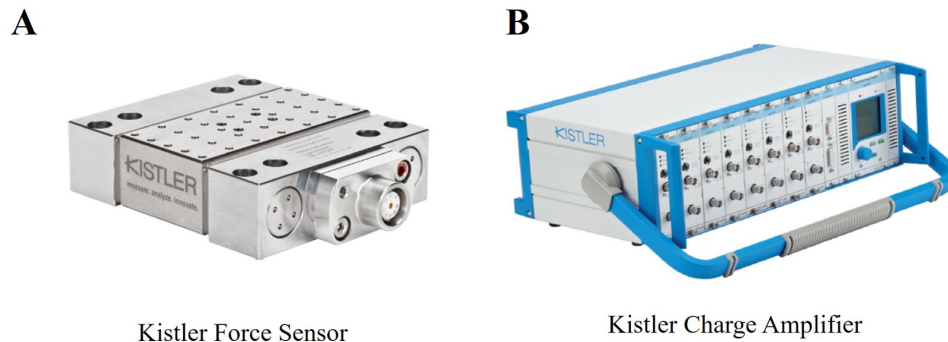


FIGURE 4.13: Process force acquisition instruments; A: Kistler force sensor, B: Kistler charge amplifier [90]

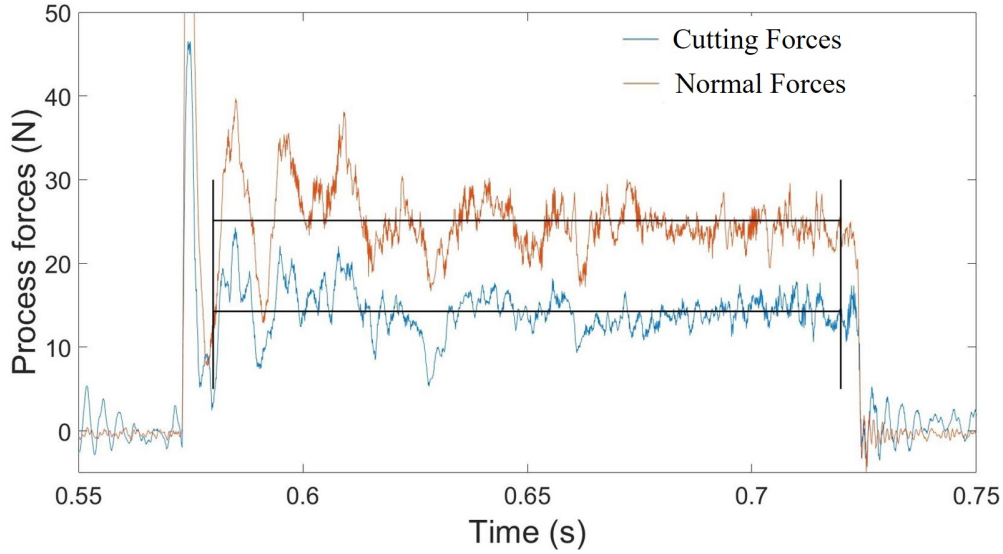


FIGURE 4.14: Sample process forces measurement

4.4.2 Scratch profile topography measurement

As explained in the previous chapters, material removal behavior in grinding can be classified into rubbing, plowing, and cutting. Rubbing action occurs due to elastic deformation, plowing action occurs due to a combination of elastic and plastic deformation and cutting occurs due to plastic deformation with material separation. In practical cases, it is difficult to distinguish these three material removal mechanisms. With the help of single grit scratch tests these effects can be better understood than investigating an actual grinding process where several grits simultaneously engage onto the workpiece. Hence the pile-up area and groove area measured with the Nanofocus- μ surf Explorer confocal microscope provides deeper insight of the material removal mechanism undergoing in grinding. The material removal phases seem to be difficult to distinguish exactly but can be expressed as an influence on the contribution of material removal. If we assume that the cross-section profile of the scratch is kept constant along the scratch length (see schematic cross-sectional view of a scratch profile in 4.16). In ideal rubbing action, there should be no scratches on the surface ($P1+P2=0$, $GA=0$). In ideal plowing action, pile-up unit volume must be equal to the groove unit volume ($GA=P1+P2$), thus no material removal takes place with this action. In case of ideal cutting, the groove unit volume must equal to the removed material volume ($P1+P2=0$, $GA>0$), there should not exist pile-up material in the side of ground groove. Using this approach, the material removal mechanism is analyzed based on various input machine parameters such as tool geometry, depth of cut and linear speed in the next chapter.

The ground surface created by the single grit scratches is measured by a confocal microscope (Nanofocus- μ surf Explorer). To obtain more precise scratched topography, an optical measurement method is chosen and to avoid possible damage caused by a stylus (in case of tactile measurements). Confocal microscopy is chosen over conventional microscopy as it is a powerful tool that provide sharp images of a specimen that would be otherwise blurred. Also conventional microscopy does not provide 3D data, which is quite essential in determining the scratch topography. The goal of measuring the ground workpieces is to obtain a precise estimation of the pile up and groove areas. An image obtained from a confocal microscope has less haze and

better contrast. The basic principle of a confocal microscope is to reconstruct a 3D topography of a specimen after capturing multiple 2D images at different depths (also known as optical sectioning). Due to the non-contact measurement technique, a confocal microscope can give better feature information and extraction for scratches and pile-up than that obtained from stylus type instruments.

Fig.4.15 shows a measurement performed on a single grit scratched aluminum (A2024-T351) specimen. The main objective is to obtain the pile-up area ($P1+P2$), groove area (GA) and the undeformed chip thickness (a_p) as shown in Fig.4.16. The topographical measurements are performed at the middle region along the x direction of the scratched workpiece. This is because the scratching process is at a steady state and the depth of cut remain constant in this region. The measurement area is chosen to be $1600 \times 1600 \mu\text{m}^2$. The X, Y and Z co-ordinates of the measured scratched workpiece are extracted in an excel format along with microscopic images using the μsoft metrology software. The data is further processed with MATLAB to obtain an averaged 2D scratch profile and thereby calculate the pile-up and groove areas.



FIGURE 4.15: Optical measurement of ground surface topography

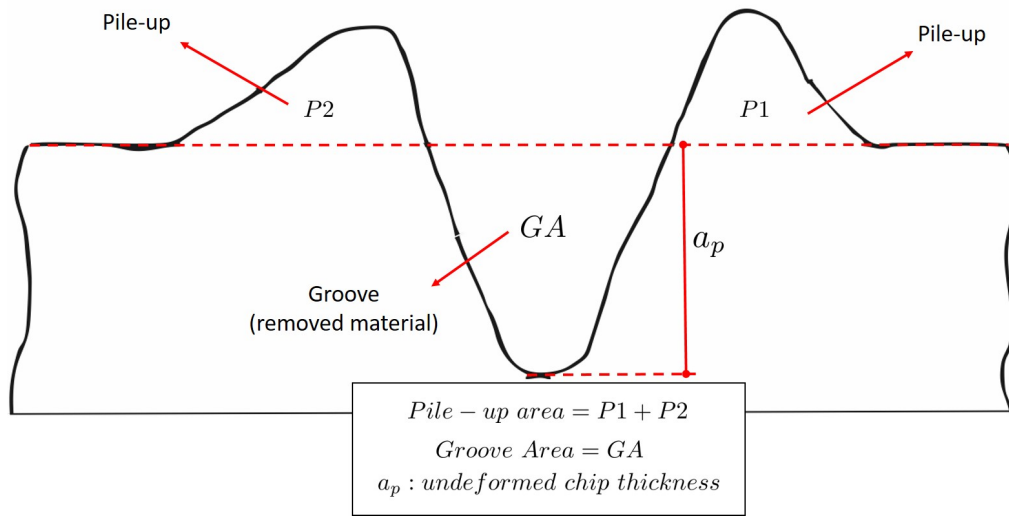


FIGURE 4.16: Schematic view of a scratch cross-section profile [82]

Fig.4.17A shows a 3D scratch topography of a single grit scratch test. From the figure, it can be observed that the variation of the height profile (z -axis) is along the scratch direction. So, the x coordinates need to be averaged along the scratch direction to obtain an averaged 2D scratch profile.

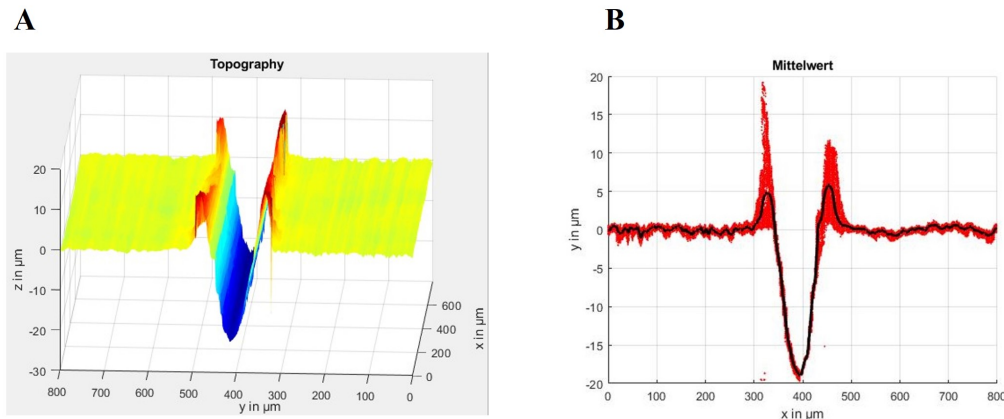


FIGURE 4.17: SST scratch profile; A: 3D SST scratch profile B: Averaged SST scratch profile

As shown in Fig.4.17B, the averaged z coordinates are plotted as a red scatter plot. A black line is fit along the scatter plot depicting the averaged values. Finally, in Fig.4.18, the zero line is plotted on the 2D scratch profile. The area measured over the zeroth line is the pile-up area and the area measured below is the groove area. Furthermore, the undeformed chip thickness is calculated for each scratch performed, by calculating the straight line distance between deepest point along the groove and the plotted zero line (ref Fig.4.18).

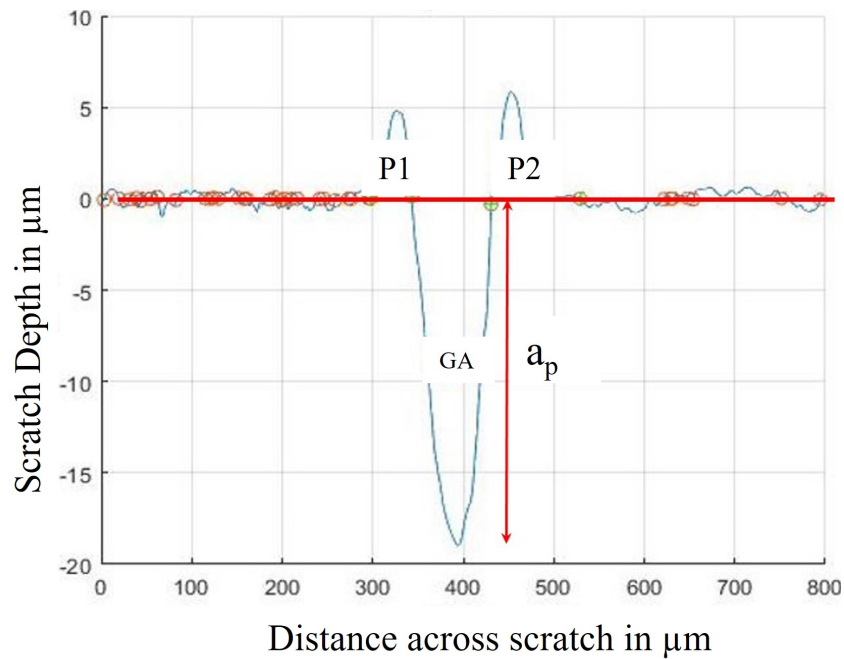


FIGURE 4.18: Post processing: SST

Fig.4.19A shows a 3D scratch topography of MPST. A similar method is used to extract the pile-up and groove areas as the SST. Fig.4.19 B shows the averaged 2D scratch profile for an MPST. Similarly, a zero line is plotted to calculate the groove and pile-up areas. The area above the zeroth line ($P1+P2+P3+P4+P5$) is calculated as the pile-up area and the area below the zeroth line is the groove area ($GA1+GA2+GA3$).

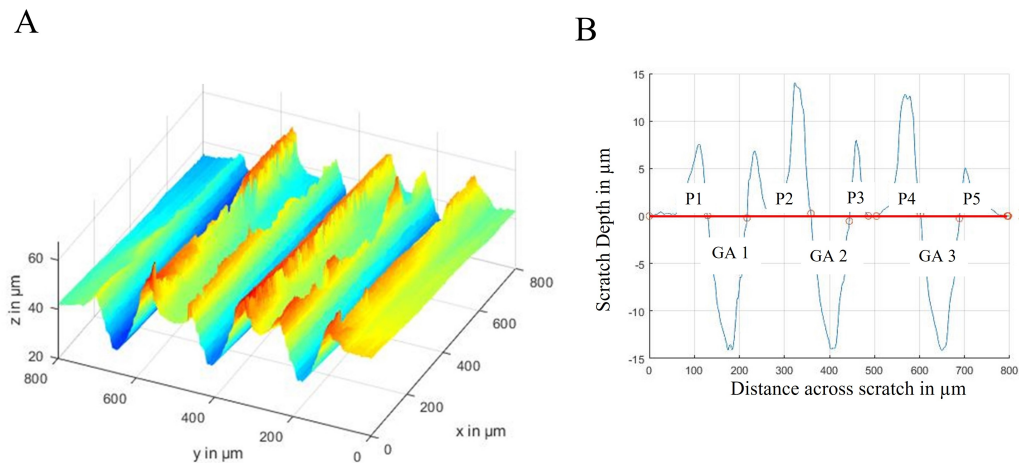


FIGURE 4.19: MPST scratch profile; A: 3D MPST scratch profile B: Averaged MPST scratch profile

4.5 Summary of single grit scratch experimental framework

In this chapter, the measurement framework and methodology followed in this research has been introduced. The grit grinding procedure has been described in terms of Single Scratch Tests (SST) and Multiple Pass Scratch Tests (MPST). The force sensors used for monitoring and recording a scratch process are described for single/multiple grit grinding. Finally, the topographical scratch surface measurement methods to analyze material removal mechanisms in single and multiple grit grinding are described.

Chapter 5

Experimental Results: Single and Multiple Grit Grinding

5.1 Introduction

To understand the fundamentals of the grinding process mechanisms at micro scale, single grit grinding experiments were performed. A grinding process could be thought of as the multiple interactions of several single grit operations on the workpiece [82, 127]. Thereby, performing single grit experiments provides crucial insights of the micro-mechanical material removal occurring in a grinding process. All the information regarding the experimental setup, methodology and conditions has been described in the previous chapter 4.

In this chapter, single grit experiments were performed on A2024-T351 aluminum workpiece. The single grit experiments were analyzed based on five output parameters namely, pile-up ratio, chip removal strength, effective grit engaging radius, process forces and specific energy exerted during scratching. The scratch experiments were analyzed by varying machine specific and tool specific factors. Looking at the machine specific factors, the influence of the different depth of cuts and cutting speeds on the scratches obtained were analyzed. The depth of cut is varied between 10 μm to 50 μm . The linear cutting speeds varied between 200 mm/s and 1000 mm/s. In terms of tool specific factors, the influence of the tool shape and the tool angles on scratches obtained were analyzed. Conical, pyramidal, and unshaped geometries were the tool shapes chosen to perform scratch experiments. For known tool shape geometries (conical and pyramidal indenters), grit angles of 105°, 120° and 135° were tested.

5.2 Material removal mechanisms in terms of pile-up ratio and chip removal strength

To describe the behavior of the material removal under different grit cutting edge geometries (conical, pyramidal and unshaped geometries), the output parameters pile-up ratio and chip removal strength are used as indicators. The pile up ratio is defined as the ratio of the pile-up area to groove area. Considering an average cross-section profile of a scratch along the scratched surface, as shown in Fig.4.16., the pile-up ratio can be calculated as

$$Pile - up\ ratio = \frac{Total\ pile - up\ area}{Total\ groove\ area} = \frac{P1 + P2}{GA} \quad (5.1)$$

The pile-up ratio indicates the most prominent material removal mechanism that takes place

during a single grit grinding. In case of a higher pile-up ratio, the material undergoes more prominent rubbing and plowing mechanisms. In case of a lower pile-up ratio, the material undergoes a prominent cutting mechanism. In theory, a lower pile-up ratio is preferred as it requires lower energy to remove a large volume of material.

The chip removal strength is a measure of material removal rate over the scratch cross-sectional area, similar to the calculation made by [82]. This is obtained by subtracting the total pile-up area from the total groove area.

$$\text{Chip Removal strength} = \text{Total groove area} - \text{Total pile - up area} \quad (5.2)$$

The experimental results are categorized into three sections based on grit edge geometries: conical geometries, pyramidal geometries, and unshaped geometries.

5.2.1 Pile-up ratio and chip removal strength for single scratches

This section explains the behavior of material removal under different grit cutting conditions. The experiments are performed with conical, pyramidal, and unshaped geometries - the output parameters pile-up ratio and chip removal strength are used as indicators.

Fig.5.1 shows that the variation of the pile-up ratio with respect to the depth of cut for conical, pyramidal and unshaped indent geometries. The scratches were performed at varying depth of cut (10 μm to 50 μm) at a constant linear speed of 200 mm/s. A similar tendency is observed for all grit geometries, where the pile-up ratio decreases with increasing depth of cut. With increasing depth of cut, there is an increase in the material removed and a prominent cutting mechanism. The material removal mechanism, if it is predominately rubbing, plowing, or cutting is influenced by the set depth of cut. This explains a lower pile-up ratio at a higher depth of cut and an inverse behavior at a lower depth of cut. The similar behavior is as also observed in the experiments performed by [82, 83].

In Fig.5.1 A and B, for the same depth of cut, cone angle 135° measures a lower pile-up ratio in comparison to cone angle 105°. This is due to the fact that the wider 135° indenter induces a higher compressive action producing smaller pile-up regions. The narrower 105° indenter at a higher depth of cut, produces a larger pile-up ratio as there is more sideways and forward material accumulation. Hence a cutting mechanism in the 135° indenter is more pronounced than the 105° indenter. This behavior is also confirmed by [83]. It can also be observed that pile-up ratios measured from the scratches performed with pyramidal indenters (Fig.5.1 B) is lower in comparison to the scratches performed with a conical indenters (Fig.5.1 A). As pyramidal indenter geometries have a wider cutting grit than conical indenter geometries, a lower pile-up ratio is measured. So, It can be concluded that material removal with wider pyramidal geometries offer a predominant cutting mechanism, especially at higher depths of cut. While comparing the measured pile-up ratio among all grit shapes and geometries, the 135° pyramidal indenter measures the least pile-up ratio. Confirming the grit shape and grit geometry have an influence on the material removal mechanism, this is also confirmed by [80, 84, 74]. From optical measurements performed on unshaped indenter grits, it is observed that grit angles measured lie between the range of 125°-140°. When comparing pile-up ratios of unshaped grit indenters (Fig.5.1 C) and pile-up ratios of 135° conical grit indenters (Fig.5.1 A), it can be observed that the pile-up ratios measured are in a similar range. Hence it can be inferred that the material removal mechanism behavior of unshaped geometry is similar to conical grits rather than pyramidal grits.

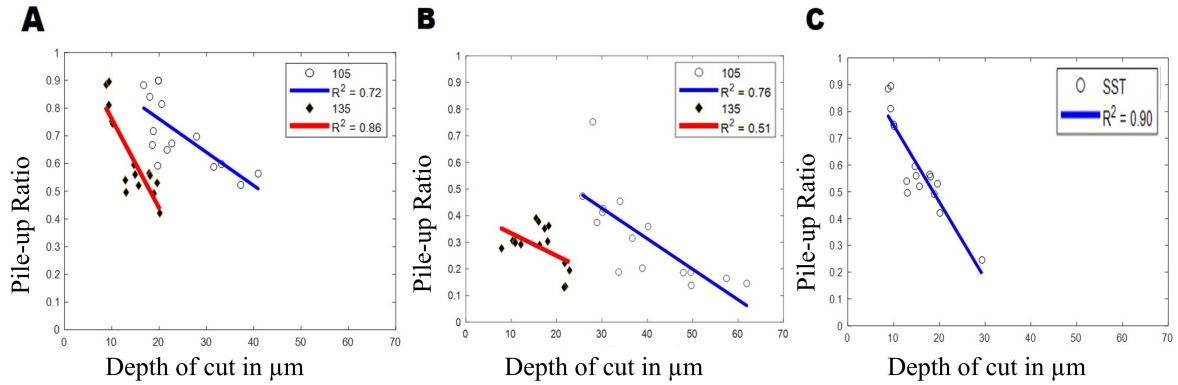


FIGURE 5.1: SST: Variation of the pile-up ratio with respect to depth of cut with A: conical grit; B: pyramidal grit; C: unshaped grit indenters for $V_c=200$ mm/s

In this section the change in pile-up ratio is studied with the scratch groove area measured. This investigation is performed to confirm that the above observed tendency of the pile-up ratio with change in the set depth of cut, is also observed here. On observing Fig.5.2, the pile up ratio decreases with increase in groove area for all grit geometries. Showing a similar trend as the change in pile up ratio with respect to depth of cut. The conical indenters as well as pyramidal indenters, with cone angle (105° and 135°) show a similar tendency. It is observed that, for the same groove area produced, the pile-up ratio is lower for the 135° indenter than the 105° indenter. It is also observed here that the wider 135° pyramidal indenter (Fig.5.2 B) produces a lower pile up ratio in comparison to the other tool shapes and geometries (Fig.5.2 A,C).

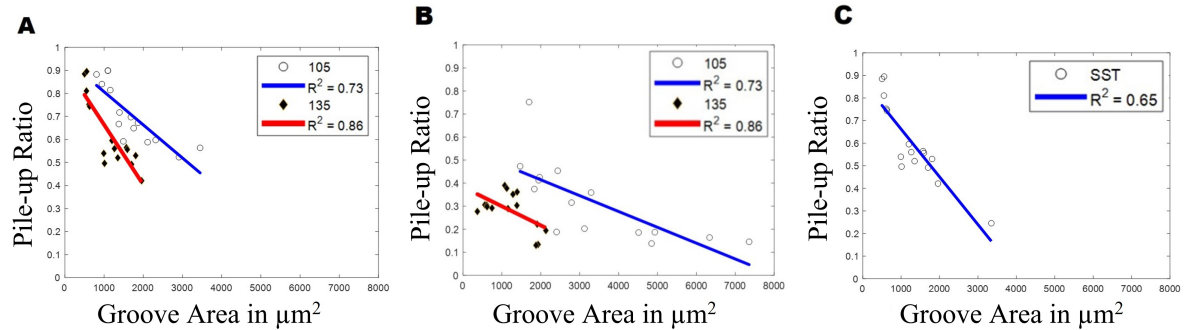


FIGURE 5.2: SST: Variation of the pile-up ratio with respect to groove area with A: conical grit; B: pyramidal grit; C: unshaped grit indenters for $V_c=200$ mm/s

Fig.5.3 in general shows that the chip removal strength increases with the increase in depth of cut for all grit shapes and geometries. Similar results are also reported by [82]. However, it can also be observed that the chip removal strength is dependent on the grit shape and geometry. In Fig.5.3 A, for the same depth of cut, wider 135° conical indenters measure a greater chip removal strength than the narrower 105° conical indenters. The reason is, as a wider conical indenter exerts a higher compressive action onto the workpiece, it produces a larger groove area and lower pile-up area. It can also be consequently inferred that the forces measured while scratching with a wider conical indenter are higher than a narrower indenter.

In Fig.5.3 B, depths of cut reached by the wider pyramidal 135° indenters are much lesser in comparison 105° indenters. It can be also inferred, that a wider indenter tool induces a larger force onto the workpiece. Also the blunt nature of a wider tool produces a lower depth of cut compared to narrower indenter tool. This is due to the low width to depth ratio of 135° pyramidal indenters. However from the results it can be extrapolated that for the same depth of cut, a wider pyramidal 135° indenter would measure a larger chip removal strength in comparison to a narrower 105° indenter. It can be also observed that the chip removal strength measured with the pyramidal indenters is higher than the conical indenters. This is attributed to the fact that the pyramidal geometry having a wider grit geometry produce a larger groove area in comparison to the conical geometries. Hence the chip removal strength is dependent on the grit apex angle as well as the grit shape.

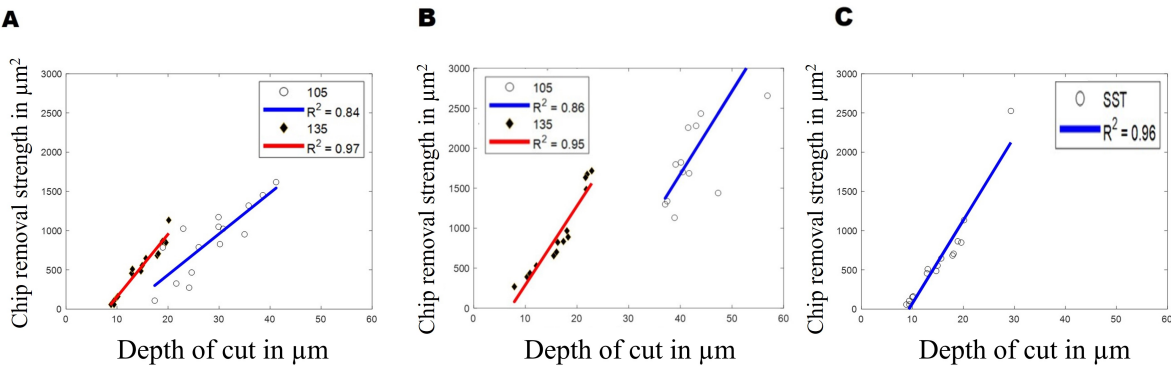


FIGURE 5.3: SST: Variation of the chip removal strength with respect to depth of cut with A: conical grit; B: pyramidal grit; C: unshaped grit indenters for $V_c=200$ mm/s

5.2.2 Pile-up ratio and chip removal strength for multiple scratches

As an extension to Single Scratch Tests (SST), another set of experiments were performed to produce multiple edge scratches. The multiple edge scratches are single scratches that are separated by a constant distance of 0.2 mm. Three scratch passes are performed with a constant separation distance to complete a Multiple Pass Scratch Test (MPST). The results were obtained by performing the scratch tests with 135° conical and pyramidal indenters. The scratches were performed at varying depth of cut (15 μm to 35 μm) at a constant linear speed of 200 mm/s.

Fig.5.4 shows the comparison of Single Edge Scratches (SST) in comparison to Multiple Pass Scratches (MPST) in terms of pile-up ratio for various depths of cut. The pile-up ratio of MPST is calculated as an average pile-up ratio calculated for each individual scratch performed as part of a MPST test. Like the SST, the pile-up ratio of MPST decreases with increase in depth of cut. This is attributed to an increased cutting mechanism occurring at higher depths of cut.

For all grit geometries, it is observed that for MPST, the pile-up ratio is higher than that of SST. The high pile-up ratio can be attributed to large pile-up of material at the middle region of the scratch as shown in Fig.5.5. This occurs due to the small separation distance between the scratches. Therefore, it is observed that for a same depth of cut, the MPST has a higher pile-up ratio than SST. This behavior is also confirmed by the experiments performed by [20, 82]

While comparing MPST pile-up ratios for pyramidal geometries (Fig.5.4B) with conical geometries (Fig.5.4A), it can be observed that pile-up ratios of pyramidal geometries are lesser in

comparison to conical geometries. This can be attributed to the wider cutting edge of pyramidal geometries, which induce a higher compressing action onto the work material. Hence there is a more significant cutting action, leading to production of higher grooves and lower pileups. This can be also clearly noticed at the overlap regions in Fig.5.5. This behavior also supports the argument placed before for SST, that pyramidal geometries are more efficient in material removal than conical geometry. Finally observing Fig.5.4C, the pile-up ratios measured for unshaped grit geometries are in the similar range as conical geometries, it can be inferred that the material removal behavior of unshaped grit geometry is similar to conical indenters.

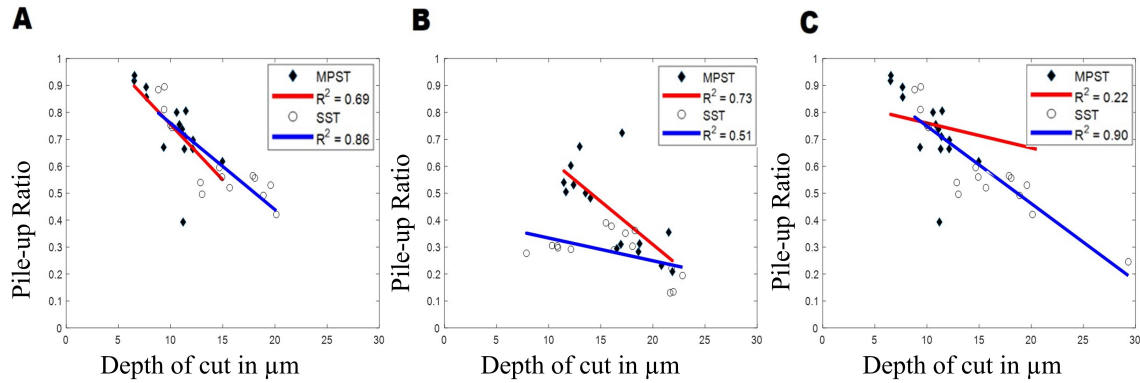


FIGURE 5.4: MPST: Variation of the pile-up ratio with respect to depth of cut with A: conical grit; B: pyramidal grit; C: unshaped grit indenters for $V_c=200$ mm/s

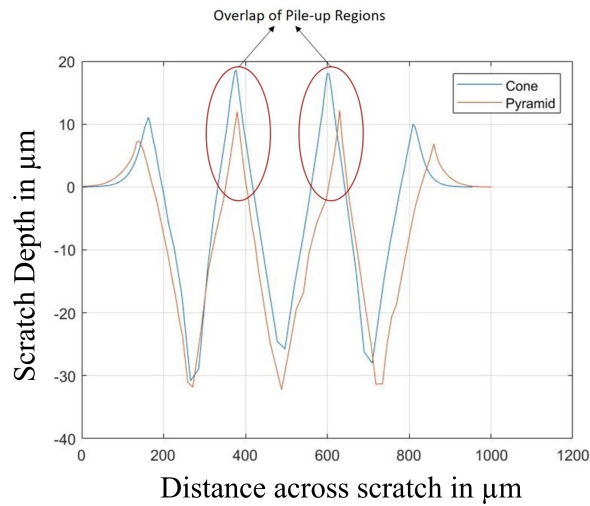


FIGURE 5.5: MPST scratch profile comparing scratches performed with pyramidal and conical indenters

In Fig.5.6 a similar tendency is observed, where the multiple pass scratches have a higher pile-up ratio than the single scratches with respect to the groove area for all grit geometries. It can also be observed that for grit geometries, the overall groove area produced by MPST is higher than that of SST, this obvious as material removed in MPST is higher than SST.

This investigation is performed to check if there are anomalies in tendencies of the pile-up ratio with respect to the output parameter-groove area. However the behavior is similar to the tendency as observed in Fig.5.4

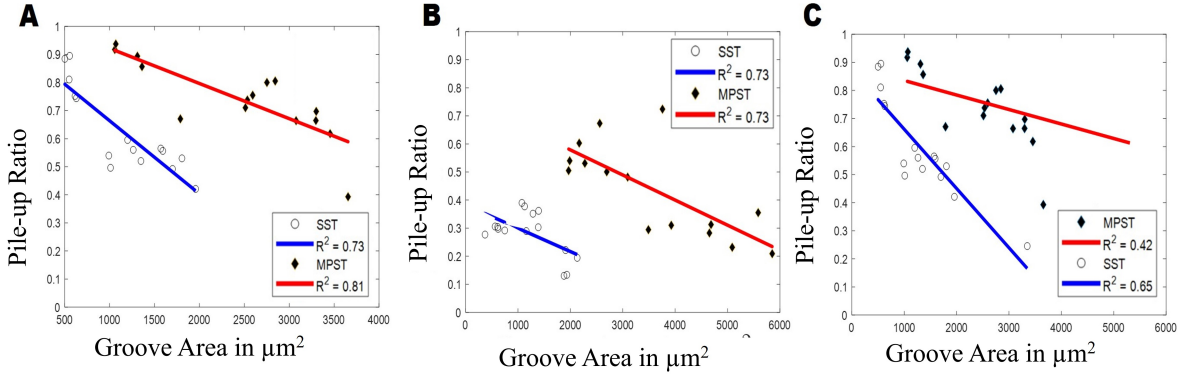


FIGURE 5.6: MPST: Variation of the pile-up ratio with respect to groove area with A: conical grit; B: pyramidal grit; C: unshaped grit indenters for $V_c=200$ mm/s

Subsequently, Fig.5.7 shows that for all grit geometries, chip removal strength is higher for SST compared to MPST. This behavior can be attributed because of high pileup ratios measured during MPST. This behavior is also confirmed by the experiments performed by [82, 20]. When comparing the chip removal strength in MPST between pyramidal (Fig.5.7A) and conical geometries (Fig.5.7A), it can be observed that the chip removal strength measured for pyramidal geometries is much higher in comparison to conical geometries. This can be attributed to the fact that a pyramidal indenter produces a more effective cutting action, generating larger grooves and smaller pileups.

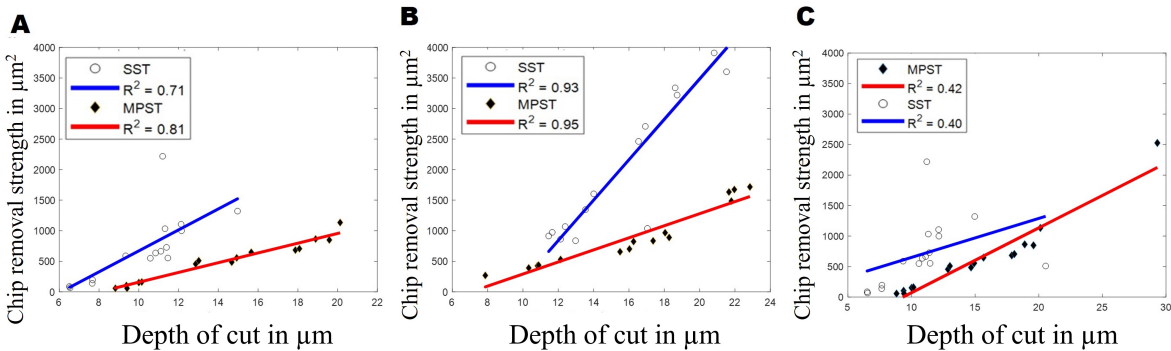


FIGURE 5.7: MPST: Variation of the chip removal strength with respect to depth of cut with A: conical grit; B: pyramidal grit; C: unshaped grit indenters for $V_c=200$ mm/s

5.3 Effective grit engaging radius

To understand the grinding mechanics in terms of contact variation, the Effective Grit Engaging Radius (EGER) is used, based on the calculations made by [82]. This assumes that the measured cross-sectional profile of a scratch can be represented as an arc of a circle, see Fig.5.8C, and the

radius of that arc is the EGER. The grit is assumed to have a spherical shape, defined by the nominal grit engaging radius with the workpiece at the time of contact. To calculate the width for individual scratch profiles, the points where the scratch depth is zero are selected. As observed in the Fig.5.8A and 5.8B arcs are drawn along the width of the groove profile, the radius of the drawn arc provides the EGER. In case of MPST (Fig.5.8B), three arcs are drawn along each of the groove profiles, the final EGER computed as the arithmetic mean of the individual EGERs, which deviates from the assumption made by [82], where a single arc along all three groove profiles is calculated as the EGER. The EGER predicts closely the contact radius between the grit and workpiece, for the scratch profiles produced by different grit shapes at varying depth of cuts. It should be noted that the EGER calculation approximates the contact condition between tool and workpiece to be spherical nature irrespective of the tool geometry (cone or pyramid), therefore certain deviations can be observed between the actual tool-workpiece condition and approximated EGER. Based on this approximation, the various tendencies of variation of contact condition with change in the scratch input parameters are captured. In future, the calculation can be adjusted to better approximate contact conditions based on individual tool geometries.

The tendencies are built from the experimental analysis in the further sections, which provides important insights on the material removal based on contact variation between the grit and workpiece.

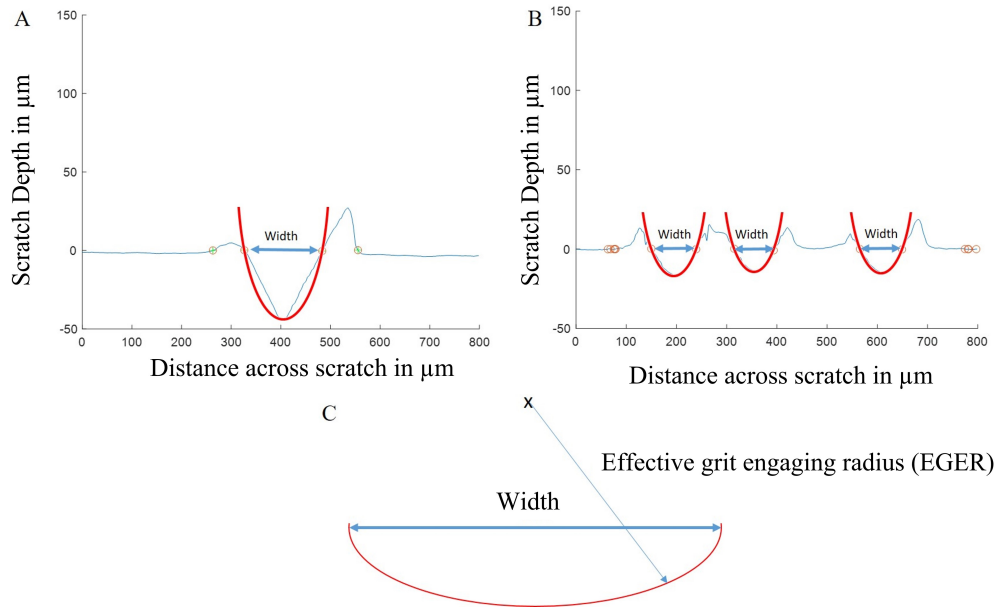


FIGURE 5.8: A: Measurement of EGER for single grit scratches, B: Measurement of EGER for multiple grit scratches C: Illustration of EGER calculation

5.3.1 Effective grit engaging radius for single scratches

In this section, the effective grit engaging radius is used as an indicator to understand the contact variation, while performing single edge scratch tests with conical edge geometries and pyramidal edge geometries (105° , 120° and 135°).

In Fig.5.9, the variation of EGER with the depth of cut is shown for conical and pyramidal indenters with cone angles 105° and 135° . It is observed that the EGER increases with the

increase in depth of cut, indicating that the grit is more in contact with the workpiece at a higher depth of cut. It is also observed that a wider 135° indenter has a higher EGER compared to a narrower 105° indenter, as the total surface area of a wider indenter is larger in comparison to a narrower indenter. Due to the increased tool-workpiece contact with a wider 135° indenter, a prevalent cutting mechanism takes place while scratching.

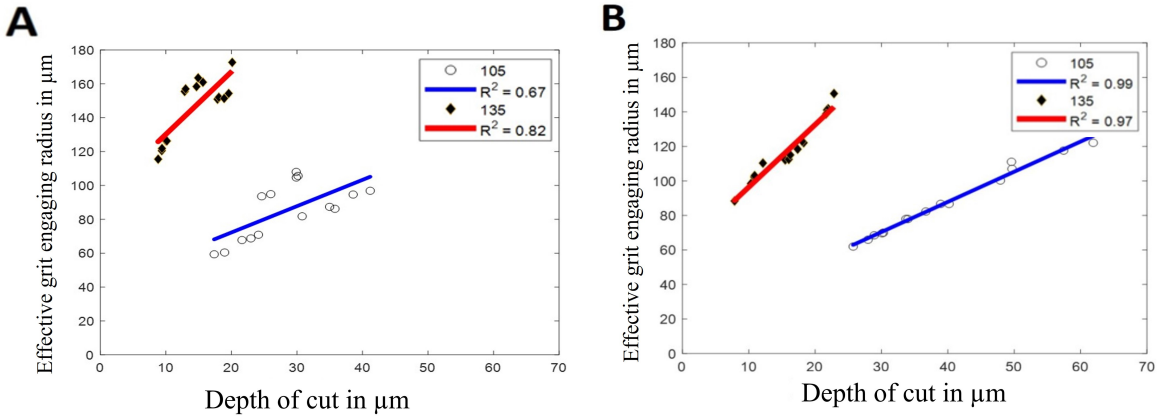


FIGURE 5.9: SST: Variation of the EGER with respect to depth of cut with A: conical grit; B: pyramidal grit for $V_c=200$ mm/s

Fig.5.10 presents the EGER relation with groove area and shows a similar trend with the depth of cut variation as shown in Fig.5.9. The above explanation holds true to the tendency of the measured EGER with respect to the groove area.

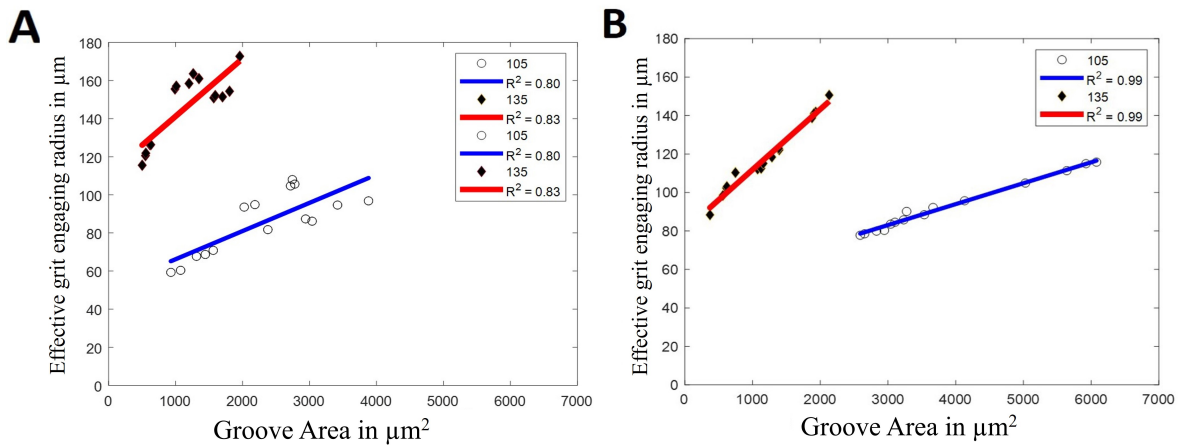


FIGURE 5.10: SST: Variation of the EGER with respect to groove area with A: conical grit; B: pyramidal grit for $V_c=200$ mm/s

In Fig.5.11 it can be observed that for both conical and pyramidal geometries, the pile-up ratio reduces with increase in EGER. This is a direct consequence of tendencies observed in Fig.5.10. A prevailing cutting mechanism occurs while scratching with a higher EGER, leading to a lower measure of pile-up ratio. It can also be observed that a wider indenter (135°) geometry measures a lower pile-up ratio at higher EGER. This behavior can be observed for both conical

and pyramidal indenters. This supports the observation done in the previous section that a wider indenter geometry produces a lower pile-up by inducing a higher compressive force onto the workpiece. Finally in Fig.5.11 B, pyramidal indenters, especially a wider 135° pyramidal indenter produces the least pile-up ratio at high EGER. Pyramidal geometry makes a larger tool-workpiece contact, this considerably increases its cutting efficiency.

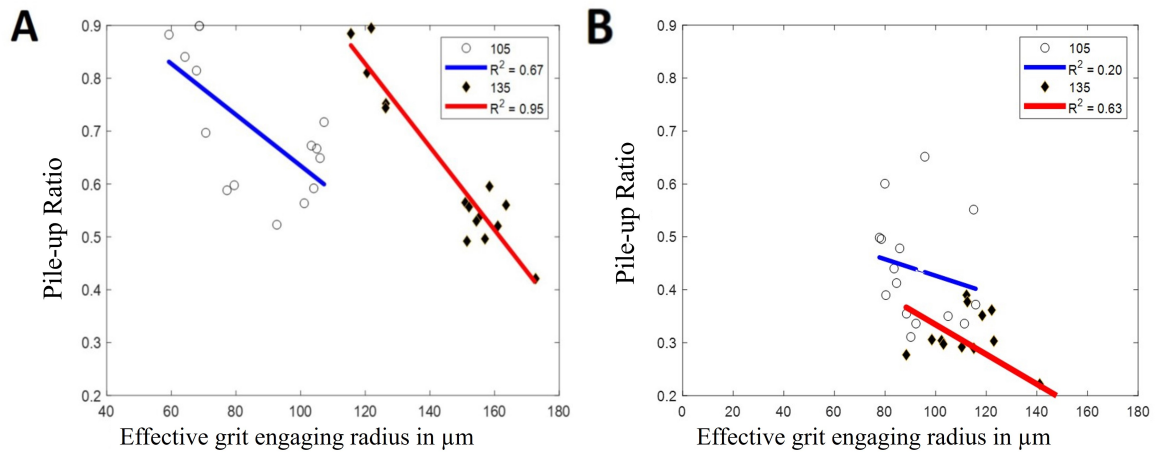


FIGURE 5.11: SST: Variation of the pile-up ratio with respect to EGER with A: conical grit; B: pyramidal grit for $V_c=200$ mm/s

5.3.2 Effective grit engaging radius for multiple scratches

The calculated value of the EGER is higher for similar depths of cut in the case of single edge scratches compared to multiple pass scratches, as shown in Fig.5.12. While performing multiple pass scratch tests, although there is more material removal than single edge scratch tests, there is also an increase in the pile up regions produced Fig.5.6. This reduces the effective contact between the grit and the workpiece and hence the MPST tests measure a lower EGER. This can be clearly observed in Fig.5.12, where the pile-up ratios of MPST is higher in comparison to SST.

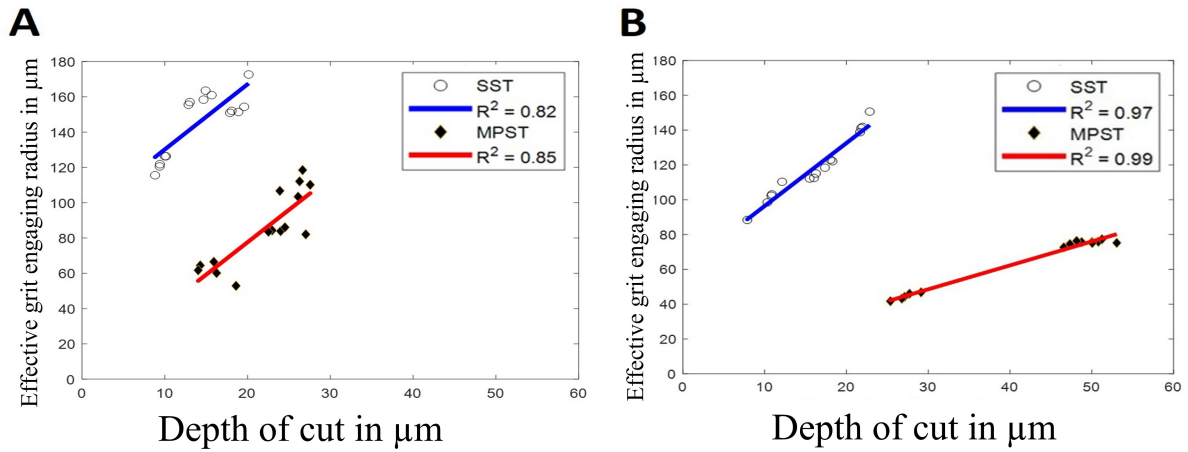


FIGURE 5.12: MPST: Variation of the EGER with respect to depth of cut with A: conical grit; B: pyramidal grit; C: unshaped grit indenters for $V_c=200$ mm/s

Pile-up ratio decreases with increasing EGER for both single edge scratches and multiple pass scratch tests as shown in Fig.5.13. This is because the cutting mechanism is more prominent with increasing EGER. It is observed that the pile-up ratio is higher for the multiple pass scratch test, and this is because of the small separation between the scratches leading to the accumulation of pile-up during overlap of the individual scratches. When comparing the pile-up ratio with respect to EGER, for MPST experiments of pyramidal and conical, geometries it can be observed that pyramidal geometries measure a lower pile-up ratio at high EGER, this shows that at increased tool-workpiece contact pyramidal geometries produces larger grooves and smaller pile-ups, in comparison to conical indenters.

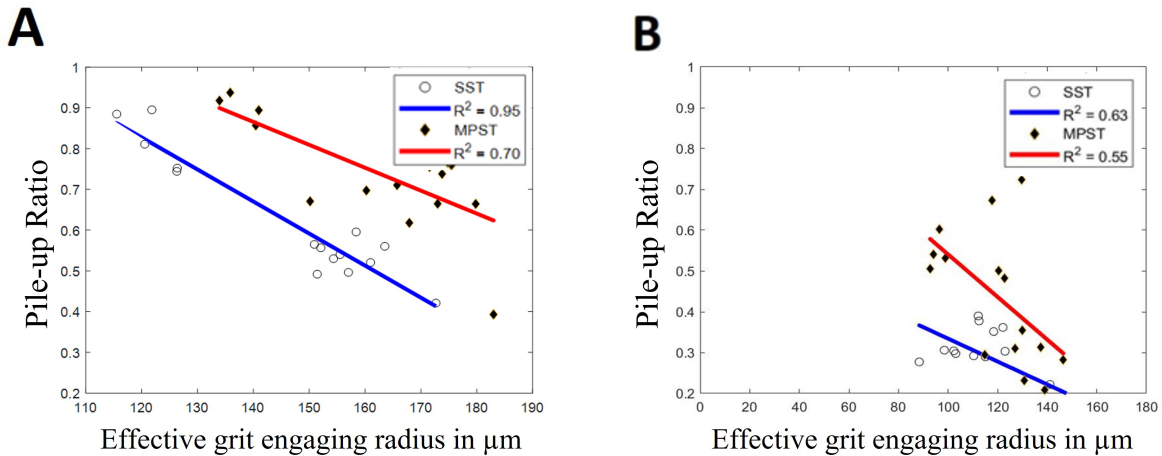


FIGURE 5.13: MPST: Variation of the pile-up ratio with respect to EGER with A: conical grit; B: pyramidal grit indenters for $V_c=200$ mm/s

5.4 Process forces during single grit grinding

In this section, the process forces (cutting forces F_c and passive forces F_n) are used as an indicator to analyze the scratch experiments performed at various depths of cut and linear speeds. The process force variation is also analyzed based on the change in indenter geometry (conical, pyramidal, and unshaped). The process forces are also analyzed based on two experimental methods, Single Scratch Tests (SST) and Multiple Pass Scratch Test (MPST).

5.4.1 Process forces vs linear speed

In this section, the variation of the process forces with the change in linear speed is described. Fig.5.14 and Fig.5.15 illustrate the change in passive forces and cutting forces generated when single grit scratch experiments were performed with a depth of cut of $35\ \mu\text{m}$ at cutting speeds of 200 mm/s, 400 mm/s, 600 mm/s, 800 mm/s and 1000 mm/s for the 105° and 120° conical indenters.

As shown in Fig.5.14 and Fig.5.15, both the passive force and the cutting force decrease with increasing cutting speed for different shapes and different tool angles of the conical abrasive grain. The reason for this is that at high cutting speeds, the cutting action is enhanced. This is due to an increased thermal softening effect that occurs at higher cutting speeds, that leads to pronounced cutting mechanism. Thus the process forces measured are lower at higher cutting speeds, similar observations are also made by [122, 31]. This trend can also be seen in tests with other indenters (pyramidal and unshaped grit indenters).

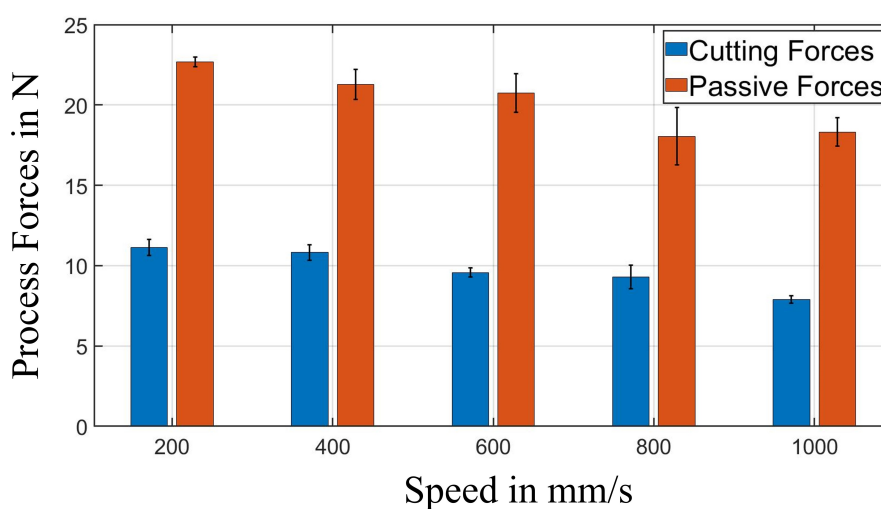


FIGURE 5.14: Process forces vs linear cutting speed with 105° conical indenter

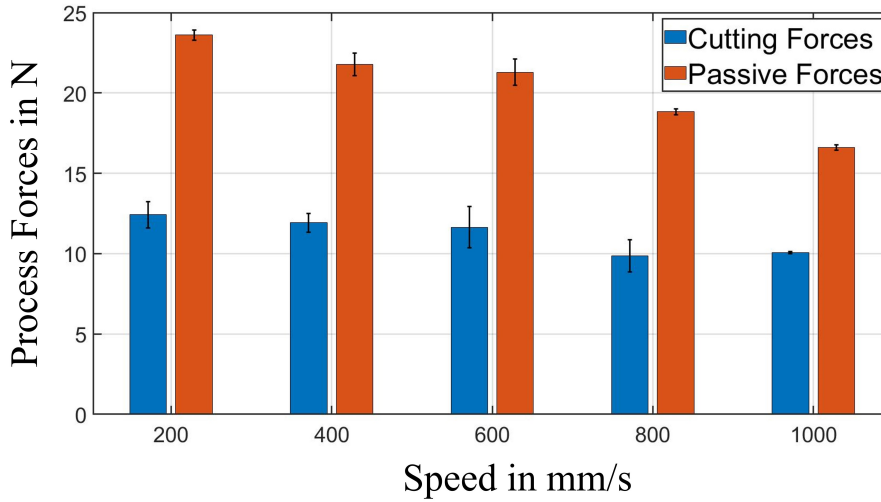


FIGURE 5.15: Process force vs linear cutting speed with 120° conical indenter

5.4.2 Process forces for single scratches

Under this section, the process forces are analyzed based on the scratch experiments performed with conical and pyramidal grit indenters with tool apex angles 105° and 135° , as shown in Fig.5.16 A and B. It is observed that the process forces increase with the increase in depth of cut. With the increase in the depth of cut, more material is removed from the workpiece. Hence, the process forces increase as well. It is observed that the cutting forces measured are smaller in comparison to the passive forces.

This tendency is commonly observed in material removal processes using cutting tools with a negative rake angle (for example, grinding). The single grit indenter exerts a higher compressive force onto the workpiece, explaining a larger measurement of passive forces. This behavior is also confirmed by the experiments performed by [84, 7, 35].

On comparing the process forces between the indenter (105° and 135°), it is observed that the indenter 135° measures a higher force. This is due to the fact that the resistance to material removal is higher when cutting with a tool with a higher rake angle. The wider 135° angle induces a higher compressive force in comparison to 105° , shown by the substantial increase in passive forces. It can be observed forces measured for both pyramidal and conical geometries lie in the same range.

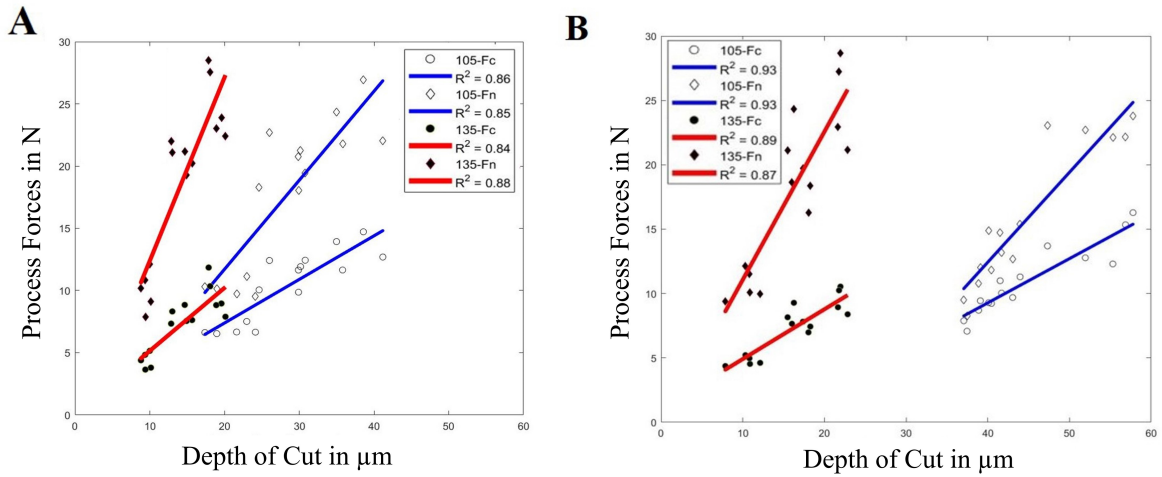


FIGURE 5.16: SST: Variation of the process forces with respect to depth of cut with A: conical grit; B: pyramidal grit for $V_c=200$ mm/s

Fig.5.17 shows a similar tendency as above. For both the conical and pyramidal indenters, the process forces increase with the increase in the groove area produced. It is observed for both conical and pyramidal geometries, for the same groove area produced the process forces measured with a wider indenter is higher. This is attributed to the fact that a wider geometry of 135° induces a higher compressive force onto the workpiece. Although 135° measures a lower pile-up ratio, it requires a higher force or higher energy to remove material in comparison to 105° .

When comparing Fig.5.17 A and Fig.5.17 B, it can be observed that the groove area produced by the pyramidal indenters are slightly larger in comparison to conical indenters for a same depth of cut, indicating that the pyramidal indenters are more efficient in removing material.

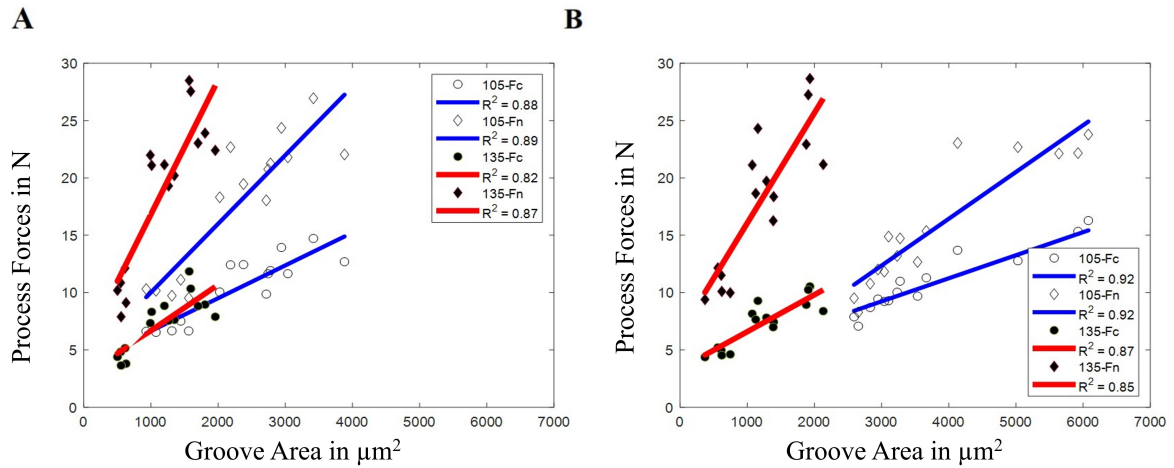


FIGURE 5.17: SST: Variation of the process forces with respect to groove area with A: conical grit; B: pyramidal grit for $V_c=200$ mm/s

The force ratio (F_c/F_n) is calculated as the ratio of cutting forces to passive forces, based on the calculation made by [96]. This value is also like the friction coefficient [96]. The calculated force ratio is associated with the efficiency of grinding/scratching. The higher the ratio the more

efficient is the material removal. In Fig.5.18, it is observed that the force ratio decreases with the increase in groove area for both conical and pyramidal indenters. As observed, the force ratio measured for pyramidal geometries are slightly larger in comparison to conical geometries. This is because the sharper pyramidal indenters measure a slightly higher tangential force in comparison to conical geometries. While considering the experiments performed at lower groove areas, the 135° pyramidal indenters measure the highest force ratio and thereby is more efficient in material removal in comparison to the other indenter geometries. It can be also inferred that the wider indenter geometries measure a lower force ratio/friction co-efficient at higher comparable groove areas.

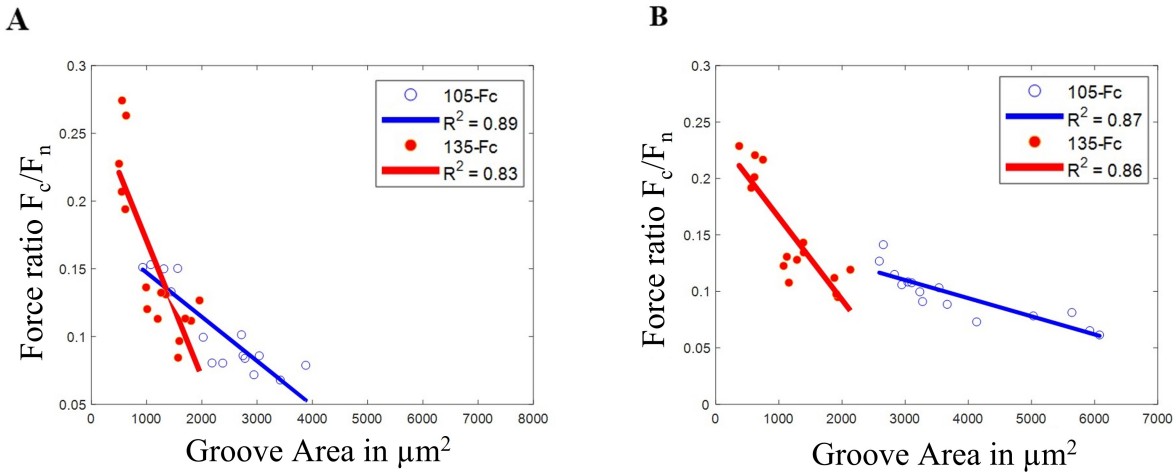


FIGURE 5.18: SST: Variation of the force ratio with respect to groove area with A: conical grit; B: pyramidal grit for $V_c=200$ mm/s

5.4.3 Process forces for multiple pass scratches

Process forces obtained from single pass scratches and multiple pass scratches for conical, pyramidal and unshaped geometries are shown in Fig.5.19 for different depths of cut. For MPST experiments, the forces are averaged for the three scratches performed. It is observed that, irrespective of the tool geometry, for both SST and MPST, the process forces increase with increase in the depth of cut. The process forces calculated for MPST is the average of the forces measured while performing the three individual scratches. The process forces measured for the MPST is slightly larger than the process forces measured for SST. This is because the plowing mechanism is more prominent while performing MPST, leading to a larger measure of the process forces. plowing is an undesired action in grinding since it consumes extra energy during the material removal process. The above observations is also seen in the experiments performed by [84, 20].

Observing Fig.5.19 A and C, it can be seen that the force measured is in the similar range for various depths of cut. This shows that geometry and the material removal mechanism is similar for conical and unshaped geometries. When observing Fig.5.19 B it can be observed that the forces measured using the pyramidal shaped indenter is smaller in comparison to conical and unshaped geometries for MPSTs. This again reaffirms previous observations, that the pyramidal indenter has better cutting performance.

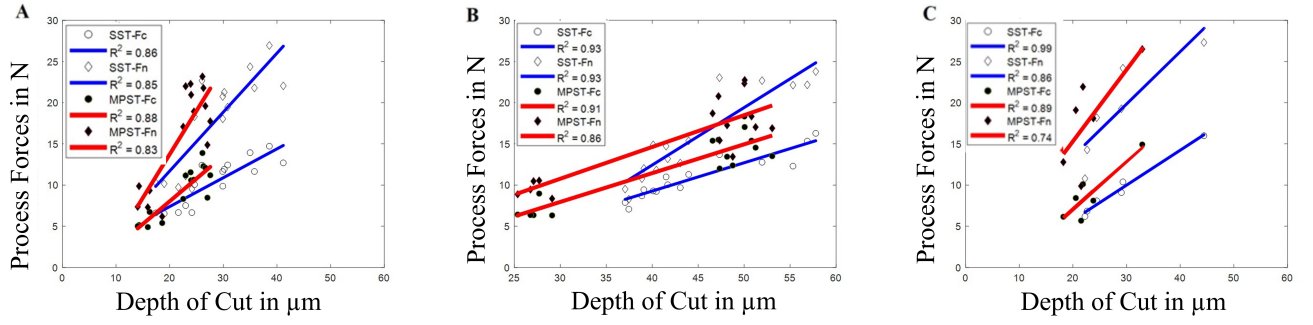


FIGURE 5.19: MPST: Variation of the process forces with respect to depth of cut with A: conical grit; B: pyramidal grit; C: unshaped grit indenters for $V_c=200$ mm/s

Fig.5.20 shows the variation of process forces with respect to the groove area for SST and MPST for conical, pyramidal and unshaped geometries. It is observed that, irrespective of the tool geometry, the groove area produced by MPST is larger than SST, while measuring higher process forces in comparison to SST. Although MPSTs obviously produce a larger groove area, there are also higher forces measured. This is due to the increase plowing and production of overlap pile-up areas as seen in Fig.5.5.

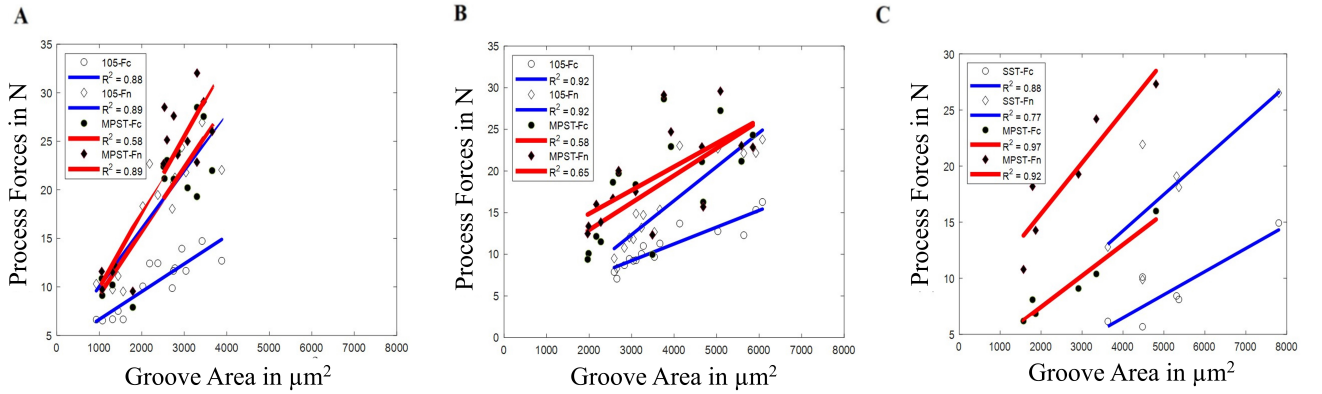


FIGURE 5.20: MPST: Variation of the process forces with respect to groove area with A: conical grit; B: pyramidal grit; C: unshaped grit indenters for $V_c=200$ mm/s

5.5 Specific energy in single grit grinding

Specific energy can be defined as the energy required to remove one unit volume of material [38, 18]. To study the change in energy lost when scratching the material, specific energy calculation is helpful. The specific energy (u) for the single grit grinding process can be expressed as

$$u = \frac{F_c}{GA} \quad (5.3)$$

This equation is a concise form of specific energy used in this thesis derived from Grinding Power (P) and Material Removal Rate (MRR). The amount of material removed from the workpiece per unit of time is known as the material removal rate [38]. Where F_c is the cutting

force, GA is the groove cross sectional area and V_c is the cutting speed.

$$u = \frac{P}{MRR} = \frac{F_c \cdot V_c}{GA \cdot V_c} \quad (5.4)$$

In earlier studies, the ratio of the cutting force to the cross-section area of the groove was used to calculate the specific energy in single grit grinding [15, 33].

In case of calculation of specific energy for MPST experiments, the following formulae is employed:

$$u = \frac{\sum F_c}{\sum GA} \quad (5.5)$$

where the groove area and the respective cutting forces for three consecutive scratches are summed to extract the specific energy. Under this section, specific energy is used as an indicator to analyze the variation based on the depth of cut and groove area for different cutting grit geometries (conical, pyramidal, and unshaped).

5.5.1 Specific energy for single scratches

Under this section, specific energy is analyzed based on the single scratch experiments performed for conical and pyramidal indenters.

Fig.5.21 shows the variation of the specific energy with respect to different depths of cut. It is observed that the specific energy reduces with increase in depth of cut for both 105° and 135° indenters. Even though the cutting forces increase with the increase in the depth of cut, the increase in the groove area is larger. This causes the specific energy of cutting to drop with the increase in depth of cut. Similar behavior is confirmed by the experiments performed by [82, 26, 102].

On comparing the specific energies between the 105° and 135° indenters, the specific energy measured for the blunter (wider) 135° is higher. While scratching with the blunter 135° conical angle, the cutting forces generated are higher even-though amount of material removed is less. This affirms the statement from [5], that the specific energy decreases with reduction in undeformed chip thickness.

While observing Fig.5.21 A, for the same depth of cut, a wider tool measures a lower specific energy in comparison to a narrower tool. This is because the pile-up ratio measured for wider indenters is lesser than narrower indenters. The frictional coefficient at a higher depth of cut is less in comparison to narrower indenters. This affirms that wider indenters are more efficient in material removal in comparison to narrower indenter geometries. While observing Fig.5.21 B, for 105° pyramidal indenter specific energy is lower in comparison to 105° conical indenter Fig.5.21 A. This reaffirms that the pyramidal indenter has a better cutting performance as it removes a same amount of material using lower energy.

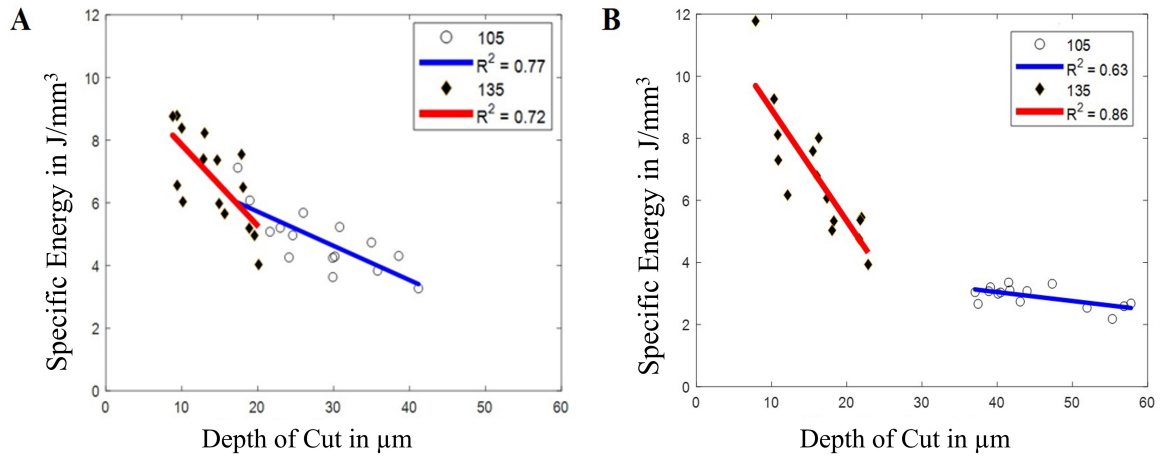


FIGURE 5.21: SST: Variation of the specific energy with respect to depth of cut with A: conical grit; B: pyramidal grit indenters for $V_c=200$ mm/s

Fig.5.22 shows the variation of specific energy with respect to the groove area. A similar tendency is observed as seen Fig.5.21. The specific energy decreases with the increase in the groove area. This is because the specific energy is inversely proportional to the groove area. It can be also observed that the 135° indenter is more efficient as predominantly less energy consuming cutting mechanism takes place while scratching, as lower pile-up areas are measured with wider indenter geometries while scratching at higher groove areas. Also while observing Fig.5.21 B, it is quite evident that especially 105° pyramidal indenter produces a much larger groove area in comparison to a 105° conical indenter consuming lower energy.

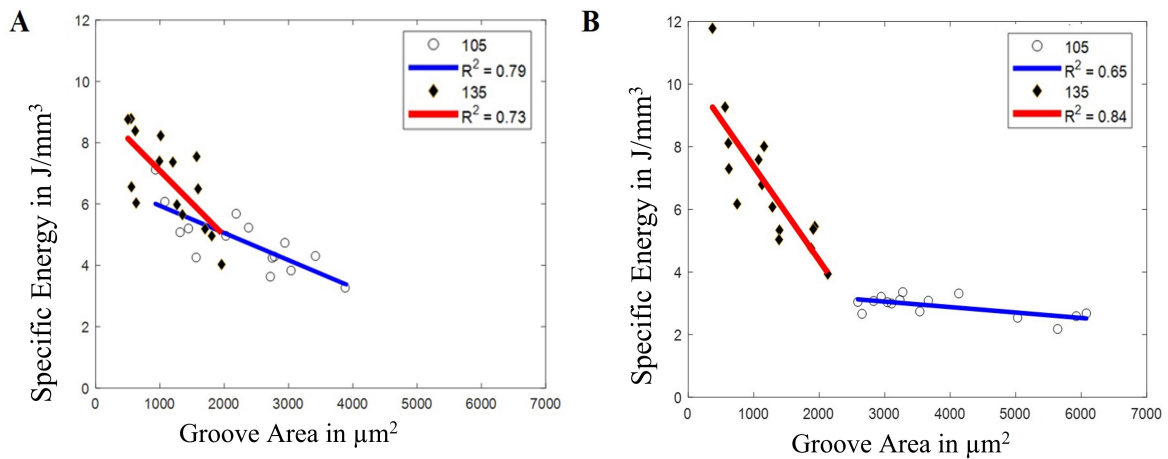


FIGURE 5.22: SST: Variation of the specific energy with respect to groove area with A: conical grit; B: pyramidal grit indenters for $V_c=200$ mm/s

5.5.2 Specific energy for multiple pass scratches

The specific energy calculated for a MPST experiment is the average of the specific energies of the three individual scratches performed. Fig.5.23 compares the specific energy between SST and MPST with respect to the depth of cut, a similar tendency as shown in Fig.5.21 is observed,

where the specific energy decreases with the increase in the depth of cut. It is also observed that MPST measures a higher specific energy in comparison to SST. This behavior is confirmed by [82].

Although there is more amount of material removed in MPST, the multiple edge scratches have more plowing action than cutting compared to single edge scratches. Also due to the interaction between the individual scratches as seen in Fig.5.5, overlapped pile-up regions are produced adding to the plowing effect. This leads to a higher measurement of specific energy in MSPTs compared to SSTs.

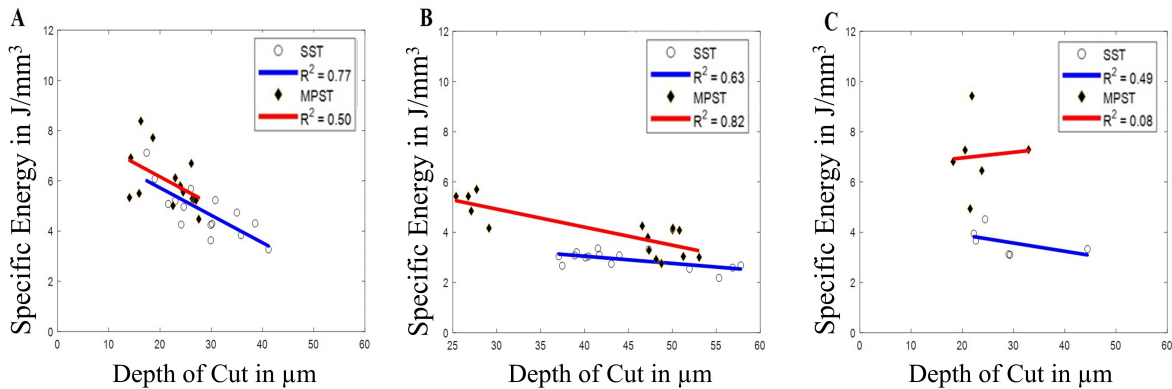


FIGURE 5.23: MPST: Variation of the specific energy with respect to depth of cut with A: conical grit; B: pyramidal grit; C: unshaped grit indenters for $V_c=200$ mm/s

In Fig.5.24, a clearer tendency is observed where the specific energy required for MPST is higher than SST. It is observed that even though the groove area measured for MPST is higher, the specific energy is higher than that of SST. This is because of the increased plowing action in MPST, and the measured cutting force is higher in comparison to SST. In Fig.5.23 B the MPST specific energy measured for pyramid indenters is much lesser than the conical and unshaped indenters. This confirms that the overall energy consumption to remove material is lesser in pyramidal geometries.

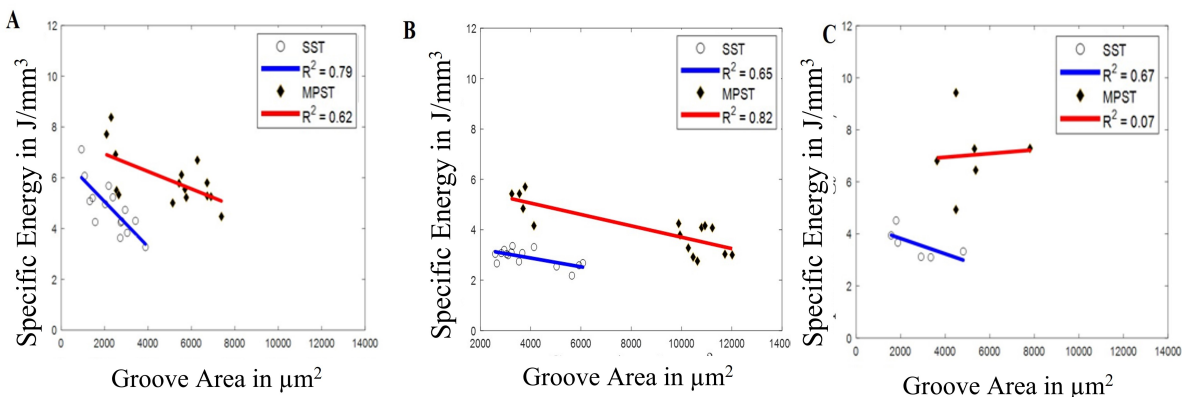


FIGURE 5.24: MPST: Variation of the specific energy with respect to groove area with A: conical grit; B: pyramidal grit; C: unshaped grit indenters for $V_c=200$ mm/s

5.5.3 Summary of single grit scratch experimental investigations

In this chapter, single and multiple pass scratch experiments were performed on A2024-T351. The experimental results show how the output parameters such as process forces, specific energy, pile-up ratio, chip removal strength and EGER are influenced during the process. The first quarter of the experimental results chapter investigates the material removal mechanism in terms of pile-up ratio, chip removal strength and EGER at the micro scale, followed by investigation of process forces and specific energy during scratching at various depths of cut, linear speeds and grit cutting geometries. All these factors show how a single grit grinding process has a highly complex material removal mechanism in comparison to orthogonal cutting operations.

According to the experimental results, pile-up ratio decreases with increase in the depth cut for all single grit cutting shapes (conical, pyramidal and unshaped geometries) as confirmed by [100, 84, 20]. On comparing the results based on the tool angles, a wider cutting edge leads to a lower pile-up ratio while a narrower cutting edge leads to a higher pile-up ratio. This is because of the small width of cross-section that makes the cutting edge behave as though it were sharp compared to cutting edges having a larger width. A wider tool thereby induces a higher compressive force and produces a lower pile-up. It is also observed that in general a wider tool geometry removes lesser material in comparison to narrower geometries, this also causes production of lower pileups. Pile-up ratio is found to be always higher with multiple grit scratches compared to single grit scratches. At lower depth of cut, a high pile-up ratio means the material removal is dominated by rubbing/plowing mechanism. It is also observed that the pyramidal indenters measure a lower pile-up ration in comparison to other geometrical grit indenters.

Chip removal strength increases with the increase in depth of cut as confirmed by [84, 20, 82]. Chip removal strength with respect to the depth of cut also represents a situation where plowing and cutting are prominent at high depth of cuts. A smaller slope in the chip removal trend can be interpreted as a plowing prominent region while a steep increase in the chip removal trend could be interpreted as a cutting prominent region. From the experimental results it is quite clear that the pyramidal indenters display a steeper slope of the chip removal strength in comparison to the other indenters.

Passive forces (F_n) exerted during single grit scratching were found to be always higher than cutting forces (F_c) as confirmed by [84, 7, 35]. Both forces are also found to be highly dependent on cutting speed, with higher cutting speed leading to lower process forces measured, refer Fig.5.14 and Fig.5.15. This behavior is also confirmed in the experiments performed by [84, 102, 101]. Both the process forces increase with increasing depth of cut and the cross sectional groove area measured for all grit cutting geometries (conical, pyramidal and unshaped) as confirmed by [84, 20, 3]. The force ratio (F_n/F_c) is generally found in the range of 4 to 16, but the ratio increases slightly with increasing groove area due to a faster rate of increase of the passive force with the depth of cut (see Fig.5.18) [82, 50].

Specific energy decreases with increase in the depth of cut (or groove area) for all cutting grit geometries (conical, pyramidal and unshaped) as observed by [82, 26, 50]. Specific energy requirement is found to be lower while performing the Single Scratch Test (SST), cutting action is efficient. However, the specific energy requirement increases while performing Multiple Pass Scratch Test (MPST), where cutting is less efficient. High pile-up areas are generated due to the interaction between the individual scratches (refer Fig.5.23 and Fig.5.24). It can be also inferred that a pyramidal indenter measures a lower specific energy compared to the other indenter geometries.

Chapter 6

Simulations: Grit-Workpiece Approach

6.1 Introduction

Simulating dynamic machining processes by simplifying the real system is quite commonly used to predict machine behavior and to understand the influence of machining parameters on both, tool and workpiece [15, 67, 68, 82]. With increasing computational power, it has become easier to solve complex problems such as abrasive grit-workpiece interactions [82, 94, 106]. A well-designed simulation model of the grinding wheel could largely reduce the cost of experimentation and help successfully determine the grinding process behavior based on the surface finish of the machined part, workpiece characteristics, material removal mechanisms, and tool wear [82, 62, 121]. In addition, simulations are able to provide some extra information like stresses, strains, strain rates, and temperature gradients, which are otherwise extremely difficult to determine by experimental investigations [82, 121, 109]. As grinding is one of the most complex machining processes, there is no universal model to comprehensively predict the machining behavior in terms of the grinding forces, material removal, and surface finish [36, 59].

Finite element simulation of machining processes in this thesis refers to simulation of single grit grinding at the micro-scale, where the depth of cut is in the order of 20 μm [82, 121, 109]. This is not a straight-forward simulation and is dissimilar to conventional machining simulation, which has a deeper cut. During the grinding process, numerous abrasive grits, which are bonded onto the grinding wheel with an arbitrary orientation, interact with the workpiece material. So, the interactions of workpiece and grit during grinding can be considered as having a different geometry of interaction at every grit-workpiece engagement. Single grit simulations are valuable not only to validate the single grit scratch experiments, but also to provide valuable insights of the material removal mechanisms that are unable to find out with experiments. Single grit grinding simulation should represent rubbing, plowing, and cutting phenomena, because three material removal phases occur at every grit-workpiece interaction in grinding.

In this thesis, the FEM single grit simulation model is developed in four phases as shown in Fig. 6.1. In the first phase, a 2D orthogonal cutting model is used to understand the cutting mechanisms and the effect of the rake angle, especially high negative tool rake angles as observed in grinding processes. The 2D orthogonal cutting model is employed to initially test the various mesh discretization methods. Two mesh-based methods Lagrangian (LAG) and Arbitrary Lagrangian Eulerian (ALE), and a particle based methods Smooth Particle Hydrodynamics (SPH) are used to perform 2D orthogonal cutting model. The 2D model is used as a foundation to develop the 3D scratch model.

In the second phase, a 3D model is developed to incorporate the rubbing and plowing mechanisms

in the FEM model. The 3D scratch model also tests three discretization methods LAG, ALE and SPH to find out which discretizational approach is most suitable to model a scratch process. The model is validated based on the process forces and topographical measurements obtained from experiments. The 3D model is tested to understand the effect of tool geometries. The 3D model is further extended and scaled up to simulate multiple pass scratch tests and are validated with the experiments performed as described in the previous chapter. The simulation frameworks and results of the 2D and 3D simulations are explained in detail in this chapter. The first and second phases are developed based on the grit-workpiece approach.

In the third phase, a virtual wheel model is developed using a through the process approach. A precise simulation of the steps involved in making a grinding wheel, from modeling the raw material through compression, sintering, and dressing to produce the finished grinding surface. The sample virtual grinding wheel model that was obtained is utilized as a digital twin to simulate the removal of material from a grinding process using FEM.

In the fourth and final phase, a simulation model is developed to simulate an up-cut surface grinding operation with a flat grinding wheel surface. This concludes the development cycle of the simulation models, scaling up from grit-workpiece models to wheel workpiece models. The description and results of third and fourth phase simulation models are described in the next chapter.

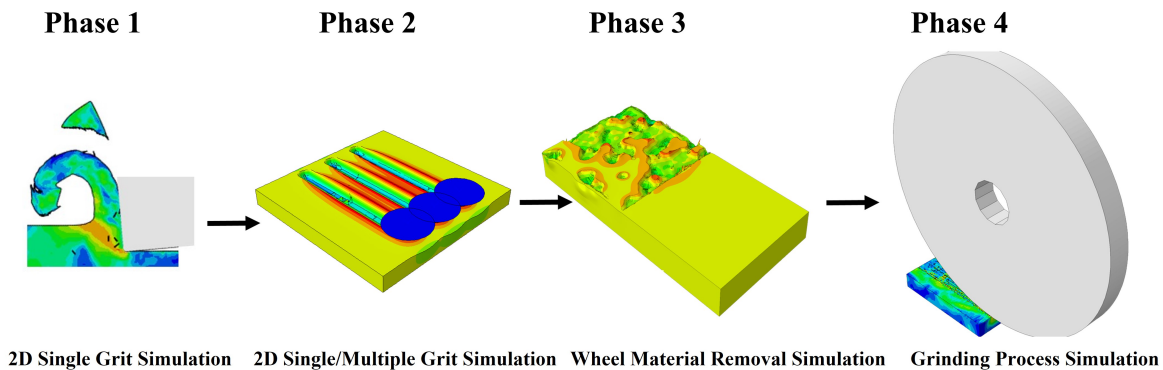


FIGURE 6.1: Simulation model development phases

6.2 Discretizational approaches

An overview of the mesh-based discretizational approaches (LAG and ALE) and particle-based discretizational approaches (SPH) is given before the simulation frameworks for the 2D, and 3D scratch models are discussed.

6.2.1 Mesh based discretizational approaches

Numerous solid mechanics issues have been solved using the Lagrangian (LAG) method. In the simulation, the displacement vector tracks each individual material point. The method is unable to follow significant deformations in simulations of metal cutting, which could result in simulation failures. However, several workable solutions, such as element elimination and adaptive re-meshing, were implemented in [110, 75, 25, 82]. The loss of material mass is a disadvantage

of the element elimination process, though. When adaptive re-meshing is used, there may be inconsistencies in the numerical outcomes of the simulation due to the mapping of internal variables from an old mesh to a new mesh.

The Arbitrary Lagrange Eulerian (ALE) approach does not consider the mesh to be constrained to a fixed domain (Eulerian) or that it moves along with material points (LAG). This approach aims at maintaining the mesh topology and prevents the division of mesh elements. Relocation of nodal positions of the mesh is performed by means of a mesh smoothing algorithm [81, 104]. This algorithm prevents mesh distortion and hour glassing. Despite the fact that ALE method is computationally efficient, its accuracy is dependent on the underlying mesh and the chosen smoothing algorithm [13, 110].

6.2.2 Particle based method

The meshless Smooth Particle Hydrodynamics (SPH) [65, 63] method significantly varies from the aforementioned mesh-based methodologies in terms of its underlying theory. In this method, spheres are used to represent the material domain. Strong particle-particle connections in solids and weak particle-particle connections in liquids are caused by this material domain. The SPH approach uses a weighted function to calculate a particle's physical quantity depending on the physical quantities of the surrounding particle and of the particle itself. The smoothing lengths and particle radius are taken into consideration by the weighted function [79]. A failure criterion is no longer required due to the particles' breakable bonds. Material separation results from the breakdown of cohesiveness between particles.

6.3 Simulation Workflow

Under this section a brief overview of the FEM models developed (2D orthogonal cutting model and 3D scratch model) is described. The sections 6.3.2 and 6.3.3 also provide information of the choice of the plasticity material model, the damage model and the friction contact model.

6.3.1 Simulation models

A 2D orthogonal cutting model and a 3D scratch model employed as part of this study were developed using Abaqus/Explicit. The simulation workflow and results of aforementioned 2D and 3D simulation models are based on a previously published scientific journal [107].

The main description of the cutting mechanism is given by a 2D orthogonal cutting model. The two mesh-based approaches ALE and LAG, as well as a particle-based approach SPH, are used to discretize this model. Section 6.4 provides a detailed explanation of the simulation settings for the workpiece, cutting tool, and boundary conditions [107].

The rubbing, plowing, and cutting mechanisms commonly present in a grinding/single grit scratching process are described using a 3D scratch model. The discretizational methods LAG, ALE, and SPH are employed to create a 3D scratch model. Section 6.5 provides a detailed explanation of the simulation settings for the workpiece, cutting tool, and boundary conditions [107].

6.3.2 Material model

Large plastic stresses and high deformation rates occur in the workpiece material during material removal in ductile materials. Complicated material removal processes like rubbing, plowing, and cutting manifest during grinding and scratching. A material model describing such material behavior is the Johnson-Cook material model [46, 45], with its mathematical description of the effective von Mises stress $\bar{\sigma}$

$$\bar{\sigma} = \underbrace{[A + B(\varepsilon)^n]}_{f_1} \cdot \underbrace{\left[1 + C \ln \left(\frac{\dot{\varepsilon}}{\dot{\varepsilon}_0}\right)\right]}_{f_2} \cdot \underbrace{\left[1 - \left(\frac{T - T_{room}}{T_{melt} - T_{room}}\right)^m\right]}_{f_3}. \quad (6.1)$$

The effective von Mises stress is the product of components describing strain hardening (f_1) as a function of strain ε , strain rate sensitivity (f_2) as a function of strain rate $\dot{\varepsilon}$, and thermal softening (f_3) as a function of temperature T . The parameters A , B , C , n , m , T_{melt} and the room temperature T_{room} are to be specified. In the previous equation, $\dot{\varepsilon}_0$ represents the reference strain rate. In this work, the material parameters for A2024 T351 are based on the parameters used in [110], as shown in Tab. 6.1. A2024 T351 is chosen as the workpiece material as the Johnson-Cook parameters are well defined in literature [68, 67, 120, 47, 49]. The 2D orthogonal cutting model and the 3D scratch model both employ the Johnson-Cook material model in conjunction with the Johnson-Cook damage model [45] to compute damage evolution. The plastic strain at failure $\bar{\varepsilon}^f$

$$\bar{\varepsilon}^f = \underbrace{\left(H_1 + H_2 \exp\left(H_3 \frac{\sigma_m}{\bar{\sigma}}\right)\right)}_{g_1} \cdot \underbrace{\left(1 + H_4 \ln \frac{\dot{\varepsilon}}{\dot{\varepsilon}_0}\right)}_{g_2} \cdot \underbrace{\left[1 - H_5 \left(\frac{T - T_{room}}{T_{melt} - T_{room}}\right)^m\right]}_{g_3} \quad (6.2)$$

is the product of the relationship between hydrostatic stress and von Mises stress (g_1), the relationship between strain rate and material ductility (g_2), and the effect of thermal softening on material ductility (g_3). In Eq.6.2, H_1 - H_5 are damage parameters. In this work, a simplified Johnson-Cook damage model is used with neglected temperature-dependent effects and with the parameters fitted by [110], see Tab.6.1. The thermal softening effect on the material ductility (H_5) is neglected because it is quite difficult to determine this temperature dependent parameter at high temperatures and high strain rates. Therefore, it is set to zero to simplify the comparison of the different discretization approaches. Furthermore, since the work of Johnson and Holmquist in 1989, in which the properties were measured for 23 different materials, H_5 has always been given as 0, which has also been adopted in [68, 67, 120, 47, 49].

In this study, the damage evolution \dot{D} is determined by the Hillerborg fracture energy model with linear softening [40]. Once the damage is initiated, the damage evolution \dot{D} varies according to

$$\dot{D} = \frac{L\dot{\varepsilon}}{u_f} = \frac{\dot{u}}{u_f}, \quad (6.3)$$

where L is a characteristic length of the finite element and u_f is the plastic displacement at failure, defined as

$$u_f = \frac{2G_f}{\sigma_{y0}} \quad (6.4)$$

TABLE 6.1: Johnson-Cook material parameters, damage coefficients and fracture toughness properties of A2024-T351, taken from [110]

Johnson-Cook material parameters			
Initial yield strength	A	MPa	369
Strain hardening constant	B	MPa	684
Strengthening coefficient of strain rate	C	-	0.0083
Strain hardening coefficient	n	-	0.73
Thermal softening coefficient	m	-	1.7
Johnson-Cook damage parameters			
Initial stress triaxiality dependent parameter	$H1$	-	0.13
Stress triaxiality dependent constant	$H2$	-	0.13
Stress triaxiality dependent coefficient	$H3$	-	1.5
Strain rate dependent parameter	$H4$	-	0.011
Temperature dependent parameter	$H5$	-	0
Fracture toughness – mode I	K_{IC}	MPa \sqrt{m}	37
Fracture toughness – mode II	K_{IIC}	MPa \sqrt{m}	26
Poisson ratio	ν	-	0.3
Young's modulus	E	GPa	73

where σ_{y0} is the value of the field stress when the failure criterion is met and G_f is the fracture energy.

After damage initiation for $D > 0$, the new yield strength value σ and new Young's modulus \tilde{E} can be computed using $\sigma = (1 - D)\tilde{\sigma}$ and $\tilde{E} = (1 - D)E$. The fracture energy G_f , a material parameter that shows the required energy to open a unit area of crack [71], can be determined by

$$G_f = \frac{1 - \nu^2}{E} K_i^2 \quad (6.5)$$

for fracture mode i . In literature there are two types of crack development, an opening mode, and a sliding mode. The fracture energy is determined by the corresponding fracture toughness (K_{IC} and K_{IIC}) [67]. The fracture toughness of A2024 T351 aluminum for these two modes are provided in Tab. 6.1. It is to be noted that the SPH model do employ the Hillerborg fracture energy model as material separation occurs due to the lack of cohesion between the particle-particle connection. Hence, an additional chip separation criterion is not required in these methods.

Fig. 6.2 illustrates the Johnson-Cook material model and the Johnson-Cook damage model of an elasto-plastic behavior with linear elasticity (a-b), strain hardening and thermal softening (b-c), damage initiation at (c), damage evolution (c-d) and eventually fracture (d). The stress-strain response in the absence of a damage model (c-e) is illustrated additionally.

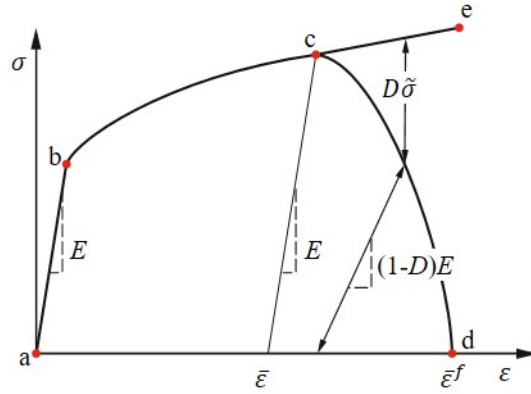


FIGURE 6.2: Uniaxial stress-strain response of an elasto-plastic material as per [67]

6.3.3 Contact model

Orthogonal cutting and scratching involve continual contact between the workpiece and the tool. When both components move in relation to one another, friction develops at the contact interface. The interface between the tool and the workpiece is defined by a penalty-based contact algorithm. Here, the tool is referred to as the master surface and the workpiece as the slave surface. The mesh of the workpiece must be kept fine enough to prevent tool penetration when in contact.

The classic Coulomb friction law is the simplest of the friction models and is applied in the contact model. In the Coulomb friction model, the frictional stress τ_f is related to the passive stress σ_n times a constant coefficient of friction μ

$$\tau_f = \mu\sigma_n. \quad (6.6)$$

Both the 2D orthogonal cutting model and the 3D scratch model employ the Coulomb friction model, where the coefficient of friction is set to $\mu = 0.23$ according to the investigation of [2]. Even though different coefficients of friction can be varied based on the force ratio measured from experiments, a constant value is chosen to facilitate the comparison between the different discretizational models.

6.4 2D Orthogonal Cutting Model

In this section, the simulation framework, benchmark simulation and study on the effect of change of tool rake angle γ are described for the 2D orthogonal cutting model.

6.4.1 Simulation Framework

An orthogonal cutting with a positive rake angle γ is selected to benchmark the 2D models (equivalent to a turning process). The orthogonal cutting model is developed to test various mesh discretizational approaches and validate the workpiece material parameters with experimental values [110]. A positive rake angle tool is initially chosen as a baseline to benchmark the model and test selected material parameters, after validation negative tool rake angles are modelled, that represent a grinding process. The model's parameters, which are presented in Table 6.2,

were transferred from [110]. These turning experiments [110] also serve to validate the outcomes of the simulation.

TABLE 6.2: Parameters of the 2D orthogonal cutting models with A2024 T351 aluminum, as per [110]

Parameters of workpiece (A2024 T351 aluminum)		
Young's Modulus E_{wp}	GPa	73
Poisson ratio ν_{wp}	-	0.3
density ρ_{wp}	kg/m ³	2780
Parameters of tool (high speed steel (HSS))		
Young's Modulus E_{tool}	GPa	210
Poisson ratio ν_{tool}	-	0.33
density ρ_{tool}	kg/m ³	7830
orthogonal rake angle γ	degree	20
clearance angle α	degree	5
cutting edge radius r	μm	4
feed per revolution f	μm	50
depth of cut a_p	μm	1
cutting speed v_c	m/min	180

The LAG, ALE and SPH consist of a tool (meshed body) and a workpiece (FEM / SPH elements). The tool is given an imposed motion with constant cutting velocity v_c in negative x -direction and the workpiece is fixed along its left and bottom nodes. The tool is positioned with a feed $f = 50 \mu\text{m}$ along the y -axis and a depth of cut $a_p = 1 \mu\text{m}$ along the z -axis. Earlier studies and selections of element sizes for the simulation models were made using suggestions from [13, 67, 68, 110] to lessen the effect of the size and spacing of the elements or of the particles on the computed reaction forces. The element discretization d_e for LAG and ALE models and the particle discretization d_p for the SPH model is set to $d_e = d_p = 3 \mu\text{m}$. The workpiece are separated into three layers in the LAG and ALE simulations: L1, L2, and L3 as shown in Fig. 6.3a. To distinguish the chip region (L1) from the components of the workpiece, the region L2 comprises of a thin line of sacrificial elements (L3). The Hillerborg fracture energy model with linear softening states that an element in the sacrificial layer (L2) fails when it reaches the preset critical damage value [40]. When the critical damage value is reached, element deletion is activated, and the element is removed to prevent mesh distortion. Based on the opening and sliding fracture modes, the failure criterion is computed. The failure criterion for regions L1 is calculated based on K_{IIC} and for L2 elements is calculated based on K_{IC} (see Eq. 6.5). For the study's mesh-based models, these values have been maintained constant. The chip region L1 in the ALE model is designated as the ALE domain with adaptive re-meshing, in contrast to the LAG model. In order to lessen element distortion, a new, smoother mesh is constructed in each adaptive mesh increment, and the nodes in the domain are moved [71]. The intensity of the adaptive meshing increases with the number of mesh sweeps for each increment. In this investigation, there were five mesh sweeps. The quality of the mesh and the effectiveness of the calculation are both impacted by the amount of adaptive meshing increments. This number is set to 50000 because mesh quality must be of the utmost importance to accomplish steady state cutting conditions [13, 71]. In case of the LAG model, the chip region L1 is simply modeled with

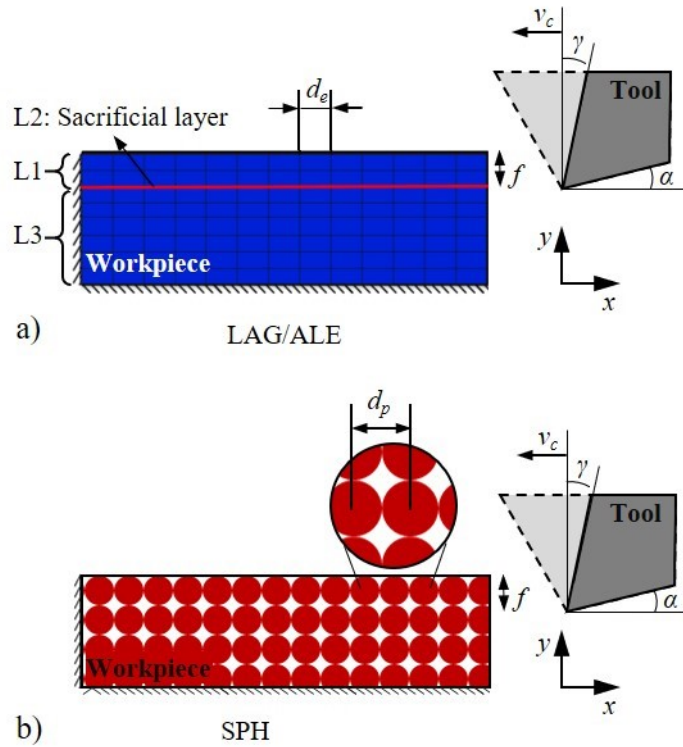


FIGURE 6.3: 2D Simulation framework of the LAG/ALE models a) and SPH models b) [107]

Lagrangian elements without activating element deletion. No sacrificial layer is designated in the case of the particle-based techniques SPH since the chip and workpiece separate because of the weak particle-particle interactions.

6.4.2 Benchmark simulation

Benchmark simulations are used to validate the considered discretization approaches LAG, ALE and SPH. The results are compared to the dry-turning process on aluminum alloy (A2024 T351) from [110]. The process forces calculated from the simulation and the forces measured from [110] are illustrated in Fig.6.4. In the steady state of the experiment, the measured average cutting force in x -direction is 50 N. The LAG, ALE and SPH methods predict the cutting force with a minor error of 1 %. It is interesting to note that for all discretization techniques, the passive force drastically understates and disagrees with experimental findings. The high error for this computation is 40 %. This inaccuracy can be attributable to the removal of elements during material separation for mesh-based approaches. When a threshold value is achieved, the distorted parts are removed, which results in less contact between the tool and the workpiece and a reduction in passive forces. The meshless methods use a weighted function rather than a mesh to calculate the cohesive relationships between the particles. The cohesive forces between the particles drop in a bell-shaped pattern inside a region of effect, which may cause the particles to separate too soon. In addition to material separation parameters, choosing a friction coefficient and friction model could aid in lowering the error in the estimation of the passive forces [13, 82, 1]. All discretization methods, however, produce comparable findings for the cutting and passive

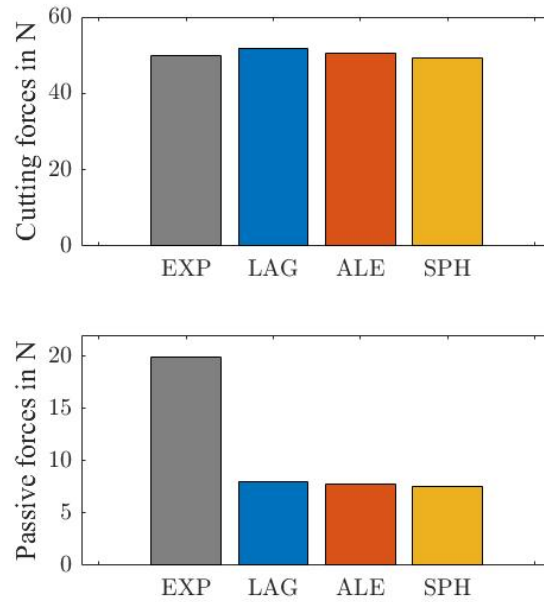


FIGURE 6.4: Comparison of the cutting/passive forces of the discretizational approaches with the experimental results from [110] for the 2D orthogonal cutting model $\gamma = 20^\circ$

forces and are accordingly regarded as equivalent modeling possibilities that require additional investigation.

6.4.3 Effect of negative tool rake angle

To determine whether the three proposed orthogonal 2D cutting models are capable of simulating scratching with a high negative rake angle, similar to the contact circumstances that occur during grinding, the rake angle is changed from $\gamma = 20^\circ$ (orthogonal cutting) to $\gamma = -60^\circ$ (grinding) and compared to the process forces. At the same time an evaluation is also made, whether a two-dimensional description is sufficient for scratching with negative rake angle. The investigated rake angles in the range $20^\circ > \gamma > -60^\circ$ are typical in grinding. For stability reasons of the LAG and ALE simulations the threshold value of the failure model had to be decreased for $\gamma \geq -52.5^\circ$, which explains why the cutting forces do not increase further for these angles, cf. Fig. 6.5. It is clear from comparing the findings of all discretization techniques for all rake angles Fig. 6.5, that cutting forces and passive forces both rise as the absolute value of the angle rises. Because increasing negative rake angles provide greater compressive stresses on the workpiece, this tendency can be attributed to the increased tool-workpiece interaction. In an experimental research conducted by, a similar trend to increase process forces is discovered [99, 35, 7]. Particle-based methods and mesh-based methods perform identically in each scenario, according to a comparison of discretization methodologies, although the forces calculated by the particle-based methods are noticeably higher. The primary cause of this might be the failure model present in mesh-based approaches, for which the threshold values must be manually specified.

The verification of the process forces with scratch experiments performed at our laboratory with rake angles of $\gamma = -52.5^\circ$ and $\gamma = -60^\circ$ and various speeds (cf. Fig. 6.6) shows that all

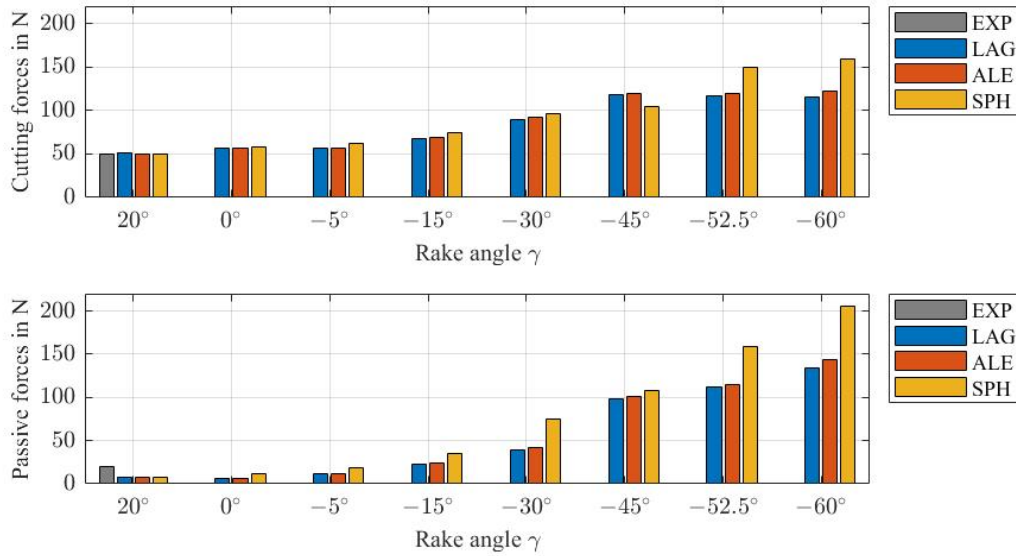


FIGURE 6.5: Cutting forces a) and passive forces b) of orthogonal cutting with discretization approaches LAG, ALE and SPH for tool rake angles $20^\circ > \gamma > -60^\circ$. Experimental obtained values from literature [110]

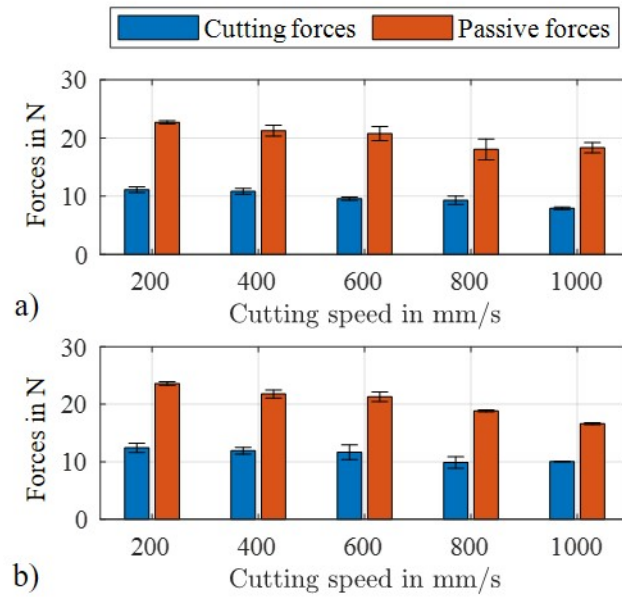


FIGURE 6.6: Measured process forces during single grit scratching with cutting speeds $200 \text{ mm/s} < V_c < 1000 \text{ mm/s}$ and depth of cut $a_p = 50 \mu\text{m}$ with a) conical indenter of cone angle 105° ($\gamma = -52.5^\circ$) b) conical indenter of cone angle 120° ($\gamma = -60^\circ$)

2D orthogonal cutting models significantly overestimate the process forces. It is evident from witnessing a real single scratch experiment that several interaction mechanisms are dominant and have an impact on the process forces. In contrast to the 2D cutting paradigm, where a single

surface interacts with the workpiece, the interaction between the cutting tool and the workpiece occurs in all directions. The force components are altered by spatial interaction with plowing and lateral material flow, which are not depicted in the 2D model. Cutting must therefore be described in 3D if not only trends but also absolute force levels are to be evaluated. Consequently, a 3D model for single grit scratching is detailed in the following part, and the outcomes of the LAG, ALE, and SPH techniques are contrasted. The objective is to determine whether the disparities between the 2D model and the trials are caused by the fact that the problem cannot be reduced to 2D or by the need for better material or friction models.

6.5 3D single grit scratch model

To examine the material flow principles and compare geometrically more complicated models with experimental research on the grit geometry and speed of cut, a 3D single grit scratch model is developed. The models are validated using a benchmark simulation, and to assess the models' performance regarding expected forces, a sensitivity analysis on the indenter cone angle and the cutting speeds is performed. An appropriate discretization to describe a scratch process is selected based on the results. The analysis is further extended to validate the scratch topography from experiments.

6.5.1 Simulation framework of 3D scratch model

The 3D scratch model is also developed in Abaqus/Explicit 2019 for the discretization techniques LAG, ALE, and SPH. In contrast to the 2D model, the tool is now modeled as a rigid cone with a $35\ \mu\text{m}$ tool tip radius and cone angles of 105° and 120° , respectively, which were estimated from microscopic photographs as shown in Fig.6.7.

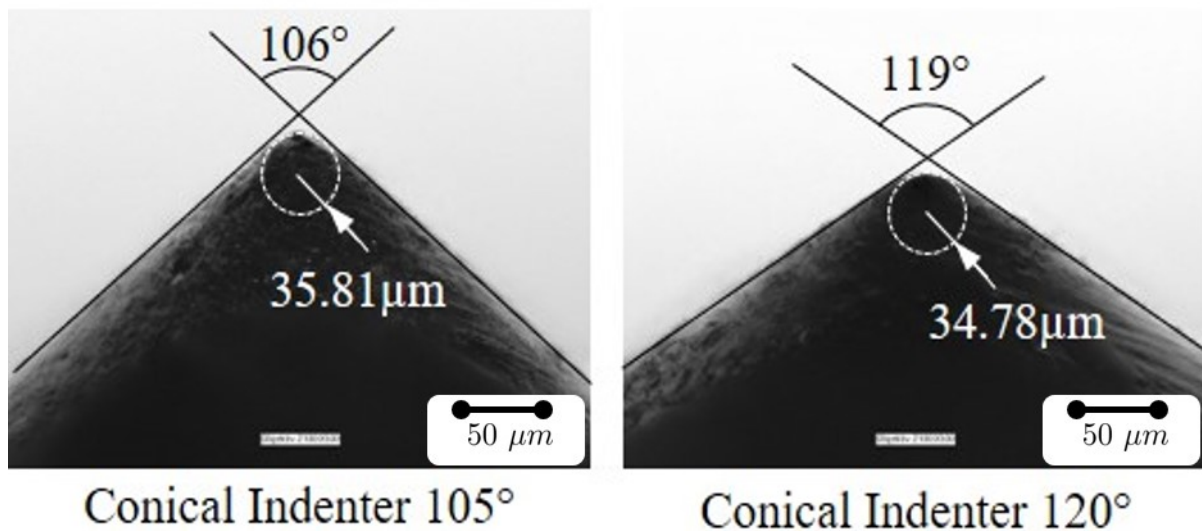


FIGURE 6.7: Microscope images of diamond indenters with cone angle and filleting [107]

To speed up computation, the conical tool is represented as a rigid body and is meshed as coarsely as possible with an element size of approximately $10\ \mu\text{m}$ at the apex. It is appropriate

to simplify the model because the experimental tool, a diamond indenter, is substantially harder than the aluminum workpiece (A2024 T351).

The tool's nodes, to which the velocity boundary conditions were applied, are connected by a stiff point.

The cuboid workpiece is represented as a deformable body using the same A2024 T351 aluminum material parameters as in the 2D model, as shown in Table 6.2. The dimensions of the workpiece are shown in Fig. 6.8 as 1 mm \times 0.5 mm \times 0.2 mm. In contrast to the 2D model, the LAG and ALE models do not contain a sacrificial layer. The Johnson-Cook material and damage model is applied to all workpiece elements, as detailed in section 6.3.2, and the energy based failure criterion (derived based on K_{IIC}) as well. The SPH methods do not use a failure criterion because the removal of material is dependent on the lack of cohesiveness between the particles.

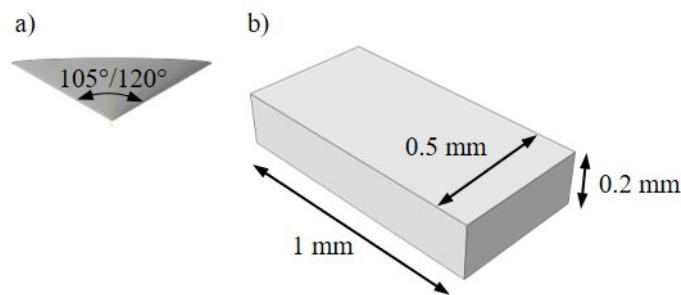


FIGURE 6.8: Model dimensions of rigid tool a) and deformable workpiece b) of the 3D scratch model [107]

The discretized workpiece is shown in Fig.6.9 with element spacing d_e for the LAG/ALE models and particle spacing d_p for the SPH model that is comparable to the 2D model with $d_e = d_p = 3 \mu\text{m}$. The element size is small enough to capture how the workpiece's topography changes throughout simulation.

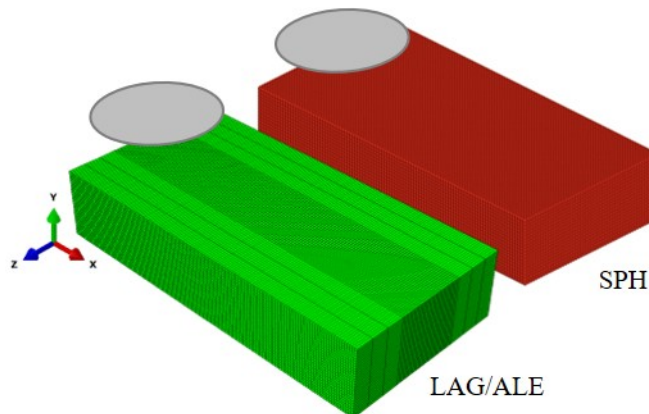


FIGURE 6.9: Discretized workpiece with element spacing d_e in the center part for the LAG/ALE models and particle spacing d_p for the SPH model [107]

6.5.2 Model adaptation based on experimental findings

According to experimental protocol as explained in 4.2.5, the workpiece is positioned for the scratch test using a vertical z -axis table. By modifying the z -axis table, a zero location is first established, and the required cutting depth is then set. To ensure that the necessary depth of cut is correctly attained, a distance measuring laser is used. The linear device is relocated to its reference point after the cutting depth has been determined. The linear device is initially accelerated to the final cutting speed with the indenter in its fixed position, then moves at a constant speed during scratching, and is eventually decelerated again. The single-grit scratch experiments are repeated five times, and force measurements are taken for each parameter combination (cutting speed and depth of cut). After the testing, the workpiece's surface was scanned to compare the topography with the simulations. Due to elastic deformation of the test setup, it was discovered that the observed groove depth was lower than the previously set depth of cut. After considerable investigation, it is discovered that the deviation is caused by the combined effect of the elastic deformation (an integral part of chip formation) at t . Consequently, the simulations were performed with a reduced depth of cut with $a_{p,sim} = 35 \mu\text{m}$, which corresponds to the predefined depth of cut $a_{p,exp} = 50 \mu\text{m}$ during experiments. In the following section, the 3D scratch models with LAG, ALE, and SPH discretization procedures are validated and analyzed using the findings from these experimental investigations.

6.5.3 Benchmark simulation

The three discretization methods (LAG, ALE, and SPH) were used to perform 3D simulations of a single grit scratch. Fig. 6.10 depicts a typical stress distribution from the ALE and SPH simulations. The LAG model and the ALE model have comparable scratch profiles. The von Mises stresses are higher for elements along the scratch's path and more evenly distributed for the ALE model than for the SPH model. When compared to the SPH model, the ALE model better describes the scratch topography and provides a clear distinction of the groove and pile-up zones.

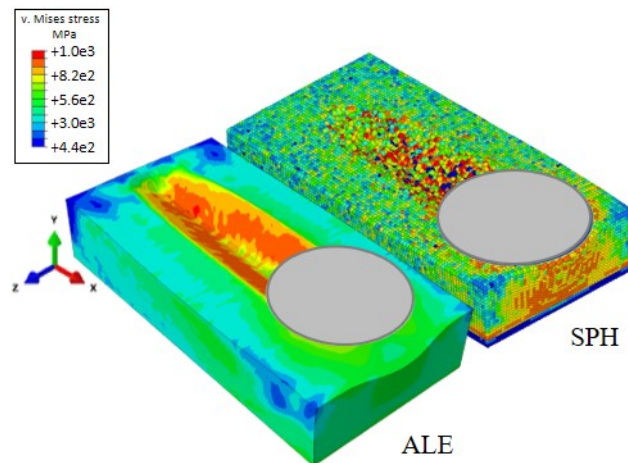


FIGURE 6.10: Distribution of the von Mises stress in the ALE and SPH model [107]

Comparing the experimental measurement of the process forces to the three discretizational approaches for a cutting speed of 200 mm/s, a depth of cut of $a_{p,exp} = 50 \mu\text{m}$ (corresponding to $a_{p,sim} = 35 \mu\text{m}$), and an indenter with a cone angle of 105° is shown in Fig. 6.11. At steady

state, the average cutting force recorded in the x -direction is 12.12 ± 0.8 N. The cutting force is overestimated by the ALE model with 13.57 N, while it is underestimated by the LAG and SPH models with 10.92 N and 5.09 N, respectively.

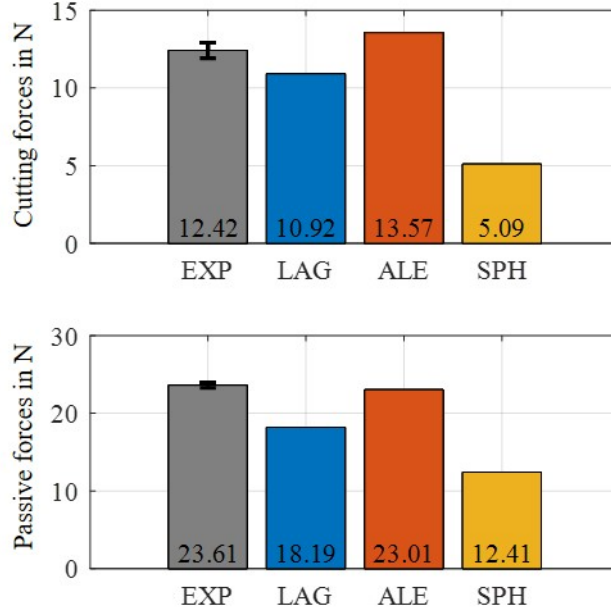


FIGURE 6.11: Process forces of measurement and discretization approaches for a 3D single grit scratch (cutting speed $v_c=200$ mm/s, depth of cut $a_{p,exp}=50$ μm that corresponding to $a_{p,sim}=30$ μm , cone angle of 105°) [107]

In a similar manner, the ALE model outperforms other discretization techniques in its ability to forecast passive forces. At steady state, the average passive forces recorded along the y -direction are 22.68 ± 0.28 N, which the ALE model can accurately duplicate with a value of 23N. With 18.19 N (LAG) and 12.41 N (SPH), the other approaches once again underestimate the passive forces.

When comparing the LAG and ALE techniques, both models have their built-in element deletion mechanisms turned on. The LAG model's components do not, however, use a smoothing technique, whereas the ALE approach does by default. As a result, the LAG model's elements are removed too soon, which lowers the process forces. The SPH model, in contrast, underestimates the process forces despite not using any failure theory or element deletion techniques.

The cohesion model used to connect the particles may be the cause for the inaccuracy. The size effect (low depth of cuts), which is evident in a micro-cutting process like scratching ([97, 113]), is not taken into account by the SPH model. The material model may need to be expanded further, and using a complicated contact model can assist to solve the issue.

It may infer from the benchmark analysis that the ALE approach is the most effective at simulating a scratch and the forces that cause it. In the following part, demonstrates how well the three discretization techniques can map trends and dependencies on cutting speed and tool geometries.

6.5.4 Sensitivity analysis of discretizational approaches

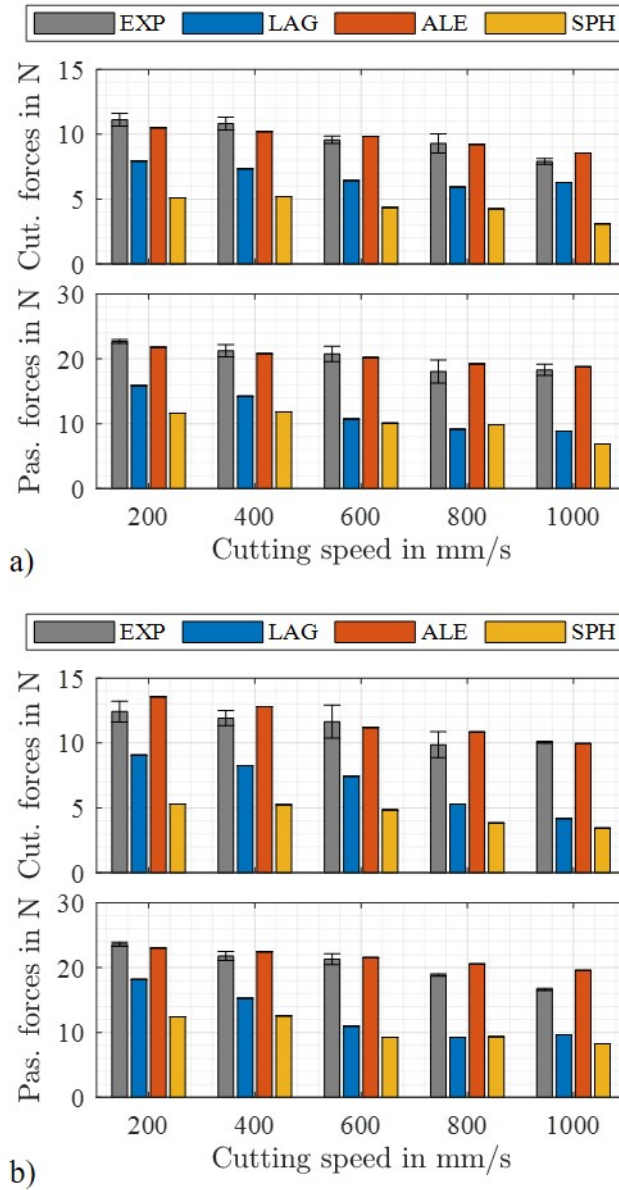


FIGURE 6.12: Process forces of measurement and discretization approaches for a 3D single grit scratch for a depth of cut $a_p=50\ \mu\text{m}$ that corresponding to $a_{p,\text{sim}}=30\ \mu\text{m}$ with a cone angle of 105° (a) and with a cone angle of 120° (b) [107]

In this section, parameter analyses are carried out to compare the discretization methods' capacity to capture observed trends in forces and topographic changes in the workpiece. The process forces are examined for two indent geometries (cone angle= 105° and 120°) and five different cutting speeds ($v_c= 200\text{-}1000\ \text{mm/s}$). A reduced depth of cut $a_{p,\text{sim}}= 35\ \mu\text{m}$ was used in the simulation to represent the groove depth when scratching with a depth of cut $a_{p,\text{exp}}= 50\ \mu\text{m}$ during experiments. Additionally, for both indent geometries the resultant workpiece topography are compared to measurements. Additionally, measurements are made

of the resulting workpiece topography for both indent geometries. The averaged process forces from simulations and observations are contrasted in Fig. 6.12. It is clear that the ALE method optimally captures the process forces. The trend for process forces to decrease with increasing cutting speed is appropriately predicted by all models. Compared to rubbing and plowing, cutting predominates at high speeds, which results in lower process forces. Additionally, thermal softening is more significant than strain hardening when scratching at high cutting speeds, which results in an additional reduction in process forces. Further evidence of this propensity comes from experimental examinations of [84]. Comparison of the results for the two cone angles (105° and 120°) shows that the process forces increase with larger angle, compare Fig. 6.12a) and b). As previously described in [99, 35, 82], this effect is particularly noticeable at low cutting speeds of 200 mm/s and can be explained by a longer contact length between the tool and workpiece, which results in higher compressive stresses. This trend is shared by all three discretization techniques, albeit the ALE model comes closest to the experimentally measured process forces. The Johnson-Cook model's strain rate sensitivity and thermal softening parameters should be optimized to further enhance the outcomes. Nevertheless, by comparing the process forces between the discretization approaches and the experiments, it can be concluded that the ALE approach is the most accurate with an average error of 5.4 % for cutting forces and 5.2 % for passives forces, for the other numerical methods the errors are greater than 30 %.

In the further section, extensive testing of the ALE model by varying the tool geometries and varying machine parameters is performed. The simulations will be verified with scratch experiments performed at the laboratory. The model will also be further developed to describe a multiple grit scratch test which will be verified with experiments. This will take us one more step closer towards understanding complex material removal mechanisms that happen during a grinding process.

6.6 Parameter study of 3D single scratch ALE model based on process forces and scratch topography

The 3D scratch model is tested by varying the tool geometries, similar to the experiments performed with conical and pyramidal indenter with tool apex angles 105° , 120° and 135° as shown in Fig. 6.13. The flat workpiece is defined as a deformable body with dimensions $1\text{ mm} \times 1\text{ mm} \times 0.1\text{ mm}$ as shown in Fig.6.14. The model dimensions are optimized compared to the previous simulation model Fig. 6.8 in order to reduce the computational time. However, some benchmark simulative tests were performed with the optimized model to ensure its validity by comparing the results with the previously built models. Fig. 6.15 and Fig. 6.16 shows the FEM single grit scratch model using the conical and pyramidal indenter geometries. It can be observed that the workpiece mesh is partitioned into two regions, a coarse region, and a fine region. The fine region is meshed with an element size of $d_e = 3\text{ }\mu\text{m}$ and the coarse region with an element size of $d_e = 40\text{ }\mu\text{m}$. This is done to reduce the computational time of the explicit finite element simulation. In the following section, 3D conical and pyramidal scratch simulations are performed by varying the depth of cut like the scratch experiments performed at the laboratory. The simulations are validated based on the process forces and surface topography. Practical conclusions are drawn based on the various single grit scratch simulations performed.

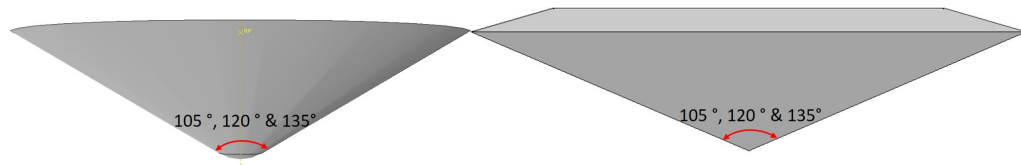


FIGURE 6.13: Tool dimensions of ALE conical and pyramidal 3D scratch models

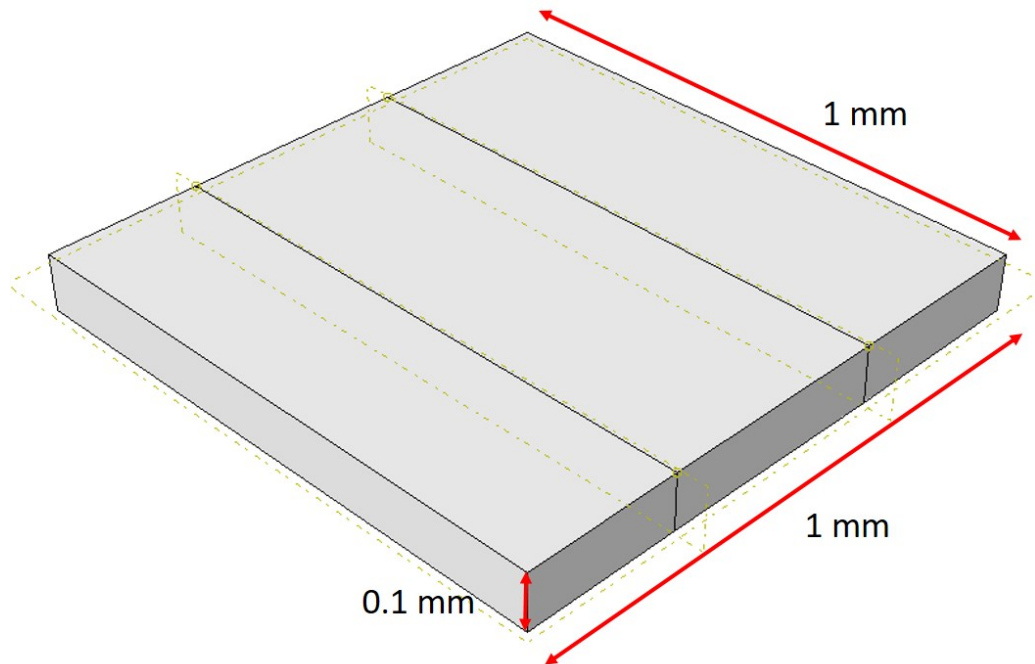


FIGURE 6.14: Workpiece dimensions of ALE conical and pyramidal 3D scratch models

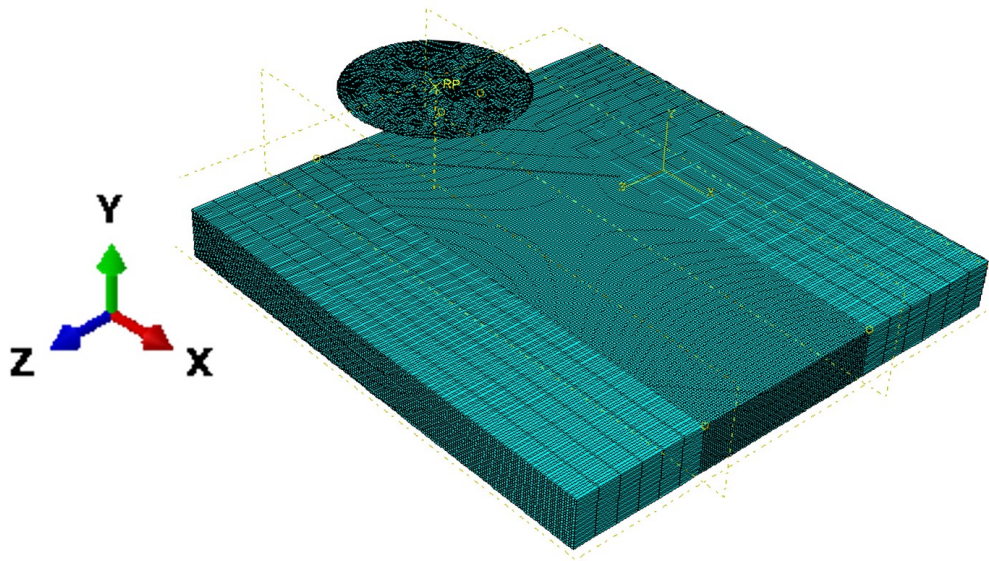


FIGURE 6.15: Simulation framework of ALE conical 3D scratch model

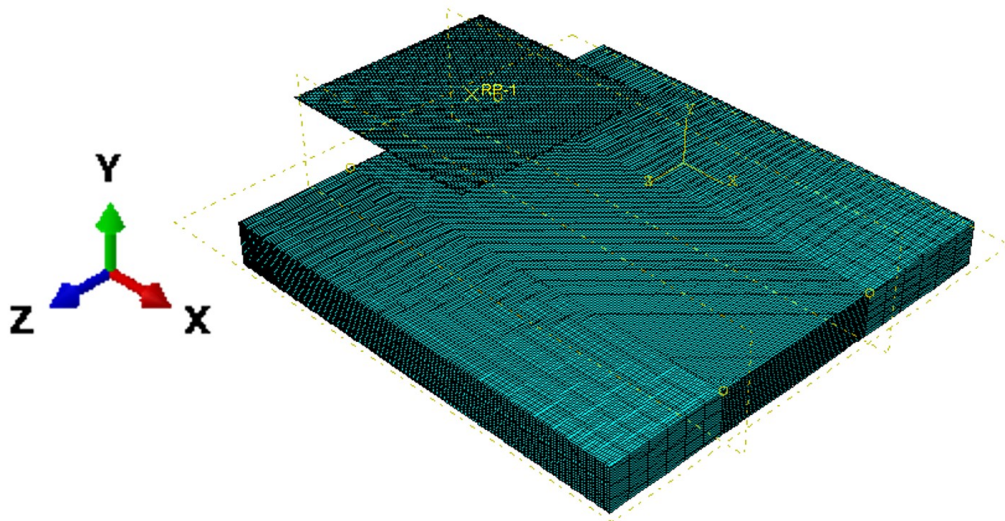


FIGURE 6.16: Simulation framework of ALE pyramidal 3D scratch model

This section is divided into two subsections, the first part presents the results of the 3D single scratch simulations performed using conical indenters, followed by the simulations performed using pyramidal indenters.

6.6.1 Results: 3D conical single scratch model

The single scratch simulations were performed with conical indenters with tool apex angles of 105° (C-105), 120° (C-120) and 135° (C-135). The depth of cut is varied from $15\ \mu\text{m}$ to $35\ \mu\text{m}$ at a constant cutting speed of $200\ \text{mm/s}$.

Fig. 6.17 shows the displacement contour plots of the simulation models in the negative y direction. It can be observed that, with the increase in the tool apex angle, the scratch width appears to be wider.

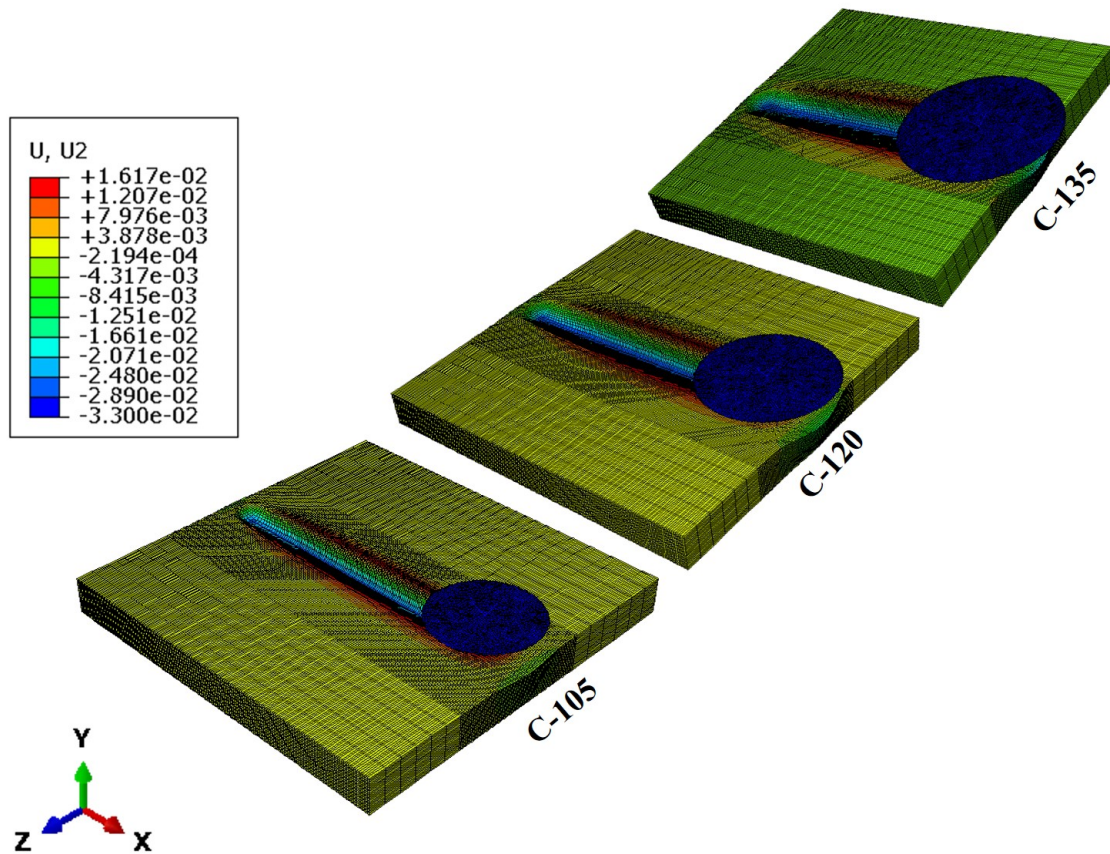


FIGURE 6.17: Displacement contour: conical indenters with tool apex angles of 105° (C-105), 120° (C-105) and 135° (C-105).

Fig. 6.18 shows the 2D cross section of a scratch obtained from the various simulations performed with conical indent geometries. It is observed that the simulated groove resembles well with the experimental groove measured, although there are some deviations observed. It can also be observed that the simulations capture the effect of a wider groove produced while performing a scratch with a wider indent geometry, similar to what is observed during the experiments. The simulations also predict that the pile-up ratio reduces with increase in tool apex angle. With increase in tool angle, a wider tool geometry induces more compressive forces onto the workpiece, which produces a larger groove and smaller pile-up areas. Although the simulated 2D scratch topographies have a good resemblance with the experimental scratch topographies, it can be observed that there are some deviations from experimental results. The deviations can be specially observed in the pile-up areas. This can be attributed to multiple reasons. In the scratch experiment, there is change in the contact conditions of tool and workpiece, due to workpiece asperities. However, this is not replicated in the simulations performed, where the workpiece is

a perfectly flat surface. In the simulation the aspect of tool wear is not considered, due to which the dynamic changes of tool-workpiece contact are not accurately reproduced. The adoption of more robust contact models and inclusion tool wear can definitely help reduce the deviation from experimental results.

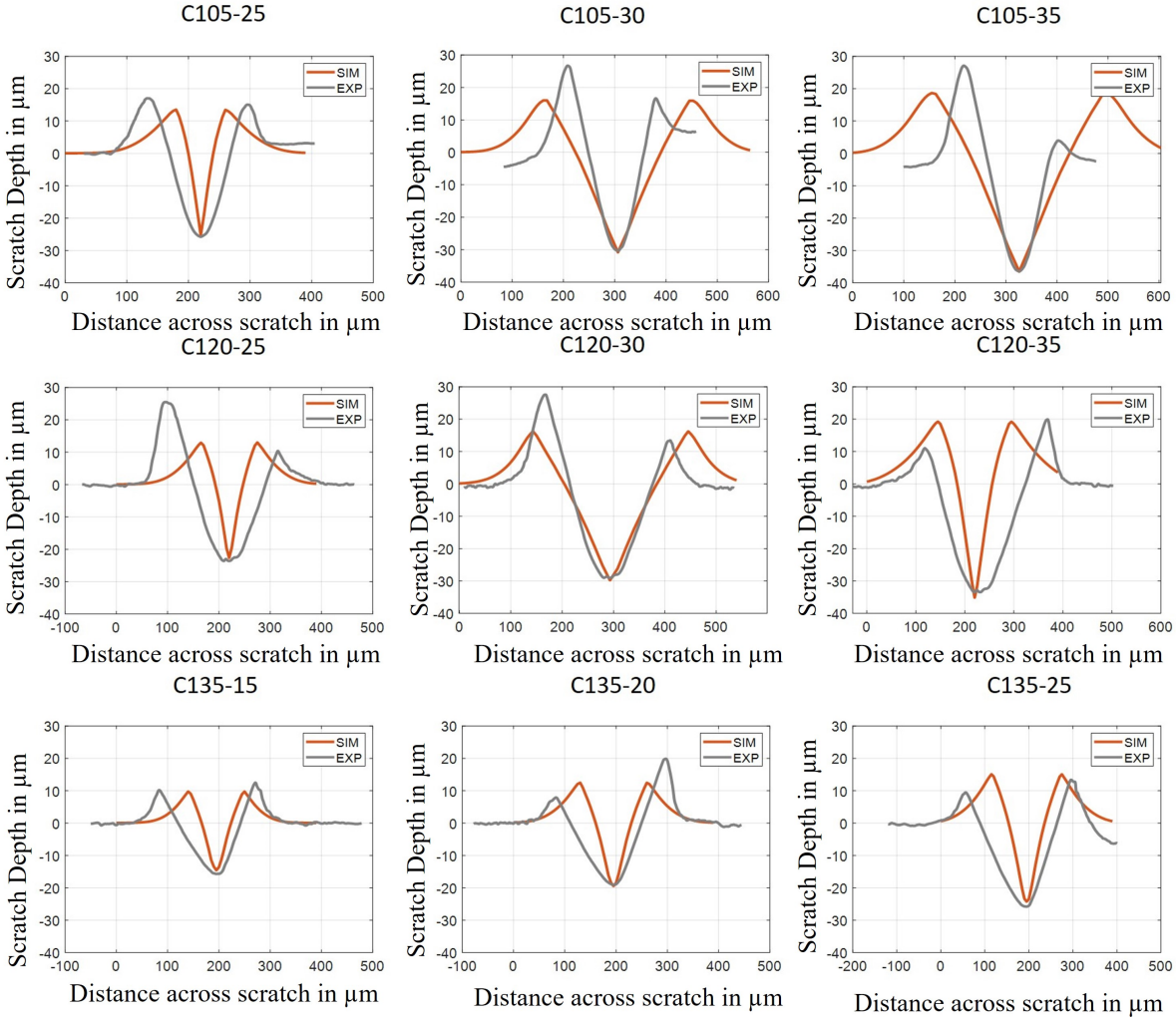


FIGURE 6.18: Experimental vs simulation results of 2D cross scratch topography for various conical tool geometries and depths of cut (with the individual sub figures named as C (conical) followed by the apex angle (in $^{\circ}$) followed by the undeformed chip thickness (a_p in μm), for example C105-25 denotes a conical indenter 105° measured with $a_p = 25 \mu\text{m}$)

The simulation results are verified with the experimental results based on the process forces and the undeformed chip thickness (a_p) measured.

Fig. 6.19 compares the process forces calculated with simulations performed against the experimental measurements. The results are in good agreement with the experimental measurements. It can be observed that the simulation is also able to build the tendencies observed in the experiments, while varying the depth of cut or the tool apex angle.

The passive forces are observed to be higher than the cutting forces measured. This is generally observed while performing material removal with tools with high rake angles. It can be

also observed that the process forces increase with the increase in the tool apex angle. This can be attributed that the wider tool angle exerts a larger force onto the workpiece. The simulation results show that the process forces are highly dependent on the tool geometry. It can be observed in Fig. 6.19 that the conical indenter 135° at $a_p = 20 \mu\text{m}$, measures a much higher process force in comparison to conical indenters 105° and 120° (refer Fig.6.19). This captures the size effect in single grit scratching with an increase in rake angle, the force required to remove material increases with decrease in undeformed chip thickness (a_p). The simulations also predict the tendency of increase in the process forces with increase in the depth of cut, as higher process forces are required to remove more material.

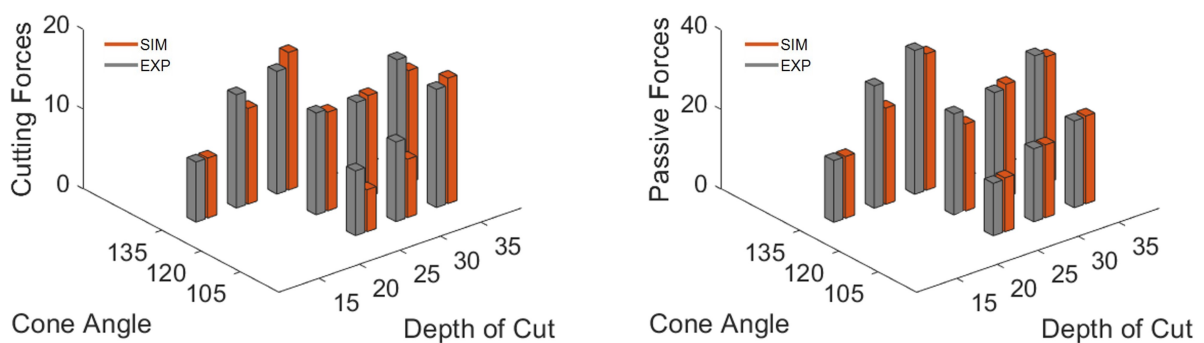


FIGURE 6.19: Experimental vs simulation results of the process forces for conical indenters

6.6.2 Results: 3D pyramidal single scratch model

Under this section, the results from single scratch simulations performed using pyramidal indenters are presented. Similar to the conical single grit simulations, the sensitivity of the simulations was tested by varying the depth of cut and the tool apex angle (105° , 120° and 135°). The depth of cut is varied from $25 \mu\text{m}$ to $40 \mu\text{m}$ at a constant cutting speed of 200mm/s . The Fig.6.20 shows the contour plot of the simulation performed with pyramidal indenters with tool apex angles 105° (P-105), 120° (P-120) and 135° (P-135). Like the conical single grit simulation, it is also observed that the wider tool indenter produces a larger groove in comparison to the narrower tool indenter.

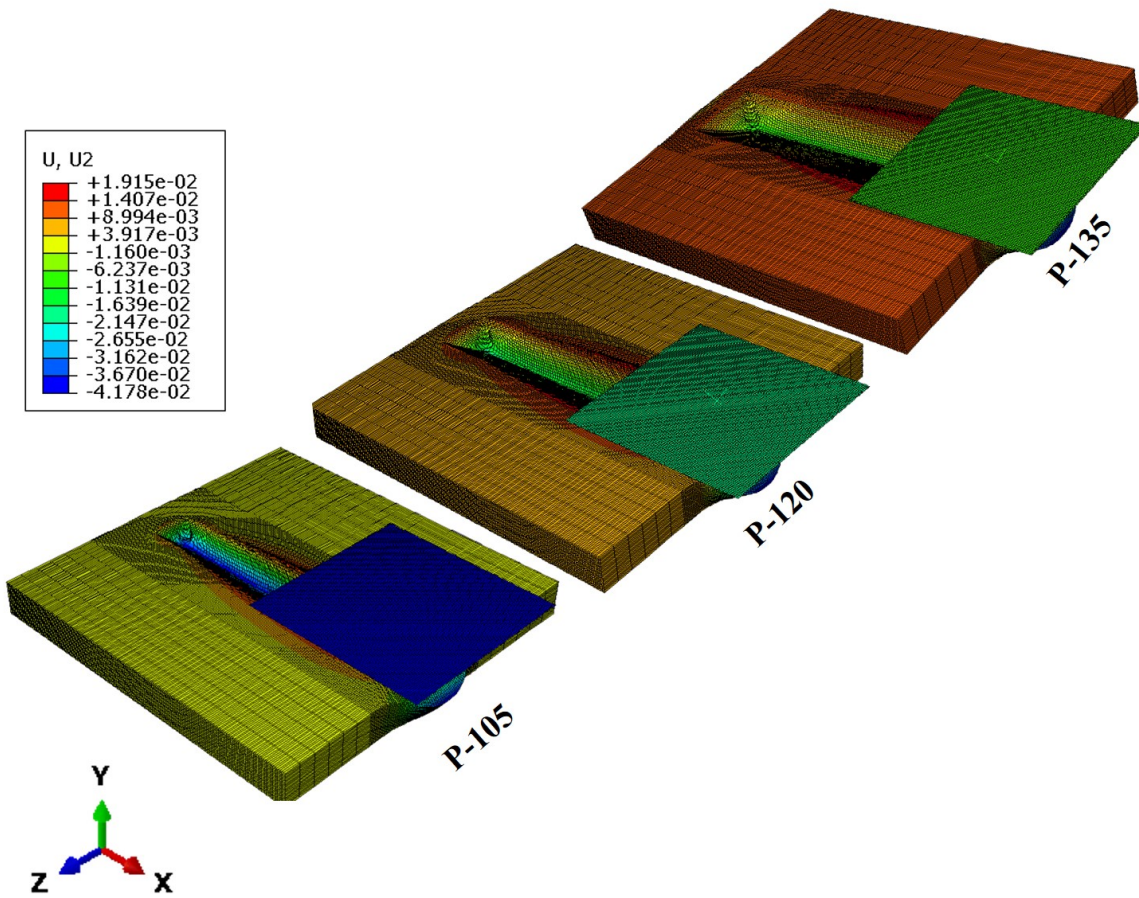


FIGURE 6.20: Displacement contour: pyramidal indenters with tool apex angles of 105° (P-105), 120° (P-120) and 135° (P-135).

Fig. 6.21 shows the 2D cross sectional scratch profile obtained from the various simulations performed. It is observed that the simulated grooves are identical to experimental measurements. The groove area as well as the pile-up areas are predicted quite well by the simulation models. The simulation model shows that the material removal increases with increase in depth of cut. Although it can be observed that there are deviations in 2D simulated scratch profiles from experimental results. It can be specifically observed that the pile-up areas are over-predicted by simulations. It can be because the simulation models are unable to capture the dynamic tool-workpiece contact that occurs during scratching. This can also be, due to strain-hardening effects that make the pile-ups more brittle, an effect that is not quite well captured in the simulation, leading to over prediction of the pile-up areas. This reason is comparable to the one provided for conical indenters. A more robust tool-workpiece contact model, optimisation of material parameters and consideration of tool wear can help improve the results.

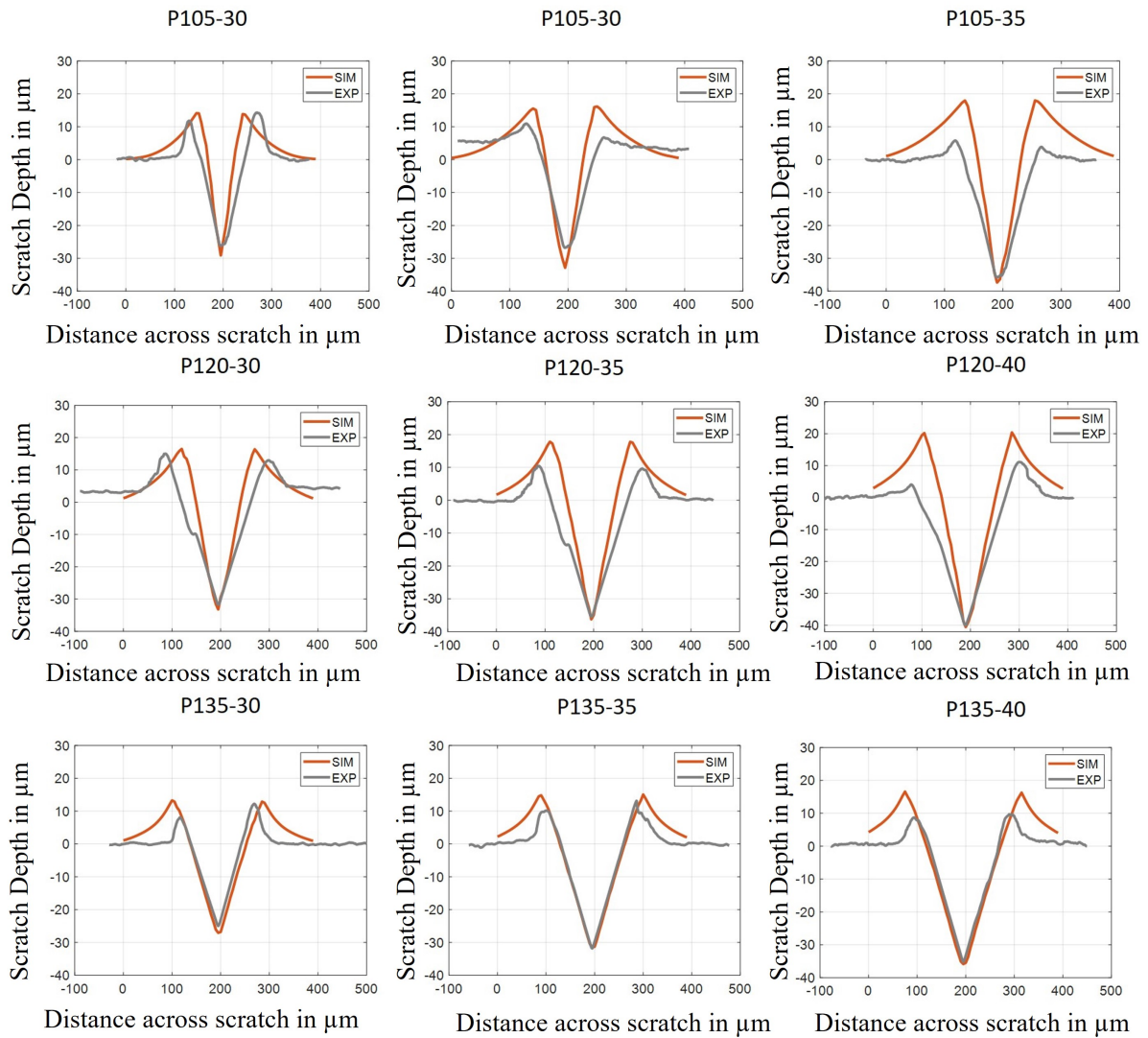


FIGURE 6.21: Experimental vs simulation results of 2D cross scratch topography for various pyramidal tool geometries and depths of cut with the individual sub figures named as P (pyramidal) followed by the apex angle (in $^{\circ}$) followed by the undeformed chip thickness (a_p in μm), for example P105-25 denotes a pyramidal 105° indenter measured with $a_p = 25 \mu\text{m}$

The simulation results are verified with the experimental results based on the process forces and the undeformed chip thickness (a_p) measured.

Fig. 6.22 compares the process forces calculated from the simulation with the experimental measurements. The modeling results and the experimental data agree rather well. The simulations can successfully develop the tendencies that are seen in the tests. It has been noted that when depth of cut increases, process forces also increase. Due to the increased compressive pressures placed on the workpiece while scratching with a wider tool indent, the process forces also increase. The simulation also predicts the process forces calculated with the pyramidal indenters, is lower in comparison to the conical indenters (refer Fig. 6.19). This indicates that the pyramidal indenters produce a more prominent cutting action in comparison to the conical indenters. Thereby producing a larger groove area while measuring lower process forces.

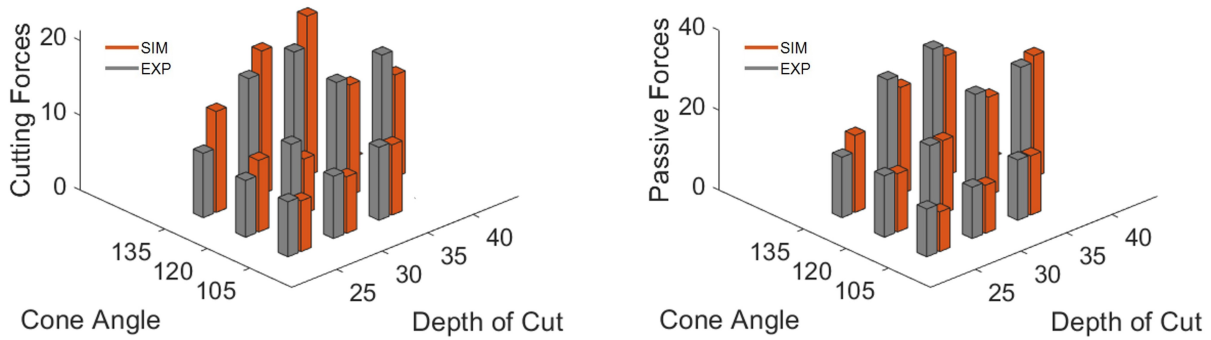


FIGURE 6.22: Experimental vs simulation results of the process forces for pyramidal indenters

6.7 Parameter study of 3D multiple scratch ALE model based on process forces and scratch topography

The multi-pass simulation was performed by shifting the grit in the traverse direction (or $-z$ direction in Figure 6.23). Similar to the multiple pass experiments performed at the laboratory, the separation distance between the indenters were set to 0.2 mm as shown in Fig. 6.23.

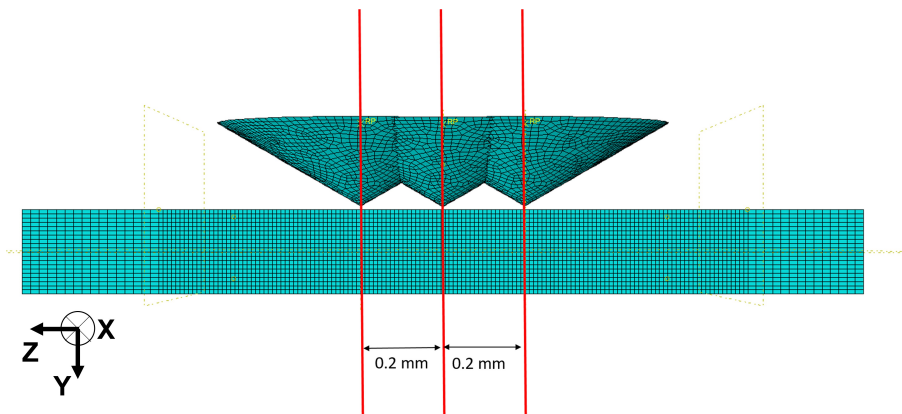


FIGURE 6.23: Separation distance between the conical indenters

Similar to the conical model the pyramidal grit are also shifted in the traverse direction ($-z$ direction) with a separation distance of 0.2 mm as shown in Fig.6.24.

Both the conical and pyramidal multiple pass models are tested at a constant depth of cut ($30\ \mu\text{m}$) and at a constant linear speed ($200\ \text{mm/s}$). The simulations are performed in a similar way the MPST experiments are performed as described in section 4.3.

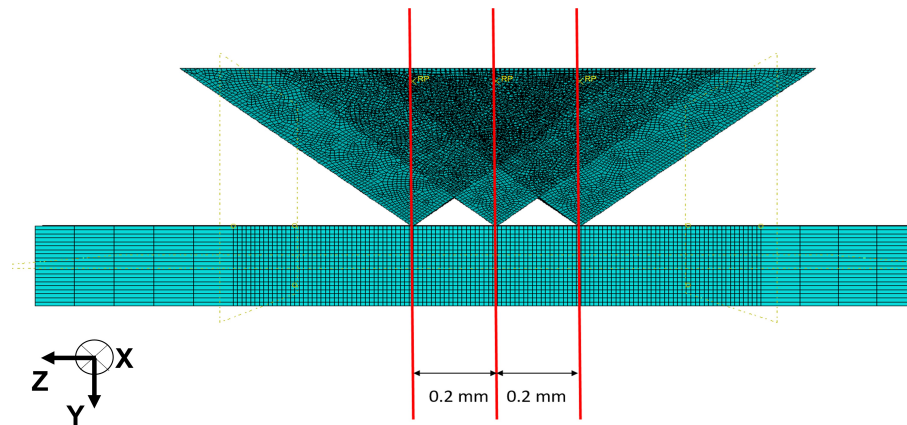


FIGURE 6.24: Separation distance between the pyramidal indenters

In the following sections, the multiple pass scratch simulations performed with the 3D ALE model are presented for conical and pyramidal geometries. The simulations are performed by varying the tool geometry (conical and pyramidal geometry). The 3D model is validated with the scratch experiments performed at the laboratory, based on the process forces (passive forces and cutting forces) measured and the undeformed chip thickness (a_p) measured.

6.7.1 Results: 3D conical multiple pass scratch model

In this section, the results from multiple pass scratch simulations performed using conical indenters are presented.

Fig. 6.25 shows the displacement contour plot in the negative y direction. The interaction between the individual scratches leads to overlap of the pile-up regions, which is quite distinctly observed from the contour plot.

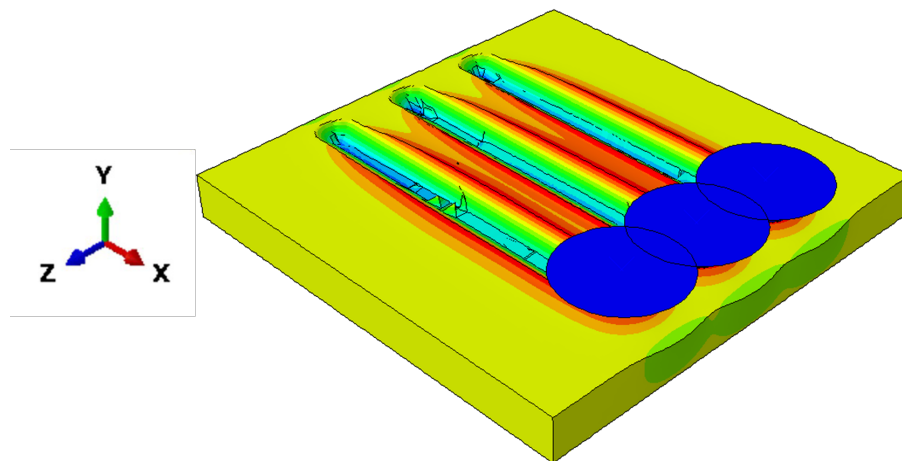


FIGURE 6.25: Displacement contour: Multiple pass simulation using a conical indenter

Fig.6.26 shows the 2D scratch profile of the multiple pass scratch simulation performed with the 105° and 120° conical indenters. On comparing the 2D topography with experiments, the simulation groove resembles the experimental groove. There is good agreement of the

groove depth and groove areas between experiment and simulation. However, there are some discrepancies between the experimental and simulation scratch profile. This can be attributed to the reasons that during performing multiple pass scratch test, the cutting condition changes more dynamically as the contact changes, due to asperity in workpiece and the interaction of the tool with previously scratched surfaces. The MPST simulations underpredict the pile-up ratio in comparison to the experiments, this could be due to higher distortion of mesh elements along the overlapping regions that cause lower accumulation of pile-up areas.

In essence, the material removal mechanism that undergoes in MPST is more complicated than in SST. The current simulation model developed does not incorporate a complex contact model or tool wear, which may be the reason for the discrepancies between the experimental and simulation scratch profiles.

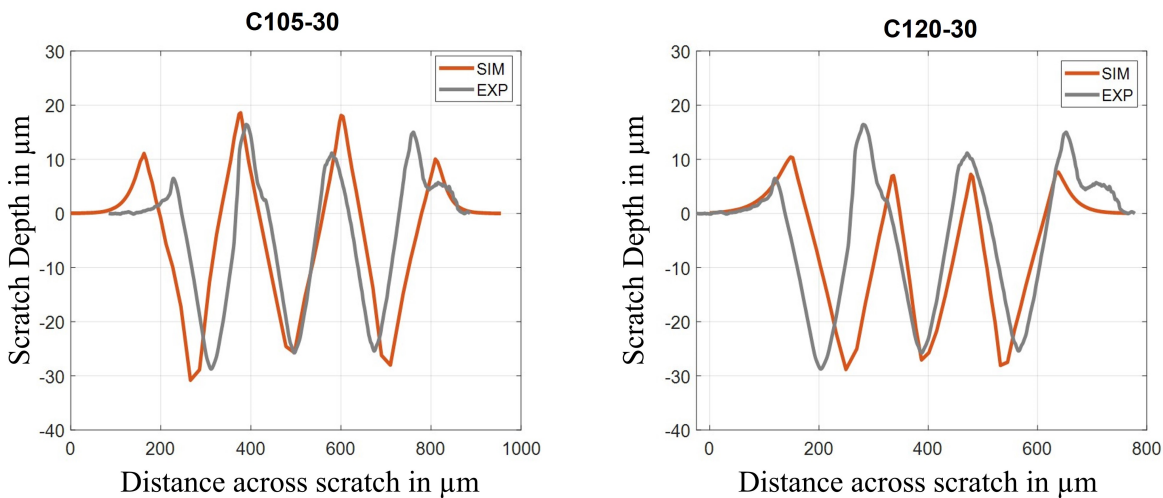


FIGURE 6.26: Experiment vs simulation of the 2D cross section topography of multiple pass simulation using conical indenters

The multiple pass scratch model is further verified based on the process forces measured during each scratch pass and the groove depth measured at each scratch pass.

Fig. 6.27 compares the process forces calculated at each scratch pass from the simulations with experimental measurements. The simulation results are in good agreement with the experimental measures. It is also observed that the simulations are also able to successfully build up tendencies that are observed during the experiments. It can be observed that the process forces remain constant for all the scratch passes. The process forces calculated for the simulation with a wider tool (120°) is higher in comparison to the process forces for the simulation with a narrower tool (105°). This is due to fact that the wider indenter induces larger compressive stresses onto the workpiece. It can also be observed that the process forces measured during pass 2 and pass 3 is higher than the process forces measured during pass 1. While performing pass 2 and pass 3 the tool interacts with the pre-existing scratches and due to interaction with the pile-up regions of the previous scratch. This interaction makes it harder to remove material, leading to higher process forces measured.

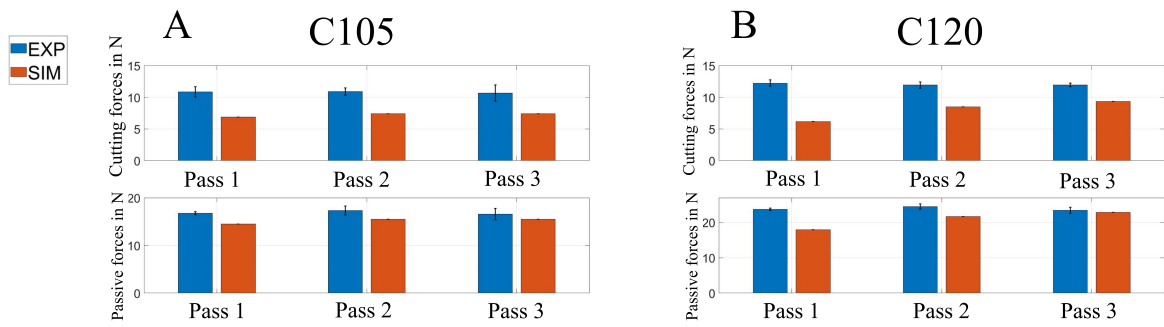


FIGURE 6.27: Experimental vs simulation results of the process forces for multiple pass simulation using conical indenters

Fig.6.28 shows undeformed chip thickness with respect to the set depth of cut for simulations performed for all three scratch passes with the 105° and 120° conical indenters. The simulation results are in good agreement with the experimental measurements. It is observed that the groove depth measured for the second pass and third pass is lesser in comparison to the first passes. This is because, there is interaction of the tool with the overlap pile-up regions from the previous scratch. Owing to the increased plowing, the groove area produced is smaller leading to a lower measure in the groove depth. This behavior is supported by the increased measurements in the process forces during scratch pass 2 and pass 3.

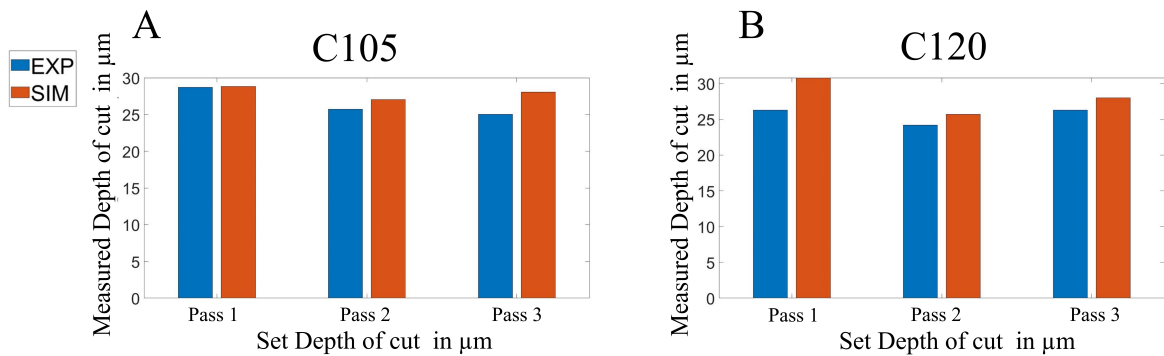


FIGURE 6.28: Experimental vs simulation results of the undeformed chip thickness for multiple pass simulation using conical indenters

Therefore, it can be concluded that the results from the conical multiple pass scratch model verify with the experimental measurements. Based on the sensitivity study performed by varying tool apex angle, the simulations can build the tendencies that were typically observed while performing multiple pass scratch tests (MPST). So, the multiple pass scratch model can capture the complex material removal due interaction between the individual scratches. This provides valuable insights to understand a much more complicated material removal that occurs during grinding.

6.7.2 Results: 3D pyramidal multiple pass scratch model

In this section, the results from multiple pass scratch simulations performed using pyramidal indenters are presented.

Fig. 6.29 shows the 2D scratch profile of the multiple pass scratch simulation performed with the 105° and 120° pyramidal indenters. Comparing the 2D topography with experiments, the simulation groove area resembles the experimental groove area. There is good agreement of the groove depth and groove areas between experiment and simulation. It can also be observed that overlap between the pile-up regions is less prominent for the pyramidal indenters in comparison to the conical indenters (refer Fig. 6.26). Also it can be observed from Fig. 6.29 B, that the pile-up ratio decreases with increase in tool apex angle. MPST pyramidal simulations successfully reproduce a similar tendency as observed in experiments. A wider tool indenter induces a larger groove and a smaller pile-up. However, like MPST results of conical indenter, there are some discrepancies observed between simulation and experimental results. In pyramidal MPST simulations also an under-prediction of pile-up areas are observed, this underestimation may be caused by more mesh element distortion along the overlap zones, which results in less pile-up area accumulation.

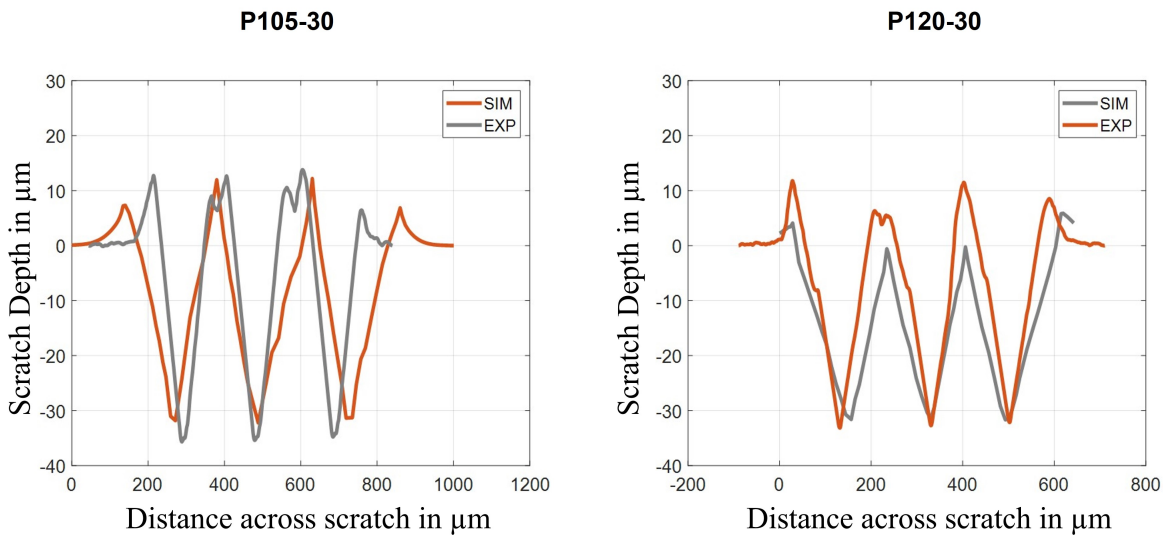


FIGURE 6.29: Experiment vs simulation of the 2D cross section topography-multiple pass simulation using pyramidal indenters

Fig. 6.30 compares the process forces calculated at each scratch pass from the simulations with experimental measurements. The simulation results are in good agreement with the experimental measures. It is also observed that the simulations can successfully build up tendencies that are observed during the experiments. It can be observed that the process forces remain constant for all the scratch passes. Showing that the pyramidal indenter is more efficient in removing material with a lower force variation between the individual scratch passes.

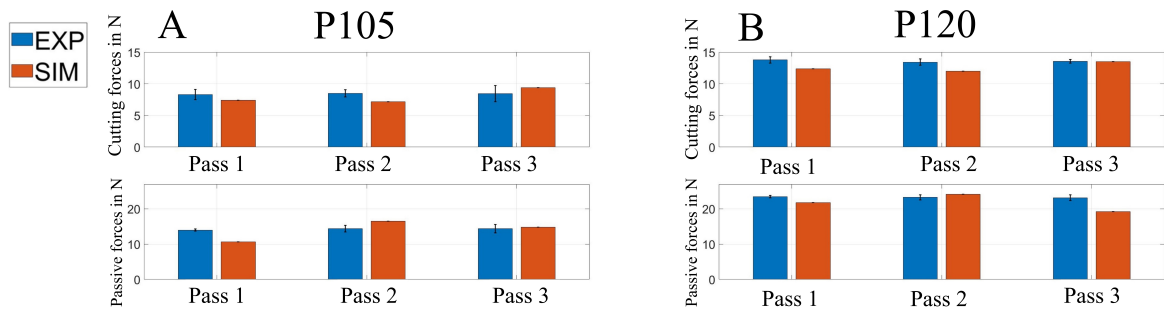


FIGURE 6.30: Experimental vs simulation results of the process forces for multiple pass simulation using pyramidal indenters

Fig. 6.31 shows undeformed chip thickness with respect to the set depth of cut for simulations performed for all three scratch passes with the 105° and 120° conical indenters. The simulation results are in good agreement with the experimental measurements. It is observed that the groove depth is unvarying for all the three scratch passes. This indicates that there is lesser interaction between the individual scratches leading to lower overlap of the pile-up regions. This is also confirmed based on the experimental analysis (Fig. 5.5), that the pile-up areas measured by the pyramidal indenters during MPST is lower than the conical indenters. This leads to producing a more or less constant groove depth for all three scratch passes. With lower variation in the measured grooves, a pyramidal indenter provides a better surface finish. It can be concluded that a pyramidal is much more efficient in removing material, by producing an even surface after machining.

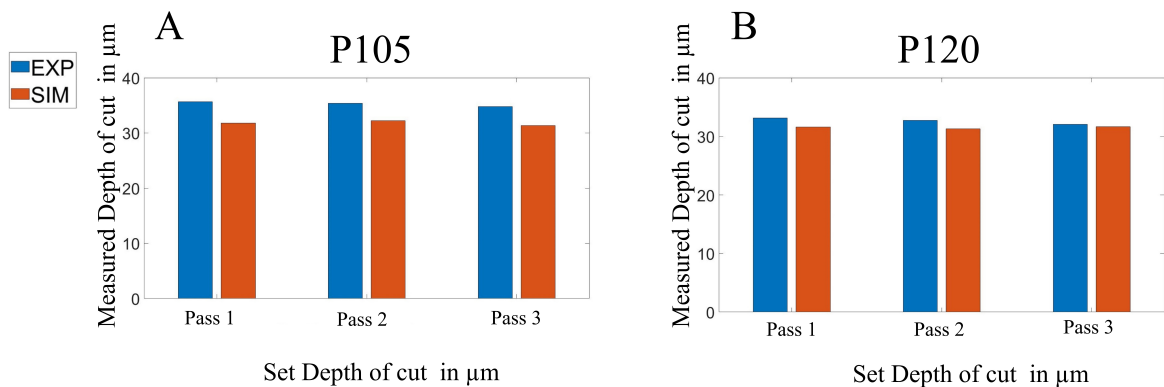


FIGURE 6.31: Experimental vs simulation results of the undeformed chip thickness for multiple pass simulation using pyramidal indenters

Therefore, it can be concluded that the results from the pyramidal multiple pass scratch model verify with the experimental measurements. Based on the sensitivity study performed by varying the tool apex angle, the simulations are also able to build the tendencies that were typically observed while performing multiple pass scratch tests (MPST).

6.8 Analysis of the simulation models based on pile-up ratio and specific energy

Under this section, the 3D scratch models are analyzed based on the pile-up ratio and specific energy.

Fig. 6.32 shows the variation of pile-up ratio with respect to the depth of cut, tool apex angle and indenter geometry. It is observed that the pile-up ratio for both the conical and pyramidal indenters reduces with the increase in the depth of cut and tool apex angle. With increase in the depth of cut, more material is removed, this increases the groove area produced, thereby reducing the pile-up ratio. Similarly, the groove area produced increases while scratching with a wider tool angle, the contact area projected by the tool onto the workpiece increases. Hence the pile-up ratio reduces with the increase in the tool apex angle. It can also be observed that the pile-up ratio is lesser in the case of the pyramidal indenters than the conical indenters. This indicates that the pyramidal indenters are sharper and more stable during material removal, thereby producing lower pile-up areas. The above explained tendencies are also confirmed from experimental investigations performed at the laboratory, refer Fig. 5.1.

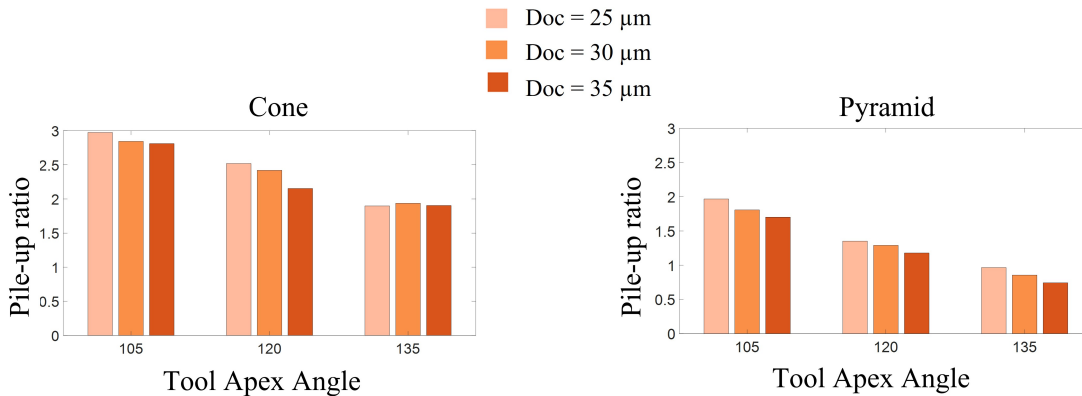


FIGURE 6.32: Variation of pile-up ratio with respect to the depth of cut, tool apex angle and indenter geometry

Fig. 6.33 shows the variation of the specific energy with respect to the depth of cut, tool apex angle and indent geometry. It can be observed that the specific energy reduces with the increase in the depth of cut. This because while producing larger groove areas, the cutting becomes more efficient with less energy lost. It is also observed that with an increase in the tool apex angle the specific energy increases, this is because a wider tool angle produces a larger groove, the cutting forces also increase with the increase in the tool angle. Due to a higher cutting force measured, the specific energy increases with the increase in the tool apex angle. It can also be observed that the specific energy required by the pyramidal indenters are lower in comparison to the conical indenters. This indicates that the pyramidal indenters are sharper and more stable than the conical indenters. Hence the pyramidal indenters prove to be much more efficient in material removal. The above explained tendencies are also confirmed from experimental investigations performed at the laboratory, refer Fig. 5.21.

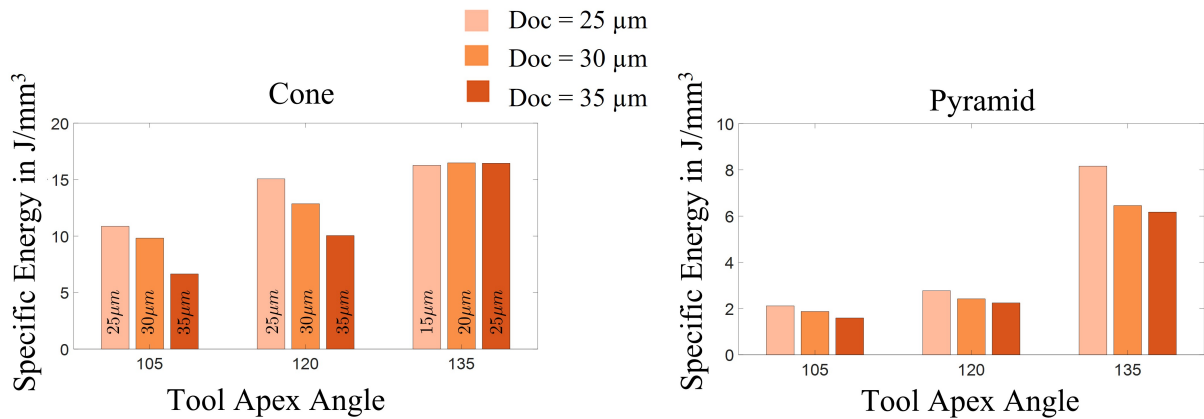


FIGURE 6.33: Variation of the specific energy with respect to the depth of cut, tool apex angle and indenter geometry

Fig. 6.34 shows the variation of the pile-up ratio with respect to single grit and multiple grit scratches. The sensitivity was tested by varying the tool apex angle and indenter geometry. It is observed that the pile-up ratio measured is higher for MPST than SST for both conical and pyramidal indenters. In Fig. 5.4, the similar tendency is observed hence validating the simulations. Due to interaction and overlap of the pile-up areas there is a higher pile-up measured in MPST. When comparing the simulated pile-up areas of pyramidal indenters in comparison to conical indenters, pyramidal indenters measure a lower pile-up ratio. This validates that the pyramidal geometry is more efficient in material removal in comparison to conical indenters. Also, the pile-up ratio measured by pyramidal MPST simulations is lower in comparison to conical MPST simulation, as there is lower interaction between the individual scratches. This is confirmed by experiments performed in the laboratory Fig. 5.5.

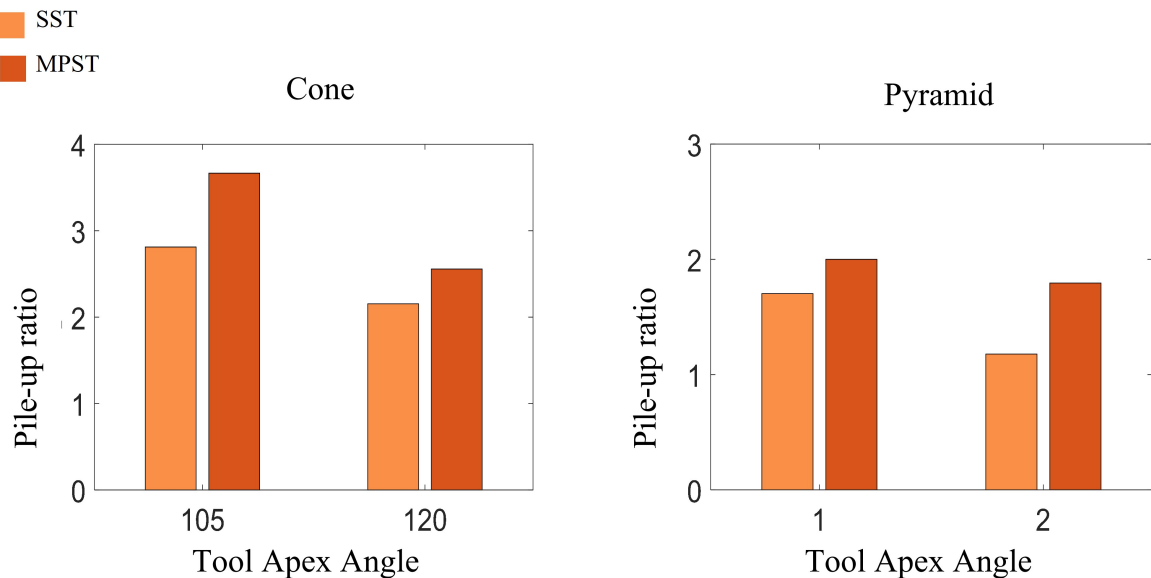


FIGURE 6.34: Variation of the pile-up ratio with respect to SST and MPST

Fig. 6.35 shows the variation of the specific energy with respect to single grit and multiple

grit scratches. The sensitivity was tested by varying the tool apex angle and indenter geometry. It is observed that the specific energy calculated is larger for MPST than SST. Although the groove area measured for the MPST is higher, the specific energy is higher than SST. This is because a wider tool geometry requires a larger cutting force to remove material. The following results are also validated with experimental analysis performed in the laboratory. Fig. 5.23

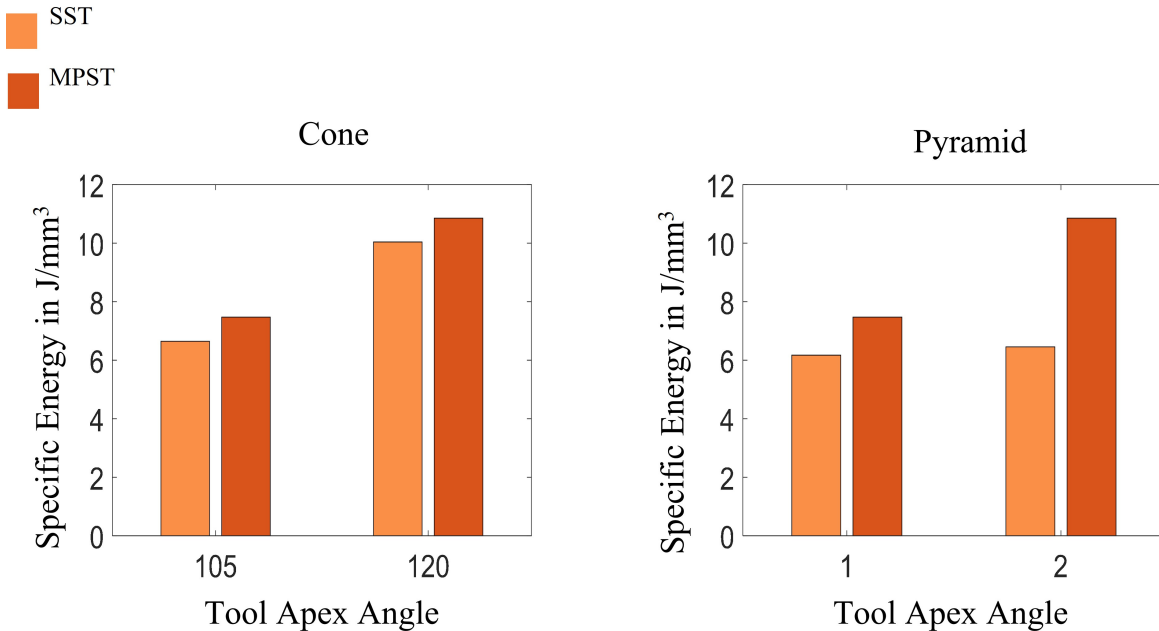


FIGURE 6.35: Variation of the specific energy with respect to single grit and multiple grit scratches

6.9 Summary of grit-workpiece approach simulations

Initially, a 2D orthogonal cutting model is developed to understand the cutting mechanisms and the effect of the rake angle, especially high negative tool rake angles are observed in a grinding process. Two mesh-based methods Lagrangian (LAG) and Arbitrary Lagrangian Eulerian (ALE), and a particle-based methods Smooth Particle Hydrodynamics (SPH) are used to perform 2D orthogonal cutting model. The 2D model is used as a foundation to develop the 3D scratch model. The models are initially benchmarked with a turning experiment for a positive orthogonal rake angle of $\gamma = 20^\circ$. All the discretizational approaches show good agreement with the experimental results in predicting the cutting forces but have a high margin of error in predicting the passive forces. The 2D models are further extended to higher negative rake angles of $\gamma = 0^\circ$ to $\gamma = -60^\circ$ to represent grinding. Although the models qualitatively show an increase in the process forces with increase in negative rake angle, the simulation results do not match the experimental results of the scratch tests performed at the laboratory.

To better capture the complex material removal mechanisms of rubbing, plowing, and cutting that occur during grinding/single grit scratching, a 3D scratch model is developed with the three discretizational approaches LAG, ALE and SPH. Comparing the simulation results, all the three approaches are in reasonable agreement with the experimental results. However, on a closer look, the ALE model predicts the process forces much closer to the experimental results than the LAG

and SPH models. On performing a parameter study with two indenters of cone angles 105° and 120° for the linear speeds $v_c = 200\text{-}1000$ mm/s, it is observed that the ALE model's prediction of the process forces comply with the experimental results confirming the results of the benchmark simulation. Hence, the ALE model is found to be the best discretizational approach to model a single scratch process as it not only predicts the process forces closely to the experimentally measured values, but also builds tendencies observed while performing the single scratch process.

The ALE model is then extensively tested by varying the depth of cut, tool rake angle and indenter geometries (conical and pyramidal). The model is thoroughly validated based on the experimental investigation of the scratch tests performed at the laboratory. The models are validated based on the process forces and scratch topography. The 3D simulation model is in good agreement with the experimental results. The ALE model is then extended to simulate the multiple pass scratch tests (MPST), the models are also validated based on the experimental results. The MPST model is also in good agreement with the experimental results.

Finally, the 3D grit-workpiece simulation models are analyzed based on the pile-up ratio and specific energy. It is confirmed that the simulation results are in good agreement with the experimental results and are also able to successfully build up tendencies, typically observed while performing experiments. Hence, the 3D scratch model is verified and can be used to predict and draw practical conclusions. The predictions of the grit-workpiece model can be extrapolated and used to optimize the grinding process.

Chapter 7

Simulations: Wheel-Workpiece Approach

7.1 Introduction

To further expand the simulation of material removal using FEM from scratching with a single grit to material removal occurring within a full grinding wheel. A precise simulation of the steps involved in making a grinding wheel, from modeling the raw material through compression, sintering, and dressing to produce the finished grinding surface. It is possible to enhance and optimize the individual processes to produce a grinding wheel with the appropriate properties by considering the individual manufacturing phases in the production of the grinding wheel in the simulation. The sample virtual grinding wheel model that was obtained is utilized as a digital twin to simulate the removal of material from a grinding process using FEM.

For FEM material removal simulations of a grinding process, a sample virtual grinding wheel model is constructed. Thus, the FEM simulation was successfully scaled up from a grit-workpiece contact to a wheel-workpiece interaction.

7.2 Mathematical Description of Virtual Wheel Modeling and simulation framework

A through-the-process modeling approach is suggested to deliver a virtual grinding wheel 3D morphology that is comparable to a genuine product in terms of topography and mechanical properties. With modeling of the raw material, compression, sintering, and treatment to produce the final grinding surface, this work seeks to provide a realistic simulation of the manufacturing process of a grinding wheel. It is possible to enhance and optimize the individual processes to produce a grinding wheel with the appropriate properties by taking into account the individual manufacturing phases in the production of the grinding wheel in the simulation. The virtual grinding wheel model that was created can also be used as a digital twin and in future FEM-based simulations of the grinding process. The up-scaling from a grit-workpiece model to wheel-workpiece model is effectively realized by incorporating the virtual grinding wheel model to simulate the material removal process in a grinding operation. The description and results of virtual grinding wheel model as discussed in section 7.2 and 7.3 are based on my previous publication [105].

The objective of this research is to realistically simulate the manufacturing of a grinding wheel. A cut-out of an actual grinding wheel is all that is simulated to provide a realistic model

that is also computationally practical. A surface side of the cut-out, which represents the grinding surface of a grinding wheel, is shown in Fig. 7.1.

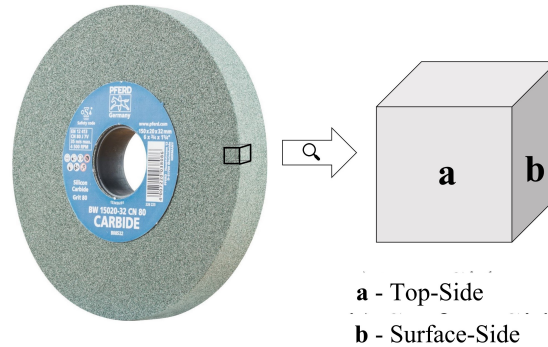


FIGURE 7.1: Grinding wheel cut-out used for simulation [105]

As seen in Figure 7.2, the simulation method largely adheres to the generalized fabrication process [60]. Weighing the raw material, or the quantity of bond substance and abrasive particles, is the initial stage in production. The materials are then combined. The natural packing between the two components, which occurs during this process, determines the distribution of the pores [9]. The final process involves pouring the liquid into a steel mould that has been hydraulically pressed into the required shape of a grinding wheel. The discrete element (DEM) simulation program LIGGGHTS 3.8 is used to simulate the first three fabrication stages. Following this, particles are burned (sintered) and dressed to create the grinding wheel's final surface. MATLAB 2018b is used to replicate those two phases utilizing the particle output from the DEM simulation.

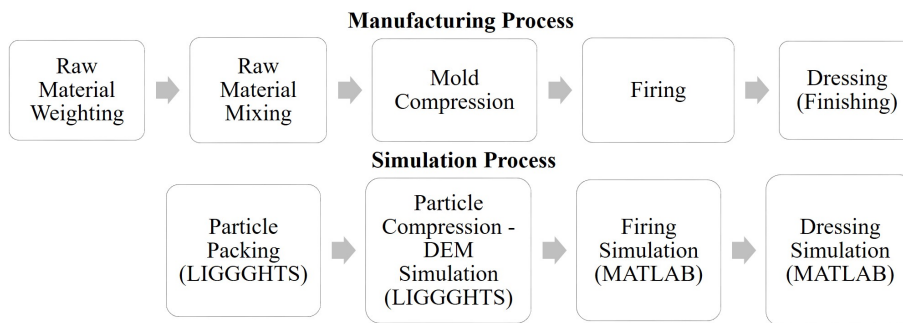


FIGURE 7.2: Simulations process in comparison to manufacturing process; adapted based on [60]

Following the simulation, all the simulation's parameters are defined and shown in Fig.7.3. The DEM simulation makes use of input parameters including material attributes and distribution properties. The corresponding properties are computed in MATLAB for the firing and dressing processes. All relevant quantities, including bonding strength, static grain count, protrusion height, pore volume, and a particle export for the surface topography, are included in the simulation properties acquired.

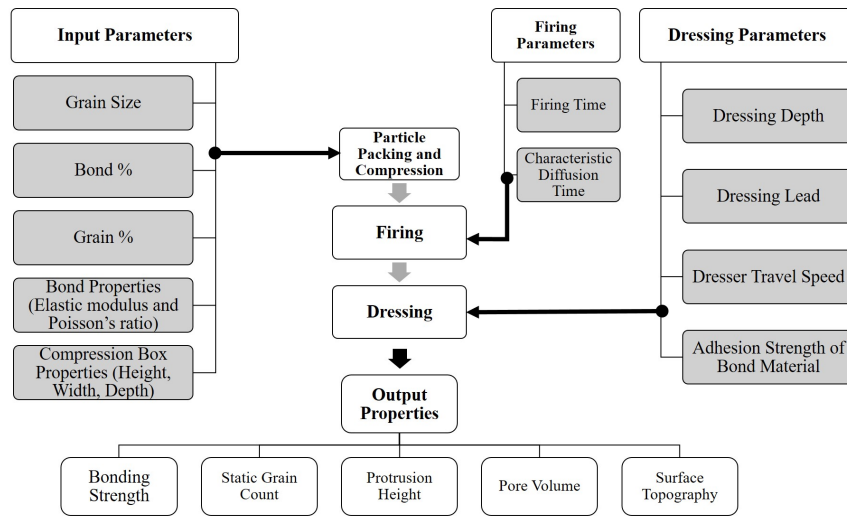


FIGURE 7.3: Input parameters and output properties of simulation; partly adapted based on [59]

Particle mixing and packing

In the simulation, the material mixing is done by creating particles where the bonding material is already surrounding the grain, in comparison to the real fabrication, where this step happens while mixing the grit and the bonding material. The creation of particles in the DEM simulation is done by a step-wise creation of new particles in the time range from $T=0$ to $T=3$, see Fig.7.4. The particles start falling immediately after their creation and the whole system settles down after the creation of particles is stopped at timestep $T=5$. Additional particles outside the desired shape are removed, resulting in randomly distributed particles at timestep $T=6$. The timestep is represented in seconds.

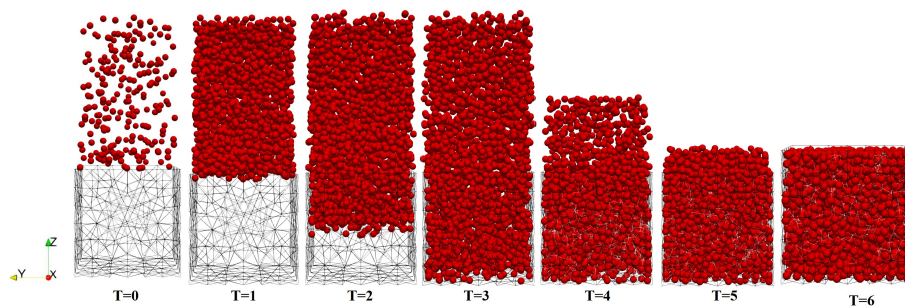


FIGURE 7.4: Visualization of particle mixing and packing in LIGGGHTS [105]

The particles created are a composite of the abrasive grain with radius R_{gi} and the correspondent amount of bond material, resulting in the total particle diameter R_{pi} , as displayed in Fig.7.5. The total particle diameter R_{pi} is dependent on the distribution of bond material and abrasive grain $\frac{f_b}{f_g}$, as well as the grain diameter R_{gi} [[60] p.59]

$$R_{pi} = R_{gi} \cdot (1 + f_b/f_g)^{(1/3)}. \quad (7.1)$$

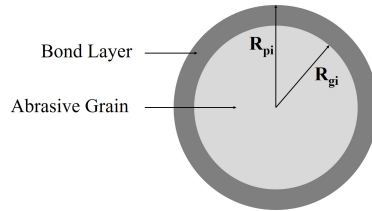


FIGURE 7.5: Visualization of bond layer and abrasive grain; adapted from [60]

Concentric spheres are the particles considered for the simulation since the additional firing and dressing procedures can be executed more quickly and with less computer effort. The study's objective is to create a straightforward and computationally less demanding grinding wheel model to illustrate the fundamental dependencies and tendencies.

Particle compression

In the simulation, the particle compression is realized by moving a plane vertically onto the particles and thereby changing the volume. In this study, the simulation is run by changing the end volume percentage of the modelled simulation box as shown in Fig.7.1. A horizontal plane that represents the actual fabrication process in the DEM simulation is shifted towards the bottom for a specific distance per unit of time [52]. Fig. 7.6 shows a graphic illustration of the compression process. At time step T3, a compression level of 25% is reached by reducing simulation box's volume to 75% its original volume. When more than 0.5 percent of the particle radius is less than the original grain radius R_{gi} , the maximum possible compression is said to have occurred. As abrasive grain is less compressible than bond material, the simulation thus depicts the different material properties of the outside bond material and interior abrasive grain. A vitreous bond medium has a Young's modulus of 6.2 GPA according to [88], but abrasive grains, such as silicon carbide, have a Young's modulus of 400 GPA. Various grit sizes (20-80) are employed for the simulation, and the grain size distribution are described in detail in Table.7.1

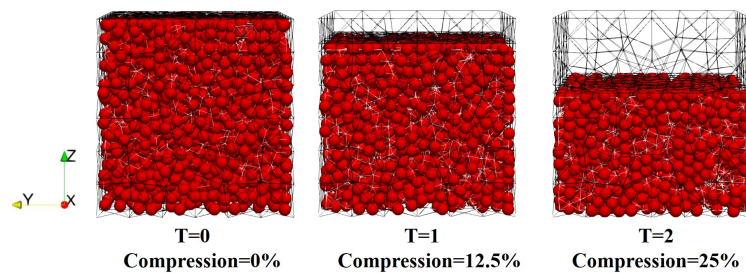


FIGURE 7.6: Compression of particles [105]

Firing

The firing (sintering) of the packed particles is simulated in MATLAB by using the exported particle data from LIGGGHTS, containing the position and radius of every particle in contact and the surface contact area of the connection. The first step in the firing algorithm is the calculation of the new neck radius a , as displayed in Fig.7.7. The characteristic time for the grain-boundary diffusion τ_g is used as a material property [128] and the sintering (firing) time for the grain-boundary diffusion [128] needs to be set. With the use of the initial neck radius a_0 [128], the formula for the new neck radius [60, 128, 14] is derived as shown in equation 7.2.

The exported particle data from LIGGGHTS, which includes the position, radius, and surface contact area of each particle in touch as well as the connection, is used to simulate the firing (sintering) of the packed particles in MATLAB. The new neck radius a is calculated as the first step in the firing method, as shown in Fig. 7.7. The grain-boundary diffusion's characteristic time, τ_g , is used as a material attribute in the simulation [128], and the simulation's sintering (firing) time needs to be adjusted. The formula for the new neck radius is developed using the initial neck radius a_0 as follows [60, 128, 14]

$$a = a_0 \cdot \left(\frac{192t}{\tau_g} \right)^{(1/6)} \quad (7.2)$$

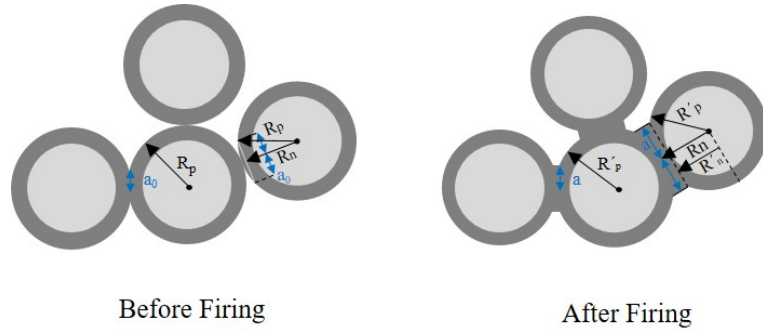


FIGURE 7.7: Development of particle connections and neck radius for compression and firing; adapted from [60]

In Fig.7.7 the formation of multiple particles before and after firing is displayed. Each particle i in the set of n particles has a radius R_{pi} before firing and a radius R'_{pi} after firing. Every connection of a particle (bond) j in the set of m connections has a neck radius a_{0j} before firing and a neck radius a_j after firing. The calculation of the particle radius R_{ni} (see Fig.7.7), which connects the particle center with the respective middle point of the neck, is calculated using Pythagoras' theorem.

$$R_{ni} = \sqrt{(R_{pi}^2 - a_{0j}^2)} \quad (7.3)$$

The distance of the particle centre towards the cutting edge of R_{ni} and the new neck boundary is defined as R'_{ni} (see Fig.7.7) and calculated as $h_i = R_{ni} - R'_{ni}$. The calculation of the new particle radius, as shown in Fig.7.8, is based on the law of conservation of mass. The equation

and its graphical representation are

$$\underbrace{\left(\frac{4}{3}\pi \cdot R_{pi}\right)^3}_A = \underbrace{\left(\frac{4}{3}\pi \cdot R'_{pi}\right)^3}_{A_1} + \sum_{i=1}^n \sum_{j=1}^m \left[\underbrace{a_i^2 \pi \cdot (R_{ni} - R'_{ni})}_{A_2} - \underbrace{\frac{\pi}{3} h_j^2 \cdot (3R'_{pi} - h_j)}_{A_3} \right] \quad (7.4)$$

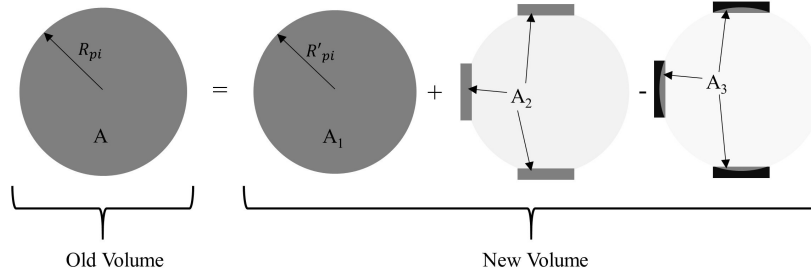


FIGURE 7.8: Visualization of new radius calculation; adapted from [60]

Dressing

To reduce thickness, correct balance or parallelism, and generate unique features (such as sharp edges), dressing of particles is typically done with a single-grit diamond [60]. The grinding wheel rotates at a specific speed while the dresser stays in place during the dressing operation. The dresser traverses the entire surface area of the grinding wheel as it moves horizontally at a set travel speed. The dresser should ideally be set up so that it travels at a specific speed and hits each section of the surface exactly once (also known as the overlap-ratio), without cutting off any other areas of the surface [111]. The dresser's cutting angle is fixed to 90° for the sake of simplicity during simulation in this investigation. Although it is its own research field (see, for example [111, 48, 115]), the impact of various dressing angles and procedures on the surface topography largely relies on the methodologies used in this work. As seen in Fig.7.9 there are three different outcomes when the dresser collides with a particle. The first scenario is that the particle is struck by the dresser on its entire surface, removing the grain regardless of the dressing force or bonding force. The second possibility is that the particle is partially struck by the dresser, but that the force of the dresser is greater than the bonding force of the particle, causing the removal of the grain. The third possibility is that the particle is partially struck by the dresser, but the bonding force is greater than the force of the dresser, causing a grain to be cut (broken).

Complex grain crack propagation at the abrasive grit can be simulated with the finite element method [8, 24]. Although grain crack propagation can provide some realistic insights in the dressing process, it is highly computationally intensive. Also the effect of temperature plays an important effect in the dressing of vitrified grinding wheel investigated by [64]. However, in this research a simple dressing algorithm based on [60] is chosen considering the high number of grits to be dressed, which would be less computationally intensive.

The finite element method may simulate complex grain crack propagation at the abrasive grit [8, 24]. Grain crack propagation is a highly computationally costly method even if it can offer some actual insights on the dressing process. Given the large number of grits to be dressed

in this study, a straightforward dressing approach based on [60] was selected as it would need minimal computing power.

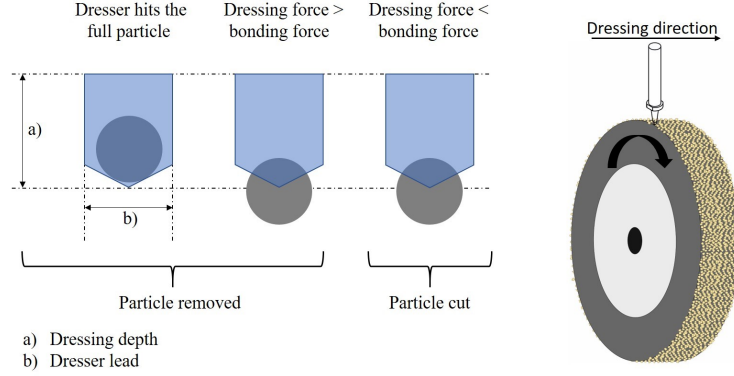


FIGURE 7.9: Visualization of dressing process [105]

For the calculation of the dressing force F_t , an empirical formula is used [58]

$$F_t = 9.631a_{dp}^{-0.1992} \cdot f_d^{-0.1774} \quad (7.5)$$

It is based on the dressing depth a_{dp} (in mm) and the dresser travel speed f_d (in $\frac{\text{mm}}{\text{min}}$). The bonding force F_b is dependent on material-specific properties of the bonding material [72]. In this study, a specific bonding force for the material of $F_{bsp} = 800 \text{ N/mm}^2$ is used, depending on the surface area of each bonding a_j of a particle. Thus, the bonding force of a particle i is

$$F_{bi} = F_{bsp} \cdot \sum_{j=1}^m a_j \quad (7.6)$$

Calculation of output variables

Two major output variables allow the evaluation of the results of the simulation: the static grain count and the protrusion height.

The static grain count is the number of grains on the wheel surface in a certain area see Fig.7.10a [60, 56], though it differs from the kinematic grain count which considers only the grains interacting with the workpiece material. The static grain count value is not always reliable as it depends on an arbitrary surface depth [56], though it is commonly used in research [27, 116, 61, 56, 62]. To solve this issue, this study introduces an alternative static grain count, where the surface depth depends on the average diameter of particles. Thus, the different grain sizes can be compared more reliably, as the surface depth adapts towards their properties and to the changing height of the bond surface.

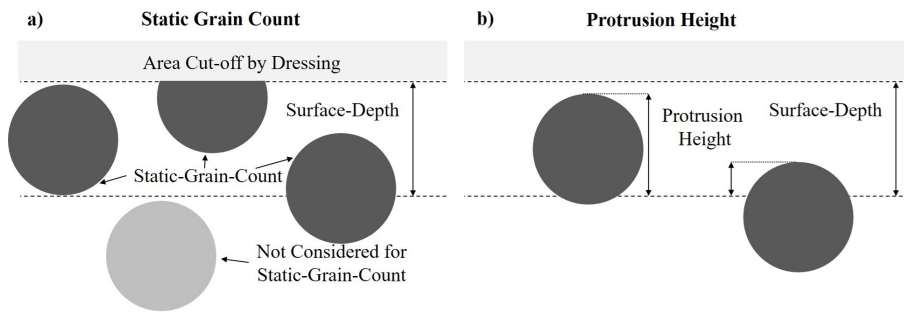


FIGURE 7.10: Visualization of a) static grain count and b) protrusion height; Partly adapted from [56]

The protrusion height is calculated as described in [56] and is visualized in Fig.7.10 b). The protrusion height is defined as the height difference of a grain tip from the bond surface [56]. The bond surface is set to an arbitrary height making it difficult to compare the obtained results with other studies [56]. In this study, all the particles that are a part of the static grain count along a specific depth are considered for the measurement of the surface depth. For the alternative protrusion height, this surface depth definition is applied, making the measurement accurate irrespective of grinding wheel grit size.

Surface calculation and modelling

Using the program ParaView 5.7, the topography of the grinding wheel is shown. The output coordinates are defined in a MATLAB simulation in order to represent the surface correctly. The creation of the coordinates for various particles and the visualization of the surface using these points are shown in Fig.7.11. The first phase involves identifying the particles that may be seen on the surface (top view). The second stage involves determining the particle's tip height. To depict the shape of the abrasive particles accurately and realistically, a third phase involves the creation of up to 16 additional data points. These extra data points are then examined for spacing before being eventually eliminated to smooth the output surface and eliminate unexpected spikes. The exported data points are joined in the visualization's last stage to create a virtual wheel topography.

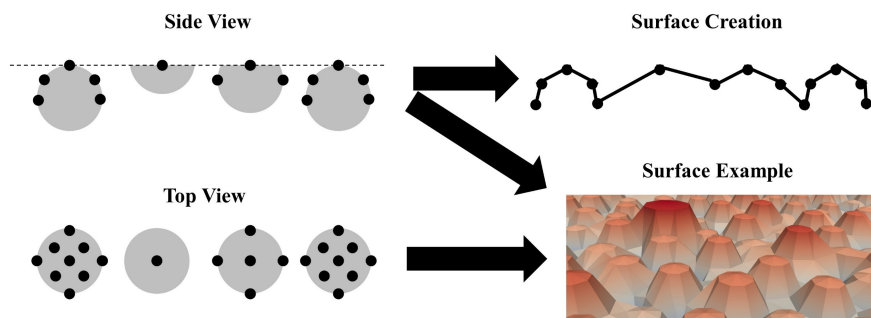


FIGURE 7.11: Visualization of simulated grinding wheel surface [105]

To improve comprehension and verify the accuracy of the calculations and hypotheses, all steps taken throughout the simulation are shown. A sample visualization of all steps with grit size 30 and a 5% particle compression is shown in Fig.7.12.

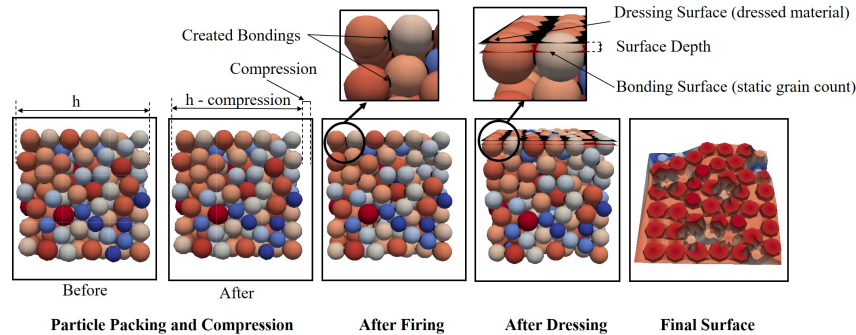


FIGURE 7.12: Visualization of the simulation steps.

7.3 Results of the virtual grinding wheel model

To attain equivalent findings, the simulation properties for the particles, firing, and dressing in this study were chosen similarly to those in [60] and can be found in Table 7.1. Based on the selected grit size, the size of the metal cast model is changed so that the number of particles at the cube's edges stays constant at around 25. The simulation can be expanded upon and is independent of the cast's size or shape. Since box geometry requires less processing, it is originally picked. Surface depth is set to 0.1 mm for the output variables' calculation. The material properties of the vitreous bond material, as described in [72] and empirically studied in [88], are used for particle compression. The dressing wheel speed is set so that the dresser lead only makes one contact with each section of the grinding wheel. There are nine different grit sizes used (grid numbers 20, 24, 30, 36, 46, 54, 60, 70, and 80), as specified in Table 7.2, with a size distribution and average grit size, as per [41]. The grain diameter values fall within the 95% confidence interval for the maximum and minimum diameters because the standard deviation for the normal distribution is calculated for a 95% confidence interval. According to equation 7.1, the particle radius (grain + bonding) was determined. Pores made up the remaining percentage, with a grain fraction of 49% and a bond fraction of 10%.

The following simulation results are divided into three subsections as follows. The impact of the output variables for a 10% percentual dressing is discussed in the first section. The second portion uses topographical measurements from trials conducted in the laboratory and measurements found in the literature [60] to validate the virtual grinding wheel model. The practical considerations of choosing a grinding wheel for a specific application are covered in the final section utilizing the grinding wheel model.

TABLE 7.1: Simulation properties and settings [105]

Particle properties	
Grain fraction	49%
Bond fraction	10%
Young's modulus of grain	400 GPa
Young's modulus of bond	6.2 GPa
Poisson's ratio	0.3
Maximum particle compression force	$35 \frac{\text{N}}{\text{mm}^2} \approx 5000 \text{ PSI}$
Firing properties	
Firing time	20 hours
Grain-boundary diffusion property	290 hours
Dressing settings	
Wheel diameter	250 mm
Wheel speed	20 mm/s
Dresser travel speed	300 mm/min
Dressing depth	10%
Dressing lead	0.19 mm

TABLE 7.2: Grain sizes and distribution used for simulation [105]

Grit size	d_{mean}	d_{max}	d_{min}	95% Confidence interval
20	0.850 mm	0.938 mm	0.762 mm	0.0440 mm
24	0.676 mm	0.762 mm	0.589 mm	0.0432 mm
30	0.532 mm	0.589 mm	0.476 mm	0.0282 mm
36	0.415 mm	0.476 mm	0.354 mm	0.0305 mm
46	0.323 mm	0.354 mm	0.291 mm	0.0157 mm
54	0.273 mm	0.291 mm	0.255 mm	0.0090 mm
60	0.233 mm	0.255 mm	0.211 mm	0.0110 mm
70	0.194 mm	0.211 mm	0.178 mm	0.0082 mm
80	0.165 mm	0.178 mm	0.152 mm	0.0065 mm

7.3.1 Analysis of output parameters based on dressing 10%

This section analyzes the output variables of alternative static grain count and alternative grain protrusion height. For the virtual wheel simulation, grit sizes 20–80 will receive a 10% percentual dressing.

Alternative static grain count

The alternate static grain count per cm^2 in comparison to the absolute percentage of compression is shown in Fig. 7.13. According to the theory, empirical findings [56], and simulation of [60],

the alternative static grain count is highest for grit 80 and decreases with grit size, with grit 24 having the lowest static grain count. Surprisingly, all the plots for the various grits display the same distinctive slope: at first, there is a very modest, but continuous increase, followed by an exponential increase. The slope eventually flattens out at increasing compression levels. As a result, before the maximum compression, a value close to the maximum static grain count is obtained. The larger grit sizes are where this trend is seen to be more prevalent.

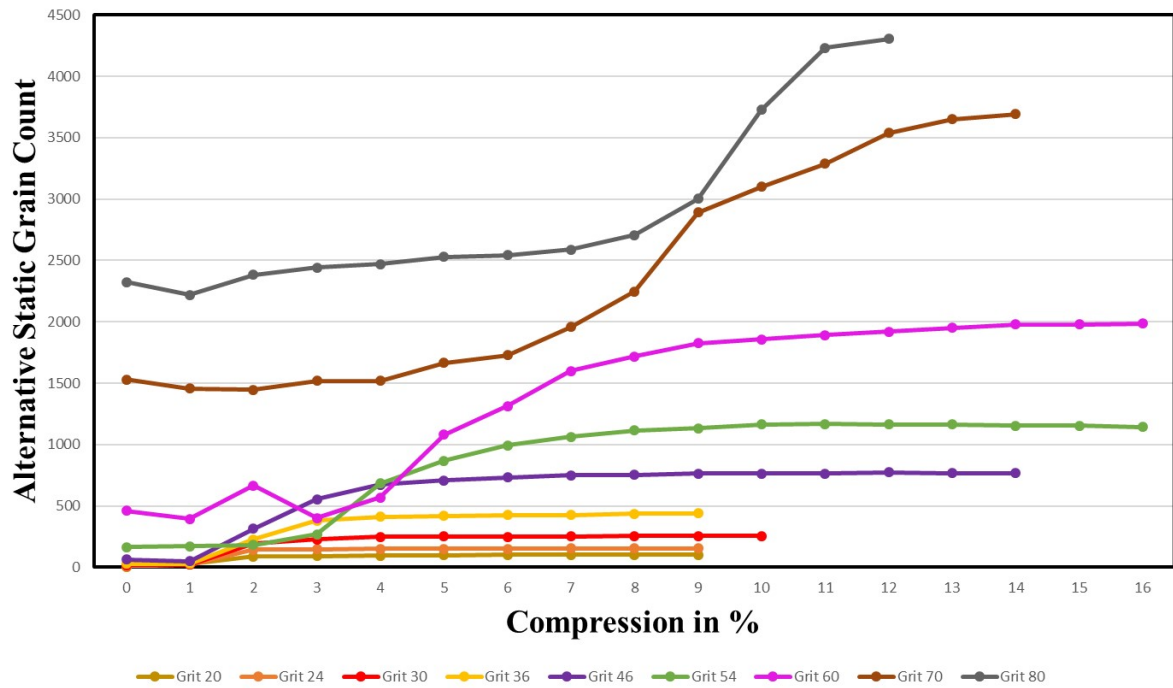


FIGURE 7.13: Alternative static grain count dependent on different percentages of compression [105]

Alternative average grain protrusion height

The height of the grain tip from the bond surface, also known as the protrusion height, is a critical parameter that greatly affects both the wear of the wheel and the roughness of the generated work surface. According to [24], the protrusion height should be measured at 35% of the particle diameter. It is challenging to compare the grit sizes when using the standard protrusion height measure at a constant height of 0.1 mm, as in [60]. Some grit sizes, such as 20, 24, and 30, cannot be used because of the determined surface depth since compression causes the particles below the top row to also be taken into account, this result is not desired. In order to compare the grits and accurately depict the bond surface, an alternate definition of the surface depth is employed, this is called as the the alternative average protrusion height. This value calculated is reliable, while comparing the protrusion height between various grit sizes.

Fig.7.14 compares the average alternative protrusion height of particles considered in the static grain count with the percentage of absolute compression. For all grits, the average protrusion height starts off lower, grows significantly until 3% compression, and then stays constant for

greater compression levels. Grit 70 and 80 are anomalies, where the maximum is obtained at 7%. With increasing grit size (decreasing particle size), a distinct trend toward a decreasing protrusion height can be seen. This trend is consistent with simulation data from [60] and empirical results from [56]. The numbers are comparable when comparing the computed protrusion height values to the simulation findings of [60], however for finer grits, the values in this study are marginally higher. This could be the result of different compression levels. According to another study [24], the average protrusion height of a particle is around 35% of the grit diameter, or 0.0955 mm for grit 54, hence the study's values fall within an acceptable range.

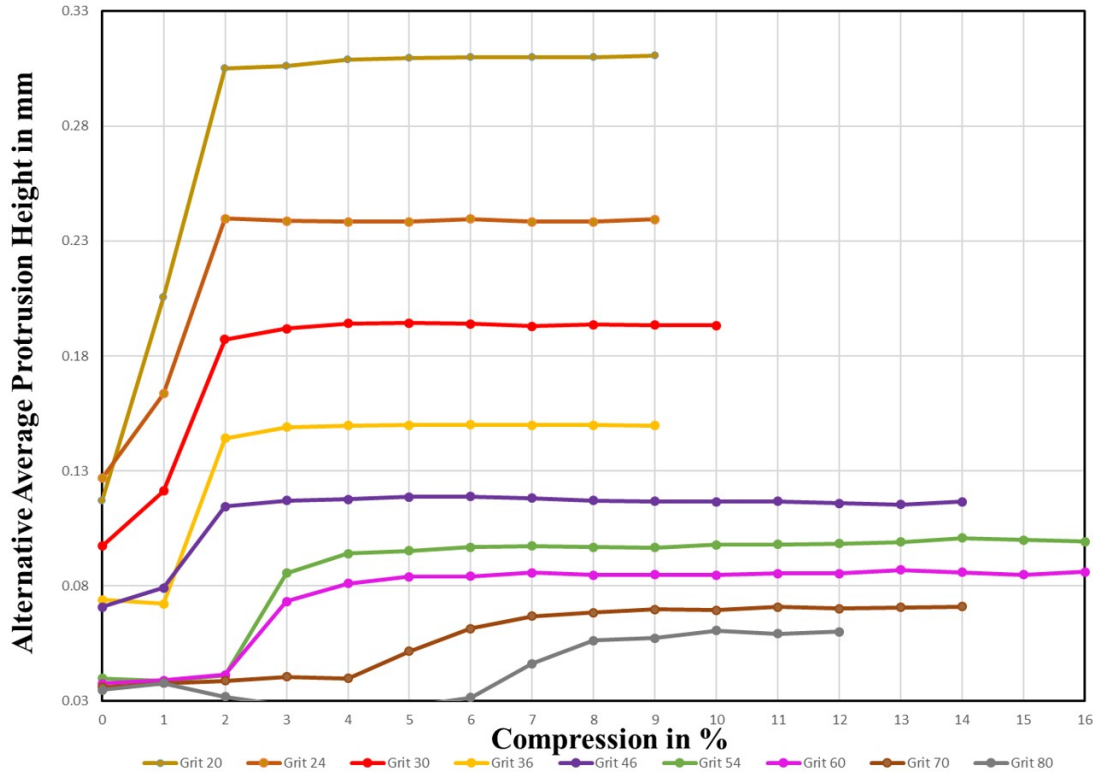


FIGURE 7.14: Alternative average protrusion height dependent on different percentages of compression [105].

7.3.2 Grinding Wheel Measurement and Model Verification

This part uses a white light microscope to test two silicon carbide grinding wheels to evaluate a simulation model that is based on static grain count and protrusion height.

Grinding wheel measurement platform

Two silicon carbide wheels with grit sizes of 60 and 80 were measured under the Keyence VHX-7000 microscope to look at the 2D and 3D grinding wheel surface topography in order to validate the model in terms of the static grain count and protrusion height (see Fig. 7.15). The static grain count is determined by analyzing the 2D grinding wheel topography, as shown in Fig. 7.16. The number of grains counted per square centimeter on the surface of the wheel is known as the

static grain count. In this investigation, the static grain count was calculated in three regions on the grinding wheel surface for both grit sizes, and the protrusion height was determined as the distance between the grain tip and the bond surface. Therefore, as illustrated in Fig. 7.17, the 3D wheel surface is created from the three randomly selected locations on the wheel surface.

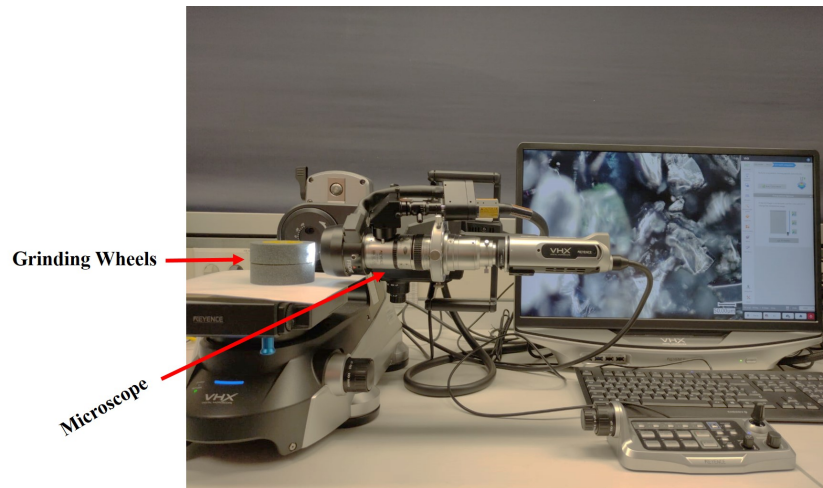


FIGURE 7.15: Grinding wheel topography detection platform

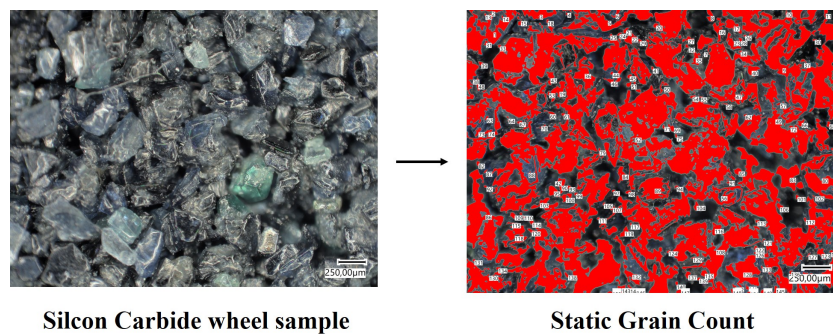


FIGURE 7.16: Detected 2D surface topography [105]

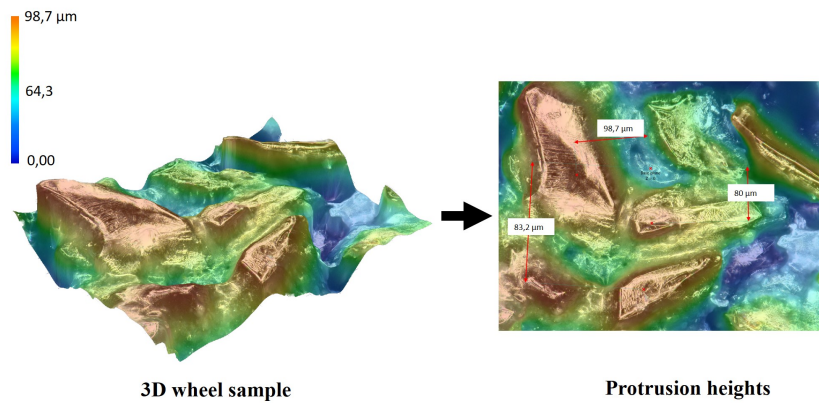


FIGURE 7.17: Detected 3D surface topography [105]

Model Validation

First, the simulations with a 10% dressing are compared to measurements of the wheel topography obtained from experiments conducted in the lab and from published works on modeling [62]. Two output parameters, the static grain count, and the protrusion height, which are extracted at maximum compression, are used to evaluate the simulation model.

Figure 7.18 describes the static grain count as a function of the grit size. It can be observed that the simulations can predict the static grain count per cm^2 in good accuracy with the measured grinding wheel topography data (experimentally obtained and literature [62]). Over the compared grit sizes the simulated static grain count values do not deviate more than 5%. It is also observed that the static grain count increases with increase in the grit size (decreasing particle size), this tendency is also observed from the simulation results. The static grain count is shown as a function of grit size in Fig. 7.18. With the measured grinding wheel topography data (obtained by experimentation and literature [62]), simulations can accurately forecast the static grain count per cm^2 . The simulated static grain count values do not vary by more than 5% across the compared grit sizes. Additionally, it is noted that the static grain count rises as the grit size (or particle size) decreases; this trend is also noted in the simulation findings.

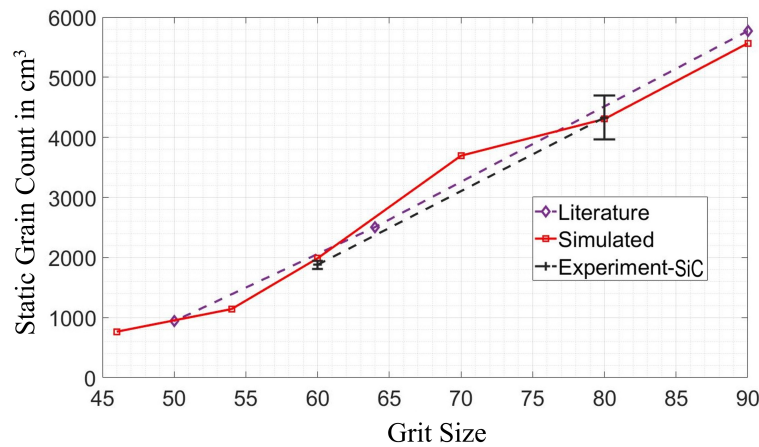


FIGURE 7.18: Comparison of simulated static grain count values with measured values from experiments and literature [62]

The protrusion height is shown in Fig. 7.19 as a function of grit size. As it can be seen, using the measured grinding wheel topography data (obtained from experimentation and literature [62]), simulations are able to forecast protrusion heights within an acceptable variation range. The simulated values do not deviate from the measured protrusion height by more than 5% when compared to various grit sizes. It is obvious that as grit size increases (particle size decreases), the protrusion height lowers. Thus, the topographical measurements from laboratory trials and measurements by [62] are in good agreement with the results of the virtual grinding wheel simulation model. However, there is some deviation between the simulation results and experimental finding, this can be due to the fact that real grinding wheels are fabricated with a mixture of various grit shapes and sizes, enhancing these effects in the simulation can help bridge the gap between experiments and simulations.

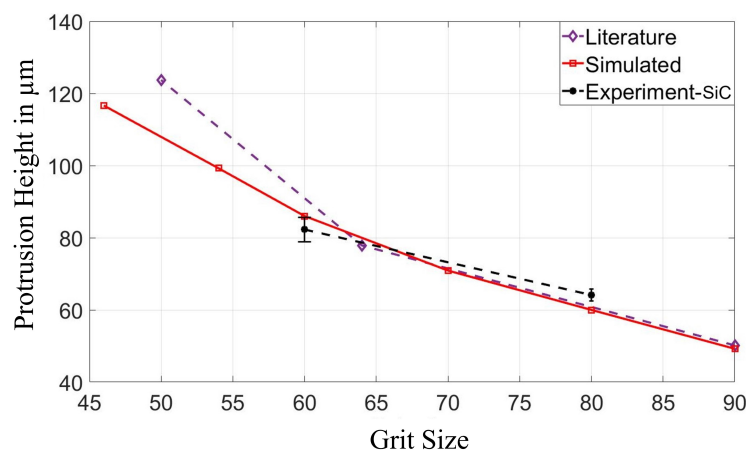


FIGURE 7.19: Comparison of simulated protrusion height values with measured values from experiments and literature [62]

7.3.3 Grinding wheel surface

This section analyzes the simulated dressing-generated grinding wheel topography using a few input/output factors. The MATLAB computations for the virtual wheel surface are then shown in ParaView. In order to represent the computed data's realistic wheel topography, an appropriate elevation grid filter is used.

Alternative protrusion height

Fig. 7.20 and Fig. 7.21 show the surface topography of grits 20 and 80 with a range of compression values from 0% to 100% of the maximum compression. The surface produced is unstructured for small percentages of compression (such as 0%), and more evenly organized for larger degrees of compression. Over 50% of maximal compression, a highly flat and homogeneous surface is typically attained. Additionally apparent is the fact that when compression increases, sporadic surface caves begin to vanish, hence diminishing the surface's pore volume. The surface topography seems to be consistent with the surface simulations [60]. Below 50% of maximal compression, the protrusion height increases, and the particle distribution is uniform. When comparing the contour plots for grit 20 and grit 80, it can be seen that at maximum compression, the grit size 80 particles are more uniformly distributed and have less apparent pores.

Alternative Protrusion Height in mm

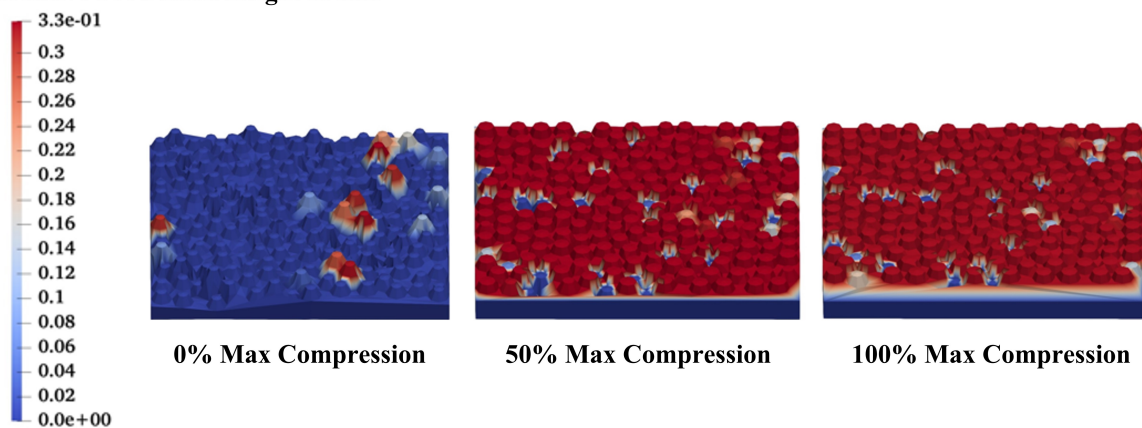


FIGURE 7.20: Grit 20 ($d_{\text{mean}} = 0.85\text{mm}$) surface topography with alternative protrusion height at 0%, 50% and 100% maximum compression [105]

Alternative Protrusion Height in mm

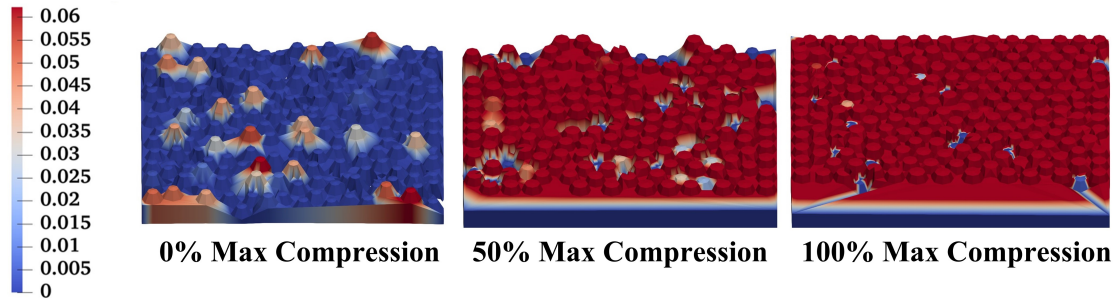
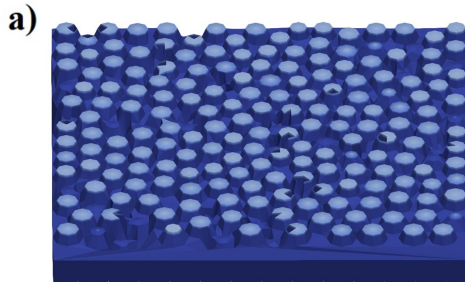
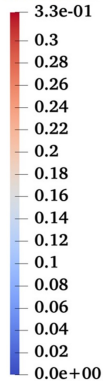


FIGURE 7.21: Grit 80 ($d_{\text{mean}} = 0.165\text{mm}$) surface topography with alternative protrusion height at 0%, 50% and 100% maximum compression [105]

Protrusion height vs. alternative protrusion height

In this study, a new surface depth metric is developed to analyze the functional variations more accurately between the grit sizes. Fig.7.22 compares the contour plots' protrusion height and alternative protrusion height for easier comprehension and interpretation. One can see that, especially for tiny grit sizes (large particle sizes), the alternate protrusion height in Fig. 7.22 b) differs from the standard protrusion height in that figure. The region surrounding the grit's center is considered in addition to the particles at the top surface. Given that this metric adapts to the corresponding particle diameter, this representation more closely represents the actual surface for each grit size.

Protusion Height in mm



Alternative Protusion Height in mm

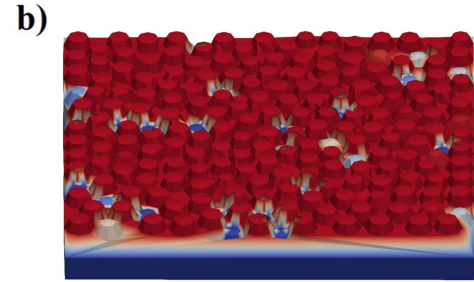
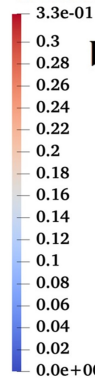


FIGURE 7.22: Grit 20 surface topography comparison for a) protrusion height and b) alternative protrusion height

7.3.4 Practical applications

The performance of grinding is greatly influenced by four variables: bonding strength, static grain count, protrusion height, and pore volume. This selection of grit size and compression level is essential. Protrusion height and total pore volume fluctuate non-linearly, although bonding strength and static grain count largely depend linearly on each other. Thus, it is important to be clear about the needs before choosing the grit size and compression level. See Fig. 7.23 for a radar

chart that aids in many useful practical conclusions based on the requirements. For instance, if coarse grinding is necessary, it may be suggested to utilize a tiny grit size (larger particle size) at maximum compression. The bonding strength is high, resulting in greater endurance, the protrusion height is high, allowing for deeper penetration, and the pore volume is high, allowing for the fitting of more abrasive material into the pores. The static grain count, however, continues to be low. The use of a large grit size (smaller particle size) at maximum compression can be suggested if the necessity is for fine grinding, on the other hand. When this happens, a high static grain count produces a smooth surface. However, the bonding strength, protrusion height, and pore volume are low. In light of the requirements, the radar charts can help manufacturers reach useful conclusions.

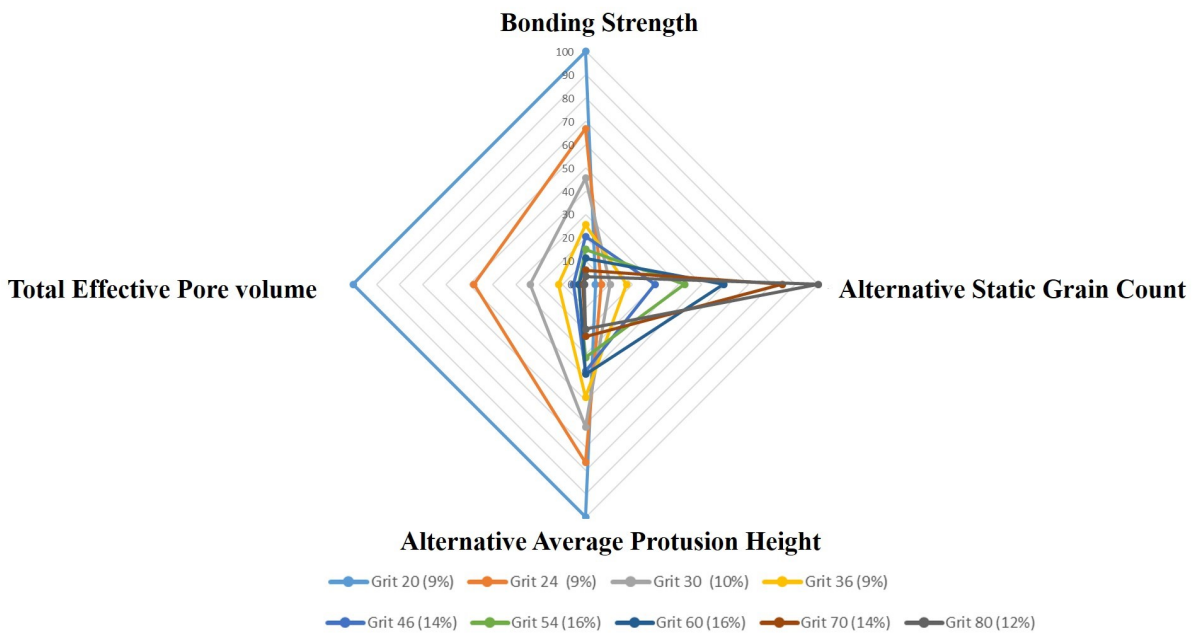


FIGURE 7.23: Radar chart optimized for maximum bonding strength and alternative static grain count at maximum compression; Values in % of the maximum possible value [105]

7.4 Up-scaling from grit-workpiece to wheel-workpiece simulation

To simulate the material removal at a macroscopic scale, the up-scaling from grit-workpiece approach to wheel-workpiece approach is necessary. Under this section, two simulations are performed that enable the up-scaling from grit-workpiece approach to wheel-workpiece approach. The first simulation employs the developed virtual wheel model (refer section 7.4.1) as a digital twin of a sample grinding wheel specimen to simulate using FEM the material removal that occurs during a grinding process.

The second simulation employs a perfectly flat grinding wheel surface without considering the grinding wheel topography, to perform the material removal simulations that occur during grinding (refer section 7.4.2).

7.4.1 Simulation with sample wheel specimen (virtual grinding wheel model)

Under this section, the FEM simulation setup is explained using the virtual grinding wheel topography model. As shown in Fig.7.24 A, the developed sample grinding wheel model is initially exported from ParaView 5.7 as a .stl file. The .stl file is pre-processed and repaired such that the model can be successfully imported as geometry in ABAQUS as shown in Fig.7.24B. The imported sample grinding wheel cut out is modelled as a rigid shell and the workpiece as a deformable body.

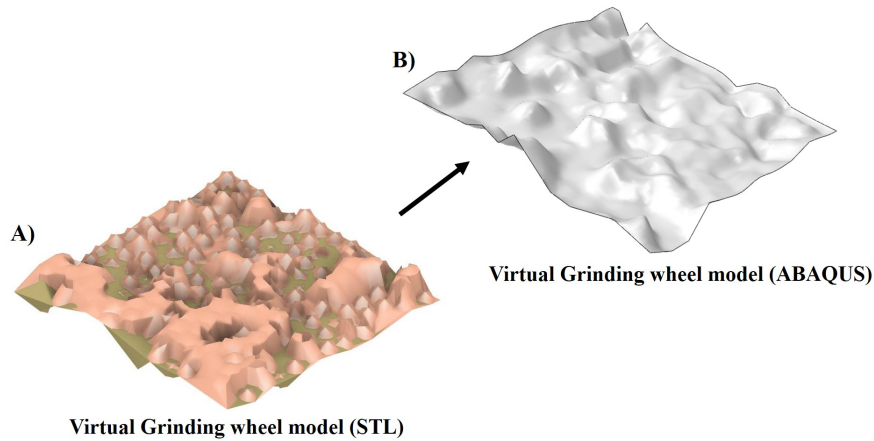


FIGURE 7.24: Translation of the virtual wheel model from .stl file (A) to ABAQUS geometry model (B)

The Fig.7.25 shows the assembly of the virtual wheel specimen and the workpiece. The simulation is performed in a similar manner to that of the 3D single grit scratch simulation. The simulation consists of two steps: in the initial step, the desired depth of cut is assigned in the negative y direction and then the virtual wheel is assigned with a linear cutting velocity. Due to the interaction between the wheel and workpiece, material removal takes place.

Fig.7.26 shows the displacement (negative y -direction) contour plot of the wheel-workpiece simulation. From the contour plot, the ground surface topography can be distinguished from the un-ground surface topography. It is to be noted that the virtual wheel model is not initiated with a round trajectory, similar to what is observed in a grinding process. Hence typical grinding grooves are not observed, as typically observed in a grinding process.

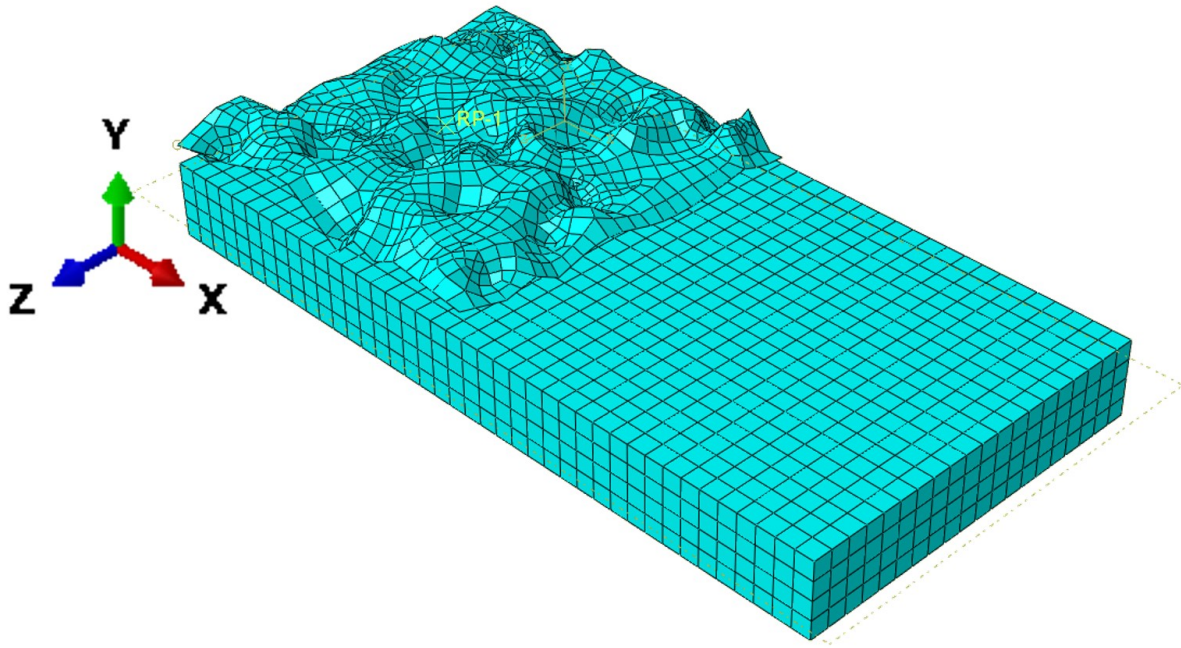


FIGURE 7.25: Assembly of the virtual wheel specimen and the workpiece

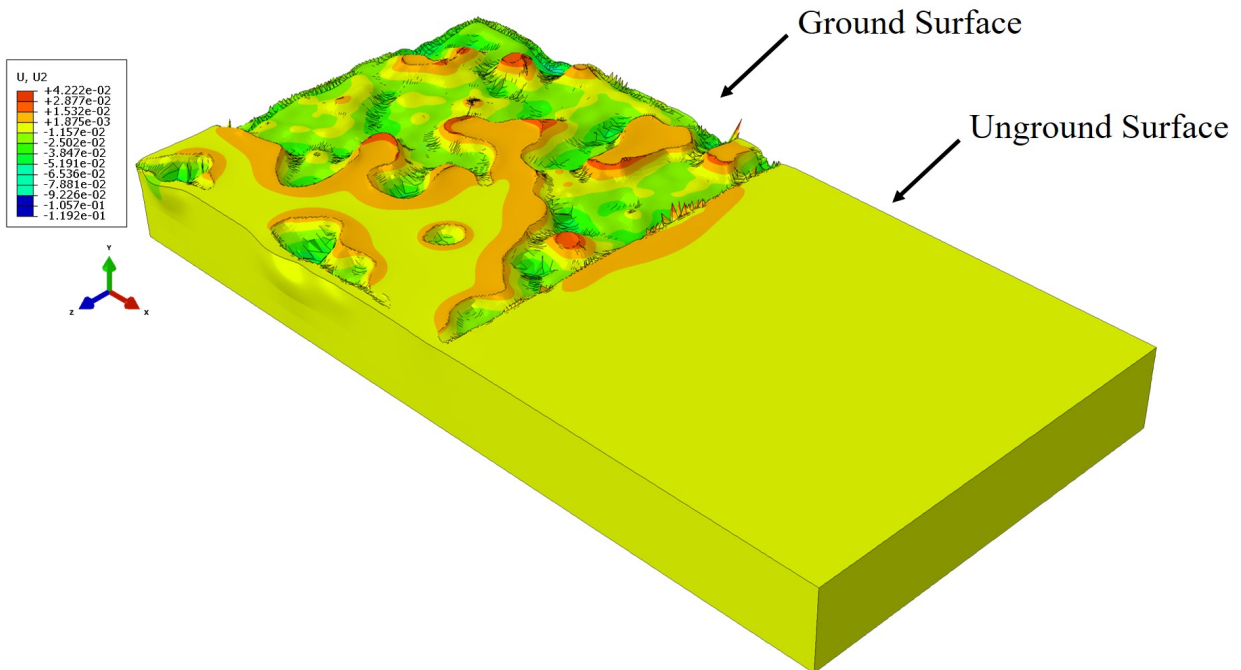


FIGURE 7.26: Displacement contour showing ground surface topography performed using the virtual wheel specimen

Fig. 7.27 shows an exemplary 2D cross sectional profile of the ground workpiece. It can be observed during material removal that multiple groove and pile-up regions are produced. Similar to analysis of the results of single grit simulations, from the virtual wheel material removal simulations the process forces, pile-up ratio and specific energy can be calculated. However, in this thesis, a quantitative analysis of the results is not performed as there were some technical difficulties encountered while performing the simulations. While converting the 3D .stl surface to a FEM mesh, some important geometrical features present in the .stl geometry are permanently lost. As a result, a simplified geometry of a virtual grinding wheel surface is only obtained. This problem needs to be addressed by finding out an appropriate method to better capture complicated tool geometries into a FEM mesh. Also, while performing the material removal simulation, there is high element distortion that occurs due to premature failure of FE mesh elements. Some alternate discretizational approaches are required to be applied to solve this specific problem. Considering the above points, a validation of the virtual wheel material removal simulations with experiments could not be established. The present version of the model is developed to qualitatively display an FEM based approach of up-scaling from a grit-workpiece model to a wheel-workpiece model. Further developments to this model can help to better understand complicated material removal mechanisms that occur in grinding. The model can also help isolate optimized process parameters by reducing the effort of experimentation.

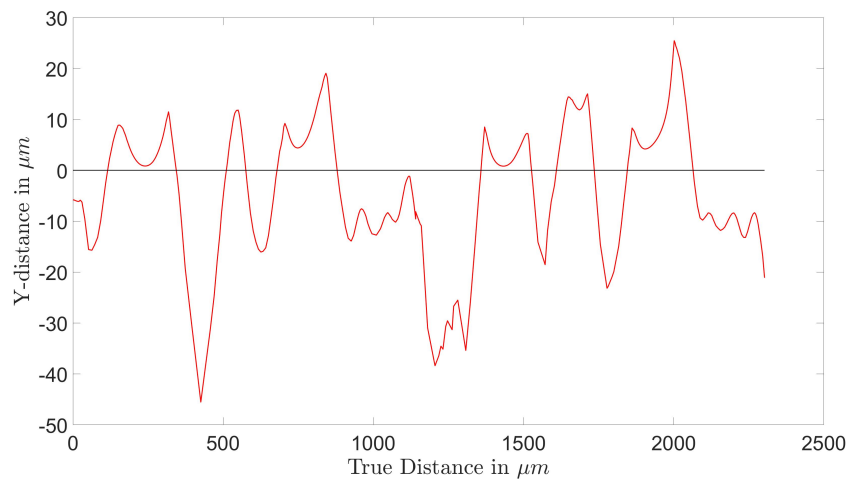


FIGURE 7.27: 2D cross sectional ground profile of the workpiece using the sample virtual wheel model

7.4.2 Simulation with complete grinding wheel

Under this section, the simulation framework of an up-cut surface grinding employing a flat grinding wheel surface is discussed. Figure 7.28 shows the grinding wheel and the workpiece. The grinding wheel is modeled as a rigid body and the workpiece as a deformable body.

Fig.7.28 shows the simulation setup of a grinding process simulation. In this simulation, the grinding wheel does not consider a virtual topography of an actual grinding wheel and is modeled as a flat surface. In this method, the surface of the workpiece is moved in the opposite direction of the rotating grinding wheel at periodic intervals. This will significantly remove material from the

surface of the workpiece. Repeating this process by moving the workpiece at significant intervals and removing the unwanted part of the workpiece surface, a smooth surface is obtained.

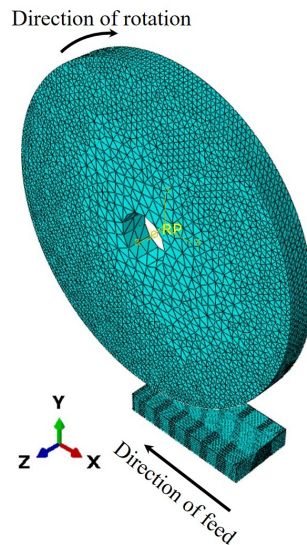


FIGURE 7.28: simulation setup of a grinding process simulation

Fig. 7.29 shows the distribution of displacement along the negative y -direction in μm . It can be observed that the ground surface shows some variations in the material removal, however the variation lies in minute scale of $0.1 \mu\text{m}$, thereby producing a flat ground workpiece. This simulation successfully produces grinding grooves, as it incorporates a round trajectory of a grinding process. However, in reality, the ground surface (grinding grooves) could have more intricate asperities due to variations in material removal mechanisms (rubbing-plowing-cutting). As this model does not consider the grinding wheel topography, some important effects of material removal in grinding are not successfully captured. If the previously developed virtual wheel model is integrated to this simulation, the simulation could more realistically describe material removal in grinding. This enables a lot of flexibility to continuously optimize and draw practical conclusions of the grinding process.

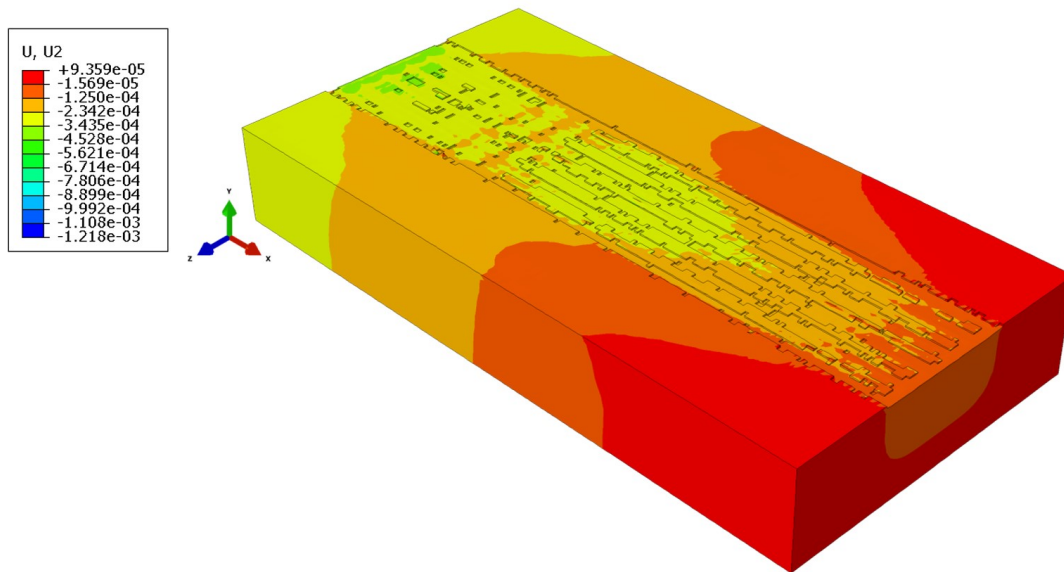


FIGURE 7.29: Distribution of displacement during the grinding process

7.5 Summary of wheel-workpiece approach simulations

In this chapter, simulations were developed considering the wheel-workpiece approach. To develop a realistic material removal simulation considering the interaction of a grinding wheel and workpiece, a realistic grinding wheel must be generated. A realistic virtual wheel model is generated based on a through-the-process approach. i.e., considering each manufacturing step during the production of a grinding wheel. The advantage of this approach over generating a virtual wheel topography from topographical scan would be the ability to generate realistic topographies of grinding wheel with different mesh sizes and thereby reducing experimental effort. The virtual wheel model is validated based on grinding wheel measurement performed at the laboratory. Finally, different output variables are analyzed, i.e., alternative static grain count and alternative protrusion height as a function of manufacturing and dressing parameters. Practical conclusions are also drawn based on the radar charts generated.

After the generation of the virtual wheel topography, it is integrated into the FEM material model. Thereby, the FEM model developed is based on the wheel-workpiece approach. In an initial simulation, a sample grinding wheel topography is used to simulate the material removal process. The model needs to be further developed and validated in the future. The current model provides a basic methodology to upscale an FEM simulation from grit-workpiece approach to wheel-workpiece approach

Finally, a simulation of an up-grinding process is developed. However, in this simulation, the actual topography of the grinding wheel is not considered. The grinding wheel is modeled as a flat surface. The results are presented in the form of stress and displacement contour plots. In the future, it is recommended that the actual grinding wheel topography is integrated to this simple grinding simulation model to better analyze the material removal process that occurs during grinding.

Chapter 8

Conclusions and suggestions for future work

8.1 Conclusions

As part of this study, material removal mechanisms have been investigated using single grit abrasive action on the workpiece. The fundamental mechanisms of rubbing, plowing, and cutting occur during single grit abrasive action. Of these three mechanisms, the cutting mechanism during chip formation by conventional cutting processes such as turning and milling are often simulated with FEM models in macro-scale. The grinding mechanism is different in comparison to the conventional cutting processes in terms of the number of cutting edges and cutting tool geometry. In grinding, numerous abrasive grits collectively perform material removal process at much smaller depth of cut in comparison to conventional cutting processes.

In this thesis, single grit removal mechanisms have been investigated both experimentally and numerically. Single grit and multiple grit experimental studies were performed by varying the shape of the cutting tool, depth of cut and linear cutting speed. The experimental results were assessed based on process forces and topographical characteristics. The experiments were analyzed based on five output variables namely pile-up ratio, chip removal strength, effective grit engaging radius, process forces and specific energy.

The pile-up ratio is a good indicator of the material removal mechanism that occurs during a single grit scratch process. A lower pile-up ratio is measured when the cutting mechanism is prominent. During the material removal process, as the grit cutting geometry continuously changes, it is difficult to separate the plowing mechanism and cutting mechanisms from each other. However, based on the topographical measurements it could be predicted when the plowing mechanism is more prominent than cutting mechanism or vice versa. For example, the cutting mechanism is prominent with increasing depth of cut. The shape of the abrasive grit also plays a substantial role to ascertain if the prominent mechanism is plowing or cutting. A sharper pyramidal grit gives a greater cutting action with increasing depth of cut in contrast to a flat conical grit. Rubbing action is the most difficult one to capture where only elastic deformation takes place without any material removal. On comparing the pile up ratio between the SST's and MPST's, it is observed that the pile-up ratio increases for MPST, showing that the plowing action is much more prominent while performing MPST.

The measurement of process forces is very important to analyze the single grit grinding process and in the calculation of the specific energy. With accurate force measurements, the force measured along the scratch can be correlated to the topographical measurements. For example,

it can be observed that with increasing process forces the groove area increases. In general, the process forces increase with the increase in the depth of cut and the MPST measures higher process forces in comparison to SST.

The specific energy is the amount of energy required to remove a unit volume of material. The lower the specific energy, the more effective is the material removal. Hence, specific energy is a key performance indicator of the grinding process. In general, it can be observed that specific energy reduces with increase in depth of cut, indicating prominent cutting mechanism. The shape of the grit has an important effect on the specific energy. Sharper pyramidal grits measure a lower specific energy, in comparison to conical grits. On comparing MPST and SST, specific energy measured for MPST is higher in comparison to SST, due to interaction of individual scratches.

The simulation model is developed under two approaches, grit-workpiece approach, and wheel-workpiece approach. In the context of development of the grit-workpiece approach, the aim was to develop a FEM model to capture the single grit grinding process and material removal process. A 2D orthogonal cutting model discussed in Section 6.4, is developed to simulate the cutting mechanism. A computationally less intensive model is employed to test various mesh discretizations and optimal element sizes. However, when the model is tested with high negative rake angles the process forces did not match with the SST experimental results performed at the laboratory. A 3D scratch model discussed in Section 6.5 is developed inheriting the tested optimized simulation parameters (mesh size, material and contact parameters) from the 2D orthogonal cutting model. The 3D model is initially tested with various mesh discretizations (LAG, ALE and SPH) and the calculated forces are bench-marked with process forces measured from experiments. It is observed that the ALE method predicts the forces in closest congruence with the experimental results. The ALE 3D scratch model is further tested by varying the tool geometry and depth of cut. The conical and pyramidal single scratch models were validated with the SST experiments. The calculated process forces and the scratch topographies were in good agreement with the experimental measurements.

After successfully validating the ALE 3D scratch model, it is extended to simulate a Multiple Pass Scratch Test (MPST). The results from the model were also validated with experimental measurements. The calculated process forces and the scratch topographies were in good agreement with the experimental measurements. Finally, the pile-up ratio and specific energy calculated from SST and MPST simulation models are presented. The models are tested to see if they are capable of building tendencies as observed from the single/multiple grit scratch experiments. It is observed that the simulation models successfully build these tendencies. As the grit-workpiece model is successfully validated with experimental measurements and can build the tendencies as observed in the experiments, it could be used to save enormous experimental effort and can be employed to continuously optimize grinding process parameters.

In the context of development of the wheel-workpiece approach, the aim was to develop an up-scale model from grit-workpiece interaction to wheel-workpiece interaction and thereby simulating an actual grinding process. As in a grinding process there is simultaneous interaction of multiple grits on the workpiece, an employment of realistic grinding wheel topography on simulating the material removal process in grinding will produce reliable results. A virtual grinding wheel topographical model is modeled using a through-the-process approach, following all manufacturing steps during the fabrication of a grinding wheel. Section 7.2 describes the simulation framework of developing a virtual grinding wheel topography. The grinding wheel

topographical model is evaluated based on static grain count and protrusion height. The topographical model is also validated by comparing static grain count and protrusion heights with measurements obtained from silicon carbide grinding wheels using optical microscopy. Based on various sensitivity studies performed, radar charts are created that help in choosing the right grinding wheel based on the application.

The virtual wheel model developed can be extracted as a .stl file to be further incorporated in the FEM material removal model. In Section 7.4.1, a material removal process is simulated with a sample grinding wheel topography. The process forces and ground surface topography are analyzed from the simulation results. Although the simulation is successful in upscaling the FEM simulation from grit-workpiece to wheel-workpiece approach, there are some drawbacks encountered with this model. These need to be addressed and validated with grinding experiments to make the quantitative results more reliable.

Finally, a simulation model is developed to simulate an up-cut surface grinding operation with a flat grinding wheel surface. The von-Mises stresses and displacements measured on the ground surface are presented. However, this simulation does not incorporate the grinding wheel topography due to technology constraints. This model also serves to provide a possible approach of scaling from grit-workpiece interaction to wheel-workpiece interaction. In future, it is recommended that the actual grinding wheel topography is integrated into the simple grinding simulation model to better analyze the material removal process that occurs during grinding.

8.2 Possible future work

There are a lot of possibilities at various crucial work points to improve on the experimentation and simulations.

Single grit experiments in future can be performed with a rotatory disk with a single grit affixed to its circumference [82]. This experimental methodology can better represent the grit trajectory that takes place during an up-grinding process. This can foster the ability to perform experiments at higher cutting speeds. However, it would be difficult to maintain a set depth of cut while performing experiments with a rotating wheel, unlike the currently used single axis linear scratch device. The experimentation could also be focused in employing various other complicated grit shapes such as diamonds, hexagons, or more complicated polygons at different orientations. The plowing effect, chip removal and process forces can be analyzed using different shaped grits. The bond fracture between grits increases wear in the grinding wheel and thereby increases the dressing frequency. This would increase manufacturing costs as well as production time. Hence, focused experiments to understand bond-grit kinematics and bond fracture from single grit tests can determine the bond strength of a grinding wheel. Also, extending the experiments to depths of cut of less than $10\mu\text{m}$ would provide information of the material removal mechanisms at sub-micrometer level. With respect to topographical measurements, surface roughness could be used as an important output variable to assess the grinding performance. Experiments also need to be performed with cooling fluids to understand the effect on temperature, process forces and ground topography. Generation of a large amount of experimental data provides scope to use the data to train recurrent neural networks to estimate dynamic evolution of grinding process variables such as wheel wear or specific grinding energy [57].

FEM simulations are widely used in conventional machining processes where the material removal occurs at a macro scale. However, single grit simulations were performed at depths of cut at micro-scale. The simulation can be extended to a depth of cut as little as $1\mu\text{m}$ or less. This would be highly difficult while using methods like LAG or ALE as this would cause high element deletion. This is because very small elements would be needed at the cutting area to simulate chip removal at sub-micron levels. Incorporating highly efficient and dynamic re-meshing techniques can help but this would drastically increase the computational effort. To reduce the drawback of mesh distortion, the focus for this application can be turned towards using meshless particle-based approaches like SPH and PFEM. Although, a lot of the particle based approaches are currently in development phase and require increased computational effort. Methods like an implicit SPH, implicit PFEM or implicit Element Free Galerkin (EFG) approach can solve the distortion problem that occurs at sub-micro level and at the same time reduce computational effort. The simulation needs to be extended incorporating the effect of the cooling fluid on the output process variables. The simulation would be complicated as fluid structure interaction problem is to be solved.

With respect to the wheel-workpiece simulations, certain improvements can be suggested. In the virtual grinding wheel simulation, a digital twin of grinding wheel is generated using a through-the-process approach. However, the simulation has certain limitations that can be improved in future. The DEM simulation in this study does not separate particles into bond material and abrasive grits. Due to this simplification, some of the compression results might be affected. By using a different DEM software for the simulation of particle mixing and compression stages, this potential source of errors could be avoided. Also, DEM simulation assumes that the particle along with the bond layer are perfect spheres, which is not the case. One approach of modeling particles as clumped multi-spheres [30] is using Monte Carlo method to generate granular particle geometries. Alternatively, modelling of particles as fractal geometries [78] can be employed to obtain granular particle shapes. It is also observed that the simulation is not feasible to obtain realistic grinding wheel topographies of particle sizes smaller than grit 80, requiring further development towards this direction. It is to be also noted that the overlap ratio = 1, is considered in the simulations performed. This is initially considered to reduce the computational intensity of the simulations. However, in reality the overlap ratio is chosen between 2-6 [55], this need to be adjusted in future simulations studies.

Finally, the up-scaled grinding simulation considers a small section of grinding wheel to simulate material removal process. There are some limitations with this simulation. There are some simplifications done on the grinding wheel topographical geometry to successfully apply a FE mesh. This could lead to the loss of some of the crucial information related to the complex wheel topography. Also, to efficiently capture intricate grinding wheel topography, a FE mesh with very small elements needs to be applied. This would drastically increase the computational effort. Employing a very fine FE mesh also leads to uncontrollable distortion problems which are quite complicated to solve. Use of the above-mentioned particle-based approaches can help alleviate this problem. In the case of complete grinding wheel simulation, a flat rotating wheel is used which does not consider the actual grinding wheel topography. In future, a rotational grinding wheel incorporating the actual wheel topography can better represent the material removal process that occurs during grinding.

Bibliography

- [1] Pedro J Arrazola et al. “Investigations on the effects of friction modeling in finite element simulation of machining”. In: *International journal of mechanical sciences* 52.1 (2010), pp. 31–42.
- [2] P.J. Arrazola. “Modelisation numerique de la coupe: etude de sensibilite des parametres d’entree et identification du frottement entre outil-copeau”. PhD thesis. L’École Centrale de Nantes, 2003.
- [3] N Arunachalam, L Vijayaraghavan, et al. “Evaluation of grinding strategy for bioceramic material through a single grit scratch test using force and acoustic emission signals”. In: *Journal of Manufacturing Processes* 37 (2019), pp. 457–469.
- [4] JC Aurich and H Bil. “3D finite element modelling of segmented chip formation”. In: *CIRP annals* 55.1 (2006), pp. 47–50.
- [5] WR Backer. “Marshall., ER, Shaw, MC”. In: *The size effect in metal cutting* (1952), pp. 61–72.
- [6] Author Jeffrey A. Badger and Jeffrey A. Badger. *Up vs. down grinding*. URL: <https://www.ctemag.com/news/articles/vs-down-grinding>.
- [7] AK Baldoukas, FA Soukatzidis, GA Demosthenous, and AE Lontos. “Experimental investigation of the effect of cutting depth, tool rake angle and workpiece material type on the main cutting force during a turning process”. In: *Proceedings of the 3rd International Conference on Manufacturing Engineering (ICMEN)*. Vol. 1. 3. 2008.
- [8] Thomas Bergs, M Ohlert, S Prinz, and S Barth. “Modeling of the Fracture Behavior of CBN Grains during Single Grain Dressing using FEM”. In: *Procedia CIRP* 93 (2020), pp. 1514–1519.
- [9] CP Bhateja and RP Lindsay. “The importance of abrasive grinding wheel hardness control for the productivity of production grinding operations”. In: *CIRP Annals* 30.1 (1981), pp. 247–249.
- [10] Halil Bil, S Engin Kılıç, and A Erman Tekkaya. “A comparison of orthogonal cutting data from experiments with three different finite element models”. In: *International Journal of Machine Tools and Manufacture* 44.9 (2004), pp. 933–944.
- [11] L Blunt and S Ebdon. “The application of three-dimensional surface measurement techniques to characterizing grinding wheel topography”. In: *International Journal of Machine Tools and Manufacture* 36.11 (1996), pp. 1207–1226.

- [12] Józef A Borkowski and Andrzej M Szymanski. “Uses of abrasives and abrasive tools”. In: (1991).
- [13] Benjámín Borsos, András Csörgő, Anna Hidas, Bálint Kotnyek, Antal Szabó, Attila Kossa, and Gábor Stépán. “Two-dimensional finite element analysis of turning processes”. In: *Periodica Polytechnica Mechanical Engineering* 61.1 (2017), pp. 44–54.
- [14] D Bouvard and RM McMeeking. “Deformation of interparticle necks by diffusion-controlled creep”. In: *Journal of the American Ceramic Society* 79.3 (1996), pp. 666–672.
- [15] E Brinksmeier, JC Aurich, Edvard Govekar, C Heinzl, H-W Hoffmeister, F Klocke, J Peters, R Rentsch, DJ Stephenson, E Uhlmann, et al. “Advances in modeling and simulation of grinding processes”. In: *CIRP annals* 55.2 (2006), pp. 667–696.
- [16] A Brosse, P Naisson, H Hamdi, and JM Bergheau. “Temperature measurement and heat flux characterization in grinding using thermography”. In: *Journal of materials processing technology* 201.1-3 (2008), pp. 590–595.
- [17] Huang-Cheng Chang and J-J Junz Wang. “A stochastic grinding force model considering random grit distribution”. In: *International Journal of Machine Tools and Manufacture* 48.12-13 (2008), pp. 1335–1344.
- [18] Sami Chatti, Luc Laperrière, Gunther Reinhart, Tullio Tolio, et al. *CIRP encyclopedia of production engineering*. Springer, 2019.
- [19] X. Chen and W.B. Rowe. “Analysis and simulation of the grinding process. Part I: generation of the grinding wheel surface”. In: *International Journal of Machine Tools and Manufacture* 36.8 (1996), pp. 871–882.
- [20] Xun Chen and Tahsin Tecelli Öpöz. “Comparison of material removal characteristics in single and multiple cutting edge scratches”. In: *Advanced Materials Research*. Vol. 797. Trans Tech Publ. 2013, pp. 189–195.
- [21] Thomas HC Childs, Katsuhiro Maekawa, Toshiyuki Obikawa, and Yasuo Yamane. *Metal machining: theory and applications*. Butterworth-Heinemann, 2000.
- [22] Francisco Chinesta, Philippe Lorong, D Ryckelink, G Coffignal, M Tourantier, MA Martinez, Elías Cueto, and M Doblaré. “Thermomechanical cutting model discretisation: eulerian or lagrangian, mesh or meshless?” In: *Esaform Conference proceedings*. 2002.
- [23] Timothy D Davis, Julia DiCorleto, David Sheldon, Jodi Vecchiarelli, and Can Erkey. “A route to highly porous grinding wheels by selective extraction of pore inducers with dense carbon dioxide”. In: *The Journal of supercritical fluids* 30.3 (2004), pp. 349–358.
- [24] Wenfeng Ding, Barbara Linke, Yejun Zhu, Zheng Li, Yucan Fu, Honghua Su, and Jiuhua Xu. “Review on monolayer CBN superabrasive wheels for grinding metallic materials”. In: *Chinese Journal of Aeronautics* 30.1 (2017), pp. 109–134.

- [25] M Djemana and M Hrairi. “Modelling and simulation of impedance-based damage monitoring of structures”. In: *Int. J. Simul. Model* 15.3 (2016), pp. 395–408.
- [26] D.A. Doman, R. Bauer, and A. Warkentin. “Experimentally validated finite element model of the rubbing and ploughing phases in scratch tests”. In: *Proceedings of the Institution of Mechanical Engineers, Part B: Journal of Engineering Manufacture* 223.12 (2009), pp. 1519–1527.
- [27] DA Doman, A Warkentin, and R Bauer. “A survey of recent grinding wheel topography models”. In: *International Journal of Machine Tools and Manufacture* 46.3-4 (2006), pp. 343–352.
- [28] Nian Duan, Yiqing Yu, Wenshan Wang, and Xipeng Xu. “SPH and FE coupled 3D simulation of monocrystal SiC scratching by single diamond grit”. In: *International Journal of Refractory Metals and Hard Materials* 64 (2017), pp. 279–293.
- [29] Kamal Dwivedi. *Grinding wheel:material,Bond,grain size,grade,specification,types*. 2022. URL: <https://www.mechical.com/2020/11/grinding-wheel-definition-material-bond.html>.
- [30] J Eberhardsteiner et al. *Approximation of Objects by Spheres for Multisphere Simulations in DEM*.
- [31] Cui Fang, Congbin Yang, Ligang Cai, Yongsheng Zhao, and Zhifeng Liu. “Predictive modeling of grinding force in the inner thread grinding considering the effect of grains overlapping”. In: *The International Journal of Advanced Manufacturing Technology* 104.1 (2019), pp. 943–956.
- [32] BF Feng and Guang Qi Cai. “Experimental study on the single-grit grinding titanium alloy TC4 and superalloy GH4169”. In: *Key engineering materials*. Vol. 202. Trans Tech Publ. 2001, pp. 115–120.
- [33] S Ghosh, AB Chattopadhyay, and S Paul. “Study of grinding mechanics by single grit grinding test”. In: *International Journal of Precision Technology* 1.3-4 (2010), pp. 356–367.
- [34] *Grinding wheels*. 2022. URL: <https://grindaix.de/en/magazine/grinding-wheels/>.
- [35] Mustafa Günay, Ihsan Korkut, Ersan Aslan, and Ulvi Şeker. “Experimental investigation of the effect of cutting tool rake angle on main cutting force”. In: *Journal of materials processing technology* 166.1 (2005), pp. 44–49.
- [36] Mohammadjafar Hadad. “An experimental investigation of the effects of machining parameters on environmentally friendly grinding process”. In: *Journal of Cleaner Production* 108 (2015), pp. 217–231.
- [37] RS Hahn. “Discussion:“On Determining the Hardness of Grinding Wheels—F”(Colwell, LV, Lane, RO, and Soderlund, KN, 1962, ASME J. Eng. Ind., 84, pp. 113–126)”. In: (1962).
- [38] Saleem Hashmi. *Comprehensive materials processing*. Newnes, 2014.

- [39] Amauri Hassui, Anselmo Eduardo Diniz, João Fernando Gomes de Oliveira, J Felipe, and João Jorge de Faria Gomes. “Experimental evaluation on grinding wheel wear through vibration and acoustic emission”. In: *Wear* 217.1 (1998), pp. 7–14.
- [40] Arne Hillerborg, Mats Modéer, and P-E Petersson. “Analysis of crack formation and crack growth in concrete by means of fracture mechanics and finite elements”. In: *Cement and concrete research* 6.6 (1976), pp. 773–781.
- [41] Z.B. Hou and R. Komanduri. “On the mechanics of the grinding process—Part I. Stochastic nature of the grinding process”. In: *International journal of machine tools and manufacture* 43.15 (2003), pp. 1579–1593.
- [42] Syed Amir Iqbal, PT Mativenga, and Mohammad A Sheikh. “Contact length prediction: mathematical models and effect of friction schemes on FEM simulation for conventional to HSM of AISI 1045 steel”. In: *International journal of machining and machinability of materials* 3.1-2 (2008), pp. 18–33.
- [43] MJ Jackson. “A review of the design of grinding wheels operating at excessive speeds”. In: *The International Journal of Advanced Manufacturing Technology* 94 (2018), pp. 3979–4010.
- [44] Chuan-Zhi Jing, Ji-Lai Wang, Xue Li, Yi-Fei Li, and Lu Han. “Influence of Material Microstructure on Machining Characteristics of OFHC Copper C102 in Orthogonal Micro-Turning”. In: *Processes* 10.4 (2022), p. 741.
- [45] Gordon R Johnson and William H Cook. “Fracture characteristics of three metals subjected to various strains, strain rates, temperatures and pressures”. In: *Engineering fracture mechanics* 21.1 (1985), pp. 31–48.
- [46] G.R. Johnson and W.H. Cook. “A constitutive model and data for metals subjected to large strains, high strain rates and high temperatures”. In: *Proceedings of the 7th International Symposium on Ballistics*. 1983, pp. 541–547.
- [47] GR Johnson and TJ Holmquist. “Test data and computational strength and fracture model constants for 23 materials subjected to large strains, high strain rates, and high temperatures”. In: *Los Alamos National Laboratory, LA-11463-MS* 198 (1989).
- [48] Bernhard Karpuschewski, Tjark Lierse, Timo Rouven Kaul, Steffen Schulze, and Dominik Mueller-Cramm. “Kinematic process model and investigation of grain breakout for conditioning with CVD diamond dressing disks”. In: *CIRP Journal of Manufacturing Science and Technology* 22 (2018), pp. 21–29.
- [49] Gregory Kay. *Failure modeling of titanium 6Al-4V and aluminum 2024-T3 with the Johnson-Cook material model*. Office of Aviation Research, Federal Aviation Administration, 2003.
- [50] Mohammad Khoran, Bahman Azarhoushang, and Amir Daneshi. “Experimental study of single grit scratch test on carbon fiber-reinforced polyether ether ketone”. In: *Production Engineering* 15.5 (2021), pp. 751–759.

- [51] Robert I King and Robert S Hahn. *Handbook of modern grinding technology*. Springer Science & Business Media, 2012.
- [52] B. Kirsch, C. Effgen, M. Büchel, and J.C. Aurich. “Comparison of the embodied energy of a grinding wheel and an end mill”. In: *Procedia CIRP* 15 (2014), pp. 74–79.
- [53] Fritz Klocke, Thorsten Beck, Stefan Hoppe, Tilo Krieg, Norbert Müller, Tobias Nöthe, Hans-Willi Raedt, and Kevin Sweeney. “Examples of FEM application in manufacturing technology”. In: *Journal of Materials Processing Technology* 120.1-3 (2002), pp. 450–457.
- [54] Fritz Klocke, Ekkard Brinksmeier, and K Weinert. “Capability profile of hard cutting and grinding processes”. In: *CIRP annals* 54.2 (2005), pp. 22–45.
- [55] Fritz Klocke, Janis Thiermann, and Patrick Mattfeld. “Influence of the dressing process on grinding wheel wear”. In: *Production Engineering* 9 (2015), pp. 563–568.
- [56] Philip Koshy, VK Jain, and GK Lal. “Stochastic simulation approach to modelling diamond wheel topography”. In: *International Journal of Machine Tools and Manufacture* 37.6 (1997), pp. 751–761.
- [57] Ander Arriandiaga Laresgoiti. “Recurrent neural network based approach for estimating the dynamic evolution of grinding process variables”. PhD thesis. Universidad del País Vasco-Euskal Herriko Unibertsitatea, 2016.
- [58] M. Li, W. Ding, B. Li, and J. Xu. “Morphological evolution and grinding performance of vitrified bonded microcrystal alumina abrasive wheel dressed with a single-grit diamond”. In: *Ceramics International* 45.16 (2019), pp. 19669–19678.
- [59] X. Li and Y. Rong. “Framework of grinding process modeling and simulation based on microscopic interaction analysis”. In: *Robotics and Computer-Integrated Manufacturing* 27.2 (2011), pp. 471–478.
- [60] Xuekun Li. “Modeling and simulation of grinding processes based on a virtual wheel model and microscopic interaction analysis”. In: *Worcester Polytech Inst* 4 (2010), pp. 38–78.
- [61] Xuekun Li and Yiming Kevin Rong. “Kinematics Simulation of Grinding Process Based on Virtual Wheel Model and Micro-Cutting Analysis”. In: *International Manufacturing Science and Engineering Conference*. Vol. 43611. 2009, pp. 341–346.
- [62] Xuekun Li, Sebastian Wolf, Geng Zhi, and Yiming Kevin Rong. “The modelling and experimental verification of the grinding wheel topographical properties based on the ‘through-the-process’ method”. In: *The International Journal of Advanced Manufacturing Technology* 70.1-4 (2014), pp. 649–659.
- [63] Jérôme Limido, Christine Espinosa, Michel Salaün, and Jean-Luc Lacomme. “SPH method applied to high speed cutting modelling”. In: *International journal of mechanical sciences* 49.7 (2007), pp. 898–908.

- [64] Barbara Linke and Fritz Klocke. “Temperatures and wear mechanisms in dressing of vitrified bonded grinding wheels”. In: *International journal of machine tools and manufacture* 50.6 (2010), pp. 552–558.
- [65] Gui-Rong Liu and Moubin B Liu. *Smoothed particle hydrodynamics: a meshfree particle method*. World scientific, 2003.
- [66] Qiang Liu, Xun Chen, Yan Wang, and Nabil Gindy. “Empirical modelling of grinding force based on multivariate analysis”. In: *Journal of Materials Processing Technology* 203.1-3 (2008), pp. 420–430.
- [67] Tarek Mabrouki, François Girardin, Muhammad Asad, and Jean-François Rigal. “Numerical and experimental study of dry cutting for an aeronautic aluminium alloy (A2024-T351)”. In: *International Journal of Machine Tools and Manufacture* 48.11 (2008), pp. 1187–1197.
- [68] Martin Madaaj and Miroslav Píška. “On the SPH orthogonal cutting simulation of A2024-T351 alloy”. In: *Procedia Cirp* 8 (2013), pp. 152–157.
- [69] Stephen Malkin and Changsheng Guo. “Thermal analysis of grinding”. In: *CIRP annals* 56.2 (2007), pp. 760–782.
- [70] Athanasios G Mamalis, Dimitrios E Manolakos, A Markopoulos, J Kunádrk, and Károly Gyáni. “Thermal modelling of surface grinding using implicit finite element techniques”. In: *The International Journal of Advanced Manufacturing Technology* 21.12 (2003), pp. 929–934.
- [71] Abaqus User Manual. “Abaqus user manual”. In: *Abacus* (2020).
- [72] I.D. Marinescu, W.B. Rowe, B. Dimitrov, and H. Ohmori. *Tribology of abrasive machining processes*. William Andrew, 2012.
- [73] TD Marusich and Modeling Ortiz. “Modelling and simulation of high-speed machining”. In: *International Journal for numerical methods in engineering* 38.21 (1995), pp. 3675–3694.
- [74] T Matsuo, S Toyoura, E Oshima, and Y Ohbuchi. “Effect of grain shape on cutting force in superabrasive single-grit tests”. In: *CIRP Annals* 38.1 (1989), pp. 323–326.
- [75] H Miguélez, R Zaera, Alexis Rusinek, A Moufki, and A Molinari. “Numerical modelling of orthogonal cutting: Influence of cutting conditions and separation criterion”. In: *Journal de Physique IV (Proceedings)*. Vol. 134. EDP sciences. 2006, pp. 417–422.
- [76] Amir Mir, Xichun Luo, Kai Cheng, and Andrew Cox. “Investigation of influence of tool rake angle in single point diamond turning of silicon”. In: *The International Journal of Advanced Manufacturing Technology* 94.5 (2018), pp. 2343–2355.

- [77] Vijay Kumar Mishra and Konstantinos Salonitis. “Empirical estimation of grinding specific forces and energy based on a modified Werner grinding model”. In: *Procedia Cirp* 8 (2013), pp. 287–292.
- [78] Guilhem Mollon and Jidong Zhao. “3D generation of realistic granular samples based on random fields theory and Fourier shape descriptors”. In: *Computer Methods in Applied Mechanics and Engineering* 279 (2014), pp. 46–65.
- [79] Jiwoo Nam, Taesung Kim, and Seong Wook Cho. “A numerical cutting model for brittle materials using smooth particle hydrodynamics”. In: *The International Journal of Advanced Manufacturing Technology* 82.1-4 (2016), pp. 133–141.
- [80] Yoshifumi Ohbuchi and Toshiyuki Obikawa. “Finite element modeling of chip formation in the domain of negative rake angle cutting”. In: *J. Eng. Mater. Technol.* 125.3 (2003), pp. 324–332.
- [81] Lars Olovsson, Larsgunnar Nilsson, and Kjell Simonsson. “An ALE formulation for the solution of two-dimensional metal cutting problems”. In: *Computers & structures* 72.4-5 (1999), pp. 497–507.
- [82] T. Opoz. *Investigation of Material Removal Mechanism in Grinding: A Single Grit Approach*. Doctoral thesis, University of Huddersfield. 2012. ISBN: 1855213656.
- [83] Tahsin T Öpöz and Xun Chen. “Experimental study on single grit grinding of Inconel 718”. In: *Proceedings of the Institution of Mechanical Engineers, Part B: Journal of Engineering Manufacture* 229.5 (2015), pp. 713–726.
- [84] Tahsin Tecelli Opoz. “Investigation of material removal mechanism in grinding: a single grit approach”. PhD thesis. University of Huddersfield, 2012.
- [85] Tugrul Özel. “The influence of friction models on finite element simulations of machining”. In: *International journal of machine tools and manufacture* 46.5 (2006), pp. 518–530.
- [86] Olivier Pantalé, Roger Rakotomalala, and Maurice Touratier. “An ALE three-dimensional model of orthogonal and oblique metal cutting processes”. In: *International Journal of Forming Processes* 1 (1998), pp. 371–389.
- [87] Hyung Wook Park and Steven Y Liang. “Force modeling of microscale grinding process incorporating thermal effects”. In: *The International Journal of Advanced Manufacturing Technology* 44.5 (2009), pp. 476–486.
- [88] M. Prasad, M. Kopycinska, U. Rabe, and W. Arnold. “Measurement of Young’s modulus of clay minerals using atomic force acoustic microscopy: Geophysical Research Letter, 29”. In: (2002).
- [89] JM Rodriguez Prieto, Josep Maria Carbonell, JC Cante, Javier Oliver, and Par Jonsen. “Generation of segmental chips in metal cutting modeled with the PFEM”. In: *Computational mechanics* 61.6 (2018), pp. 639–655.

- [90] *Products*. URL: <https://www.kistler.com/en/product/type-9119aa1/>.
- [91] Arsalan Qasim, Salman Nisar, Aqueel Shah, Muhammad Saeed Khalid, and Mohammed A Sheikh. "Optimization of process parameters for machining of AISI-1045 steel using Taguchi design and ANOVA". In: *Simulation Modelling Practice and Theory* 59 (2015), pp. 36–51.
- [92] Maziar Ramezani and Zaidi Mohd Ripin. "Combined experimental and numerical analysis of bulge test at high strain rates using split Hopkinson pressure bar apparatus". In: *Journal of Materials Processing Technology* 210.8 (2010), pp. 1061–1069.
- [93] Matthias Rasim, Patrick Mattfeld, and Fritz Klocke. "Analysis of the grain shape influence on the chip formation in grinding". In: *Journal of Materials Processing Technology* 226 (2015), pp. 60–68.
- [94] J Rodríguez, Pedro Arrazola, J Cante, Arratibel Kortabarria, and J Oliver. "A sensibility analysis to geometric and cutting conditions using the particle finite element method (PFEM)". In: *Procedia CIRP* 8 (2013), pp. 105–110.
- [95] Kipkurui Ronoh, Fredrick Mwema, Sameh Dabees, and Dinara Sobola. "Advances in sustainable grinding of different types of the titanium biomaterials for medical applications: A review". In: *Biomedical Engineering Advances* (2022), p. 100047.
- [96] W Brian Rowe. *Principles of modern grinding technology*. William Andrew, 2013.
- [97] Niklaus Ruttimann, Sebastian Buhl, and Konrad Wegener. "Simulation of single grain cutting using SPH method". In: *Journal of Machine Engineering* 10 (2010).
- [98] M San-Juan, Ó Martín, M del P de Tiedra, FJ Santos, R López, and JA Cebrián. "Study of cutting forces and temperatures in milling of AISI 316L". In: *Procedia Engineering* 132 (2015), pp. 500–506.
- [99] Kosaraju Satyanarayana, A Venugopal, and G VenkateswaraRao. "Effect of rake angle and feed rate on cutting forces in an orthogonal turning process". In: *Trends in Mechanical and Industrial Engineering (ICTMIE'2011)* (2011).
- [100] Dinesh Setti, Benjamin Kirsch, and Jan C Aurich. "Experimental investigations and kinematic simulation of single grit scratched surfaces considering pile-up behaviour: grinding perspective". In: *The International Journal of Advanced Manufacturing Technology* 103.1 (2019), pp. 471–485.
- [101] Vijayender Singh, US Patnaik Durgumahanti, P Venkateswara Rao, and S Ghosh. "Specific ploughing energy model using single grit scratch test". In: *International Journal of Abrasive Technology* 4.2 (2011), pp. 156–173.
- [102] Vijayender Singh, P Venkateswara Rao, and S Ghosh. "Development of specific grinding energy model". In: *International Journal of Machine Tools and Manufacture* 60 (2012), pp. 1–13.

- [103] SL Soo, DK Aspinwall, and RC Dewes. “3D FE modelling of the cutting of Inconel 718”. In: *Journal of Materials Processing Technology* 150.1-2 (2004), pp. 116–123.
- [104] Mohamed Souli, A Ouahsine, and L Lewin. “ALE formulation for fluid–structure interaction problems”. In: *Computer methods in applied mechanics and engineering* 190.5-7 (2000), pp. 659–675.
- [105] P Sridhar, D Mannherz, and KM de Payrebrune. “Modelling and Analysis of Topographic Surface Properties of Grinding Wheels”. In: *J. Manuf. Mater. Process* 5 (2021), p. 121.
- [106] Praveen Sridhar, Juan Manuel Rodríguez Prieto, and Kristin M de Payrebrune. “Discretization Approaches to Model Orthogonal Cutting with Lagrangian, Arbitrary Lagrangian Eulerian, Particle Finite Element Method and Smooth Particle Hydrodynamics Formulations”. In: *Procedia CIRP* 93 (2020), pp. 1496–1501.
- [107] Praveen Sridhar, Juan Manuel Rodríguez Prieto, and Kristin M de Payrebrune. “Modeling Grinding Processes—Mesh or Mesh-Free Methods, 2D or 3D Approach?” In: *Journal of Manufacturing and Materials Processing* 6.5 (2022), p. 120.
- [108] Piotr Stepień. “Grinding forces in regular surface texture generation”. In: *International Journal of Machine Tools and Manufacture* 47.14 (2007), pp. 2098–2110.
- [109] Yunhua Su, Bin Lin, and Zhongchen Cao. “Prediction and verification analysis of grinding force in the single grain grinding process of fused silica glass”. In: *The International Journal of Advanced Manufacturing Technology* 96.1 (2018), pp. 597–606.
- [110] S. Subbiah. “Some investigations of scaling effects in micro-cutting”. PhD thesis. Georgia Institute of Technology, 2006.
- [111] Taghi Tawakoli and Abdolreza Rasifard. “Dressing of grinding wheels”. In: *Machining with Abrasives*. Springer, 2011, pp. 181–244.
- [112] HK Tönshoff, J Peters, I Inasaki, and T Paul. “Modelling and simulation of grinding processes”. In: *CIRP annals* 41.2 (1992), pp. 677–688.
- [113] Morten F Villumsen and Torben G Fauerholdt. “Simulation of metal cutting using smooth particle hydrodynamics”. In: *LS-DYNA Anwenderforum, C-III* 17 (2008).
- [114] T Volz, R Schwaiger, J Wang, and SM Weygand. “Comparison of three approaches to determine the projected area in contact from finite element Berkovich nanoindentation simulations in tungsten”. In: *IOP Conference Series: Materials Science and Engineering*. Vol. 257. 1. IOP Publishing, 2017, p. 012013.
- [115] Konrad Wegener, H-W Hoffmeister, B Karpuschewski, F Kuster, W-C Hahmann, and M Rabiey. “Conditioning and monitoring of grinding wheels”. In: *CIRP annals* 60.2 (2011), pp. 757–777.

- [116] M. Weiß, F. Klocke, S. Barth, M. Rasim, and P. Mattfeld. “Detailed analysis and description of grinding wheel topographies”. In: *Journal of Manufacturing Science and Engineering* 139.5 (2017).
- [117] *Welcome to Micro Star Technologies*. 2022. URL: <https://microstartech.com/>.
- [118] *What is the grinding process and grinding wheel?* URL: <https://www.market-prospects.com/articles/what-is-the-grinding-process-and-grinding-wheel>.
- [119] *What Metals Work Best for Plating onto Ceramics*. <https://www.sharrettsplating.com/blog/metals-work-best-plating-ceramics/>. (Accessed on 11/30/2022).
- [120] Tomasz Wierzbicki, Yingbin Bao, Young-Woong Lee, and Yuanli Bai. “Calibration and evaluation of seven fracture models”. In: *International Journal of Mechanical Sciences* 47.4-5 (2005), pp. 719–743.
- [121] Martijn Woldman, Emile Van Der Heide, Tiedo Tinga, and Marc A Masen. “A finite element approach to modeling abrasive wear modes”. In: *Tribology transactions* 60.4 (2017), pp. 711–718.
- [122] Chongjun Wu, Weicheng Guo, Zhouping Wu, Qingxia Wang, and Beizhi Li. “Ductility-oriented high-speed grinding of silicon carbide and process design for quality and damage control with higher efficiency”. In: *The International Journal of Advanced Manufacturing Technology* 105.7 (2019), pp. 2771–2784.
- [123] HY Wu, Wing Bun Lee, Chi Fai Cheung, Suet To, and YP Chen. “Computer simulation of single-point diamond turning using finite element method”. In: *Journal of Materials Processing Technology* 167.2-3 (2005), pp. 549–554.
- [124] Hendri Yanda, Jaharah A Ghani, and Che Hassan Che Haron. “Effect of rake angle on stress, strain and temperature on the edge of carbide cutting tool in orthogonal cutting using FEM simulation”. In: *Journal of Engineering and Technological Sciences* 42.2 (2010), pp. 179–194.
- [125] Ali Zahedi and Bahman Azarhoushang. “FEM based modeling of cylindrical grinding process incorporating wheel topography measurement”. In: *Procedia Cirp* 46 (2016), pp. 201–204.
- [126] Feihu Zhang, Chen Li, Hang Zhao, Bing Leng, and Lele Ren. “Simulation and experiment of double grits interacting scratch for optical glass BK7”. In: *Journal of Wuhan University of Technology-Mater. Sci. Ed.* 33.1 (2018), pp. 15–22.
- [127] Man Zhao, Xia Ji, Beizhi Li, and Steven Y Liang. “Investigation on the influence of material crystallographic orientation on grinding force in the micro-grinding of single-crystal copper with single grit”. In: *The International Journal of Advanced Manufacturing Technology* 90.9 (2017), pp. 3347–3355.

- [128] Y.Y. Zhu, S.H. Liang, Z.J. Zhan, P. Xiao, and Z.K. Fan. “Simulation of the change of sintering neck between two grains in two dimensions”. In: *Acta Metallurgica Sinica (English Letters)* 19.6 (2006), pp. 397–404.

Lebenslauf

Berlin, 22 Februar 2024

Praveen Sridhar

Akademische Ausbildung

2018- 2022 Promotion in Maschinenbau und Verfahrenstechnik an der RPTU, Kasierslautern

2014-2018 Masterstudium in Computational Mechanics an der Universität Duisburg Essen, Essen

2009-2013 Bachelor-Abschluss in Maschinenbau an der Visvesvaraya Technological University, Karnataka, Indien

Berufserfahrung

seit 2022 Deloitte Consulting Solutions GmbH:
Senior Solutions Ingenieur in Smart Manufacturing.

2016-2017 MBtech Group GmbH:
Masterarbeit mit dem Thema „Prozessautomatisierung eines Finite-Elemente-basierten Pre-Processing-Tools zur Erzeugung von Fe-Modellen für die statische und akustische Analyse von Komponenten in einem Verbrennungsmotor.“

2012-2013 Indian Institute of Science:
Bachelorarbeit mit dem Thema „Simulation des Energieabsorptionsvermögens von Polyurethan-Schäumen.“

Computational Physics in Engineering - Berichte CPE

bereits veröffentlicht wurden

- 01/23 Lamping, F.: Vorteile durch die Berücksichtigung der Wechselwirkung von Modellierung und Design bei mehrkammerigen pneumatischen Soft Robots.
2023, ISBN 978-3-95974-204-7
- 02/23 Sridhar, P.: Physical Modeling of Material Removal in Grinding: Grit-Workpiece Approach and Wheel-Workpiece Approach.
2024, ISBN 978-3-95974-213-9

ISSN 2941-7066
ISBN 978-3-95974-213-9